# Fuel Cell Diagnostics using Electrochemical Impedance Spectroscopy

**by**

**Ghassan Mousa**

M.Eng., University of British Columbia, 2008
B.Sc., King Abdulaziz University, 2000

Thesis Submitted in Partial Fulfillment of the
Requirements for the Degree of
Doctor of Philosophy

in the
School of Mechatronic Systems Engineering
Faculty of Applied Sciences

**© Ghassan Mousa 2014**

**SIMON FRASER UNIVERSITY**

**Fall 2014**

All rights reserved.
However, in accordance with the *Copyright Act of Canada*, this work may be reproduced, without authorization, under the conditions for "Fair Dealing." Therefore, limited reproduction of this work for the purposes of private study, research, criticism, review and news reporting is likely to be in accordance with the law, particularly if cited appropriately.

# Approval

| | |
|---|---|
| **Name:** | **Ghassan Mousa** |
| **Degree:** | **Doctor of Philosophy** |
| **Title:** | ***Fuel Cell Diagnostic using Electrochemical Impedance Spectroscopy*** |
| **Examining Committee:** | **Chair:** Jiacheng (Jason) Wang<br>Assistant Professor |

**Dr. Farid Golnaraghi**
Senior Supervisor
Professor

**Dr. Jake Devaal**
Supervisor
Product Safety
Ballard Power Systems

**Dr. Erik Kjeang**
Supervisor
School of Mechatronics Systems Engineering

**Dr. Krishna Vijayaraghavan**
Internal Examiner
Assistant Professor
School of Mechatronics Systems Engineering

**Prof. Farrokh Sassani**
External Examiner
Professor
Mechanical Engineering Department
University of British Colombia

**Date Defended/Approved:** September 2, 2014

# Partial Copyright Licence

The author, whose copyright is declared on the title page of this work, has granted to Simon Fraser University the non-exclusive, royalty-free right to include a digital copy of this thesis, project or extended essay[s] and associated supplemental files ("Work") (title[s] below) in Summit, the Institutional Research Repository at SFU. SFU may also make copies of the Work for purposes of a scholarly or research nature; for users of the SFU Library; or in response to a request from another library, or educational institution, on SFU's own behalf or for one of its users. Distribution may be in any form.

The author has further agreed that SFU may keep more than one copy of the Work for purposes of back-up and security; and that SFU may, without changing the content, translate, if technically possible, the Work to any medium or format for the purpose of preserving the Work and facilitating the exercise of SFU's rights under this licence.

It is understood that copying, publication, or public performance of the Work for commercial purposes shall not be allowed without the author's written permission.

While granting the above uses to SFU, the author retains copyright ownership and moral rights in the Work, and may deal with the copyright in the Work in any way consistent with the terms of this licence, including the right to change the Work for subsequent purposes, including editing and publishing the Work in whole or in part, and licensing the content to other parties as the author may desire.

The author represents and warrants that he/she has the right to grant the rights contained in this licence and that the Work does not, to the best of the author's knowledge, infringe upon anyone's copyright. The author has obtained written copyright permission, where required, for the use of any third-party copyrighted material contained in the Work. The author represents and warrants that the Work is his/her own original work and that he/she has not previously assigned or relinquished the rights conferred in this licence.

Simon Fraser University Library
Burnaby, British Columbia, Canada

revised Fall 2013

# Abstract

When a proton exchange membrane (PEM) fuel cell runs short of hydrogen, it suffers from a reverse potential fault. This fault, driven by neighboring cells, can lead to anode catalyst degradation and, through cell reversal, to holes in the membrane due to local heat generation. As a result, hydrogen leaks through the electrically-shorted membrane-electrode assembly (MEA) without being reacted, and it recombines directly with air. This recombination results in a reduction in oxygen concentration on the cathode side of the MEA and a fuel cell voltage reduction. Such voltage reduction can be detected by using electrochemical impedance spectroscopy (EIS).

In this research, in order to fully understand the effect of this oxygen reduction fault, the impedances of single and multi-cell stacks at different leak rates were measured. Then the impedance signatures were compared with the signatures of stacks having non-leaky cells at different oxygen concentrations with the same current densities. The signatures were analyzed by fitting the leaky stacks and oxygen concentrations impedance data sets with the parameters of a Randles circuit. The correlation between the parameters of the two data sets allows us to understand the change in impedance signatures with respect to a reduction of oxygen in the cathode side. Using the circuit parameters, a model that establishes a relationship between impedance and voltage was also considered. With the help of this model along with the impedance signatures, we are able to detect the reduction of oxygen concentrations at the cathode by using fuzzy logic (FL). However, resolution of detection was reduced with the reduction of leak rate and/or increases in the stack cell-count. The amount of hydrogen leak rates were quantified by simulating the resulting reduced amount of oxygen with the use of neural network (NN) method.

Successful implementation of FL and NN methods in a fuel cell system can result in an on-board diagnostics system that can be used to detect and possibly prevent cell reversal failures, and to permit understanding the status of crossover or transfer leaks versus time in operation. Using such system will increase the reliability and performance of fuel cell stacks, where leaks can be detected online and appropriate mitigation criteria can be applied.



**Keywords**: PEM fuel cell; Hydrogen Crossover; Oxygen concentration; EIS; Neural network; Fuzzy logic

*To my wife Abrar, my mother Zeyad, and my four kids Mariyah, Hamzah, Zeyad and Hashem, I extend my deep sincerity and appreciation. Without you standing by my side I would not have been able to cross the finish line. Thank you for all your unconditional love and support.*

# Acknowledgements

Throughout my graduate studies, I went through the difficulty of living in a new culture while studying in a new environment and establishing new relationships. This fresh start gave me the opportunity to revaluate my thoughts about life, career and social responsibility. The effort I have invested to tackle the research through years allowed me to see life without boundaries, barriers and limitations. Having this unbounded spirit, I will continue working toward the better future for my country and my people.

I would like to start my acknowledgment by praising the creator, almighty Allah to whom I surrender all my power and effort. Without His ultimate blessings I would not have been able to achieve any of my accomplishments.

It was my great honor to work under the supervision of Professor Farid Golnaraghi who introduced me to the unique opportunity of working in this industrial research project. His wide research experience gave me the confidence I needed to handle the aspects of this multidisciplinary research. I also appreciate his firm skills in management that allowed walking through my PhD with minimal risks.

This research would not have been completed without the help of Dr. Jake DeVaal who put me on track from the very beginning of the project. His vast industrial experience and knowledge allowed me to understand the fuel cells and act upon my understanding in a practical way. I acknowledge his kindness, cooperation and support over my PhD period.

I would like to extend my acknowledgment to the external examiner Professor Farrokh Sassani for his participation in my defense committee. I am grateful for the informative discussions I had with Dr. Amir Niroumand, Prof. Erik Kjeang and Alan Young. Their solid knowledge in fuel cells and its applications allowed me to perform the required steps needed for the success of this work.

The experimental work done in this research was not possible without the help of Daniel Zwart, Romina Mahboub and Oldooz Pooyanfar. Daniel's hands on experience, Romina's

patience and Oldooz's accuracy were very important for the successful implementation of the experiments.

Including all the people who eased my hatchment by a pleasant smile, held the door wide open to carry on, altered my decisions by a good advice, my acknowledgment list is quite long. For all my friends, colleagues and everyone who gleamed my way for a moment, I am grateful forever to all of you.

Finally, I would like to thank Canada for giving me the chance of pursuing my research in its prestigious institutes. I also would like to thank the administration in Ballard Power Systems for giving me the opportunity to learn in its one of a kind R&D lab. I am very grateful for the scholarship I have received from King Abdulaziz University during my graduate studies.

# Table of Contents

Approval ..... ii
Partial Copyright Licence ..... iii
Abstract ..... iv
Dedication ..... v
Acknowledgements ..... vi
Table of Contents ..... viii
List of Tables ..... x
List of Figures ..... xi
List of Acronyms ..... xiv

**Chapter 1. Introduction ..... 1**
1.1. Motivation ..... 1
1.2. Objective ..... 2
1.3. Literature review ..... 3
1.3.1. Fuel and air starvation ..... 3
1.3.2. Detection techniques ..... 6
Voltage loss ..... 6
AC impedance ..... 7
1.3.3. Artificial intelligence systems ..... 10
1.4. Test outline ..... 11
1.5. Contributions ..... 11

**Chapter 2. Theory and background ..... 13**
2.1. PEM fuel cells ..... 13
2.1.1. Electrochemistry background ..... 13
Open circuit voltage ..... 15
Polarization curve ..... 16
2.1.2. Fuel cell stack module ..... 17
2.2. An Overview of EIS ..... 18
2.2.1. Nyquist plot ..... 19
2.2.2. Impedance measurement ..... 20
2.3. Artificial intelligence ..... 22
2.3.1. Neural network ..... 22
NN structure ..... 22
NN training ..... 24
2.3.2. Fuzzy logic ..... 26

**Chapter 3. Experiment Implementation of EIS ..... 30**
3.1. Experimental setup ..... 30
3.2. Results and discussion ..... 35

3.2.1. Impedance of a single cell ..... 35
Changing hole location ..... 37
Oxygen concentration and dP ..... 39
3.2.2. Impedance of multi-cell in a stack ..... 44
Air starvation ..... 44
Oxygen concentration and dP ..... 49
Measured leak rate ..... 56
3.3. Conclusion ..... 59

**Chapter 4. Design and Implementation of a Neuro/Fuzzy EIS diagnostic system ..... 61**
4.1. Estimation of hydrogen leak rate ..... 61
4.2. Modeling the impedance signature ..... 66
4.3. Detecting hydrogen leak ..... 69
4.4. Conclusion ..... 74

**Chapter 5. Conclusions ..... 76**

**References ..... 81**

Appendix A. Impedance of 20A load ..... 88
Appendix B. Impedance of 50A load ..... 106
Appendix C. MATLAB codes ..... 123

# List of Tables

Table 3.1: The test plan.....31
Table 3.2: The fuel cell operating conditions .....35
Table 4.1: Target vectors of n-cell stack network.....63

# List of Figures

Figure 2.1. Schematic diagram of a PEM fuel cell .....14
Figure 2.2: Typical polarization curve of PEM fuel cell with overpotential losses .....16
Figure 2.3: Randles circuit .....19
Figure 2.4: Nyquist plot .....20
Figure 2.5: Schematic representation of the neural network structure .....23
Figure 2.6: Sigmodial function .....23
Figure 2.7: Schematic of fuzzy logic system .....27
Figure 2.8: The membership function of a fuzzy set .....27
Figure 3.1: Schematic view of the test bed .....32
Figure 3.2: The single-cell fuel cell stack .....33
Figure 3.3: The test bed .....34
Figure 3.4: Impedance of a normal cell at 20, 50 and 125 A load .....36
Figure 3.5: Equivalent fuel cell circuit for experimental fitting .....37
Figure 3.6: Effect of differential pressure on the parameters of the 50A load inlet (top) and outlet (bottom) ports. .....38
Figure 3.7: Impedance of a normal cell at 50 A load .....39
Figure 3.8: 20A impedance of the normal cell and leaky cells with inlet holes for 13% O2 concentration .....40
Figure 3.9: 20A impedance of the medium leaky with holes located at the inlet at different dP .....41
Figure 3.10: 50A impedance of the medium leaky with holes located at the inlet at different dP .....41
Figure 3.11: Effect of oxygen concentration (top) and dP (bottom) on the parameters of the 20A load, .....43
Figure 3.12: 20A impedance of a 9-cell normal stack at different oxygen concentration .....45
Figure 3.13: 20A voltage of a 9-cell normal stack at different oxygen concentration .....46
Figure 3.14: 50A impedance of 19-cell short stack with large leaky cell at different dP .....47
Figure 3.15: 50A voltage of 19-cell short stack with large leaky cell at different dP .....47

Figure 3.16: A schematic diagram of experimental setup .....48
Figure 3.17: 20A impedance and hydrogen at the outlet of a 9-cell stack with a medium leak cell .....49
Figure 3.18: Randles model .....50
Figure 3.19: 20A impedance of a large leaky cell with 5-cell stack at different oxygen concentration (left) and dP (right) .....50
Figure 3.20: The parameters of 20A 5-cell stack of oxygen concentration (left) and dP (right). .....51
Figure 3.21: Oxygen concentration impedance signatures at 20A load of a 9-cell stack .....52
Figure 3.22: dP Impedance at 20A load of a 5-cell stack (a) and 19-cell stack (b) with a large leaky cell .....53
Figure 3.23: dP Impedance at 20A load of a 5-cell stack with medium leaky cell .....53
Figure 3.24: 20A impedance of a large leaky cell with 19-cell stack at different oxygen concentration (left) and dP (right) .....54
Figure 3.25: The parameters of 20A large leaky cell with 19-cell stack of oxygen concentration (left) and dP (right). .....55
Figure 3.26: Effect of differential pressure on the parameters of 19-cell stack with medium leak MEA. .....55
Figure 3.27: Effect of differential pressure on the parameters of 19-cell stack with small leak MEA. .....56
Figure 3.28: A schematic diagram of experimental setup .....56
Figure 3.29: dP Impedance of a single cell and injected hydrogen at 20A load .....57
Figure 3.30: dP Impedance of a single cell and injected hydrogen at 50A load .....58
Figure 3.31: dP versus hydrogen leak rate of a medium leaky cell during off-line .....59
Figure 3.32: dP versus time (a) and hydrogen flow versus time (b) .....59
Figure 4.1: A schematic diagram of neural network training .....61
Figure 4.2: Neural network topography 112:20:3 .....63
Figure 4.3: Oxygen concentration (left) and hydrogen leak rate (right) of a small leaky cell in n-cells stack .....64
Figure 4.4: Oxygen concentration (left) and hydrogen leak rate (right) of a medium leaky cell in n-cells stack .....65
Figure 4.5: Oxygen concentration (left) and hydrogen leak rate (right) of a large leaky cell in n-cells stack .....65
Figure 4.6: Measured and estimated leak rates .....66

Figure 4.7: Estimated and measured voltages of a 19-cell stack at 20A at low oxygen concentration ..... 68

Figure 4.8: Estimated and measured voltages of a 9-cell stack at 20A at air starvation ..... 69

Figure 4.9: Estimated and measured voltages of a 19-cell stack at 20A load with large leaky cell. ..... 69

Figure 4.10: Estimated and measured voltages of a 19-cell stack at 20A. ..... 70

Figure 4.11: Estimated and measured voltages of a 9-cell stack at 20A t air starvation ..... 71

Figure 4.12: Fuzzy membership functions of a 9-cell stack at 20A. ..... 72

Figure 4.13. Impedance signatures of a 19-cell stack and its estimated voltages with two leaky cells (medium and starved cell) ..... 74

# List of Acronyms

| | |
|---|---|
| BP | backpropagation algorithm |
| ccm | cm^3/min |
| CPE | constant phase element, F |
| CVM | cell voltage monitoring |
| dP | differential pressure, psig |
| EIS | electrochemical impedance spectroscopy |
| FC | fuel cell |
| FL | fuzzy logic |
| GLD | gas diffusion layer |
| HD6 | heavy duty motive power hydrogen fuel cell form Ballard power system |
| HOR | hydrogen oxidation rate |
| MEA | membrane-electrode assembly |
| MFC | mass flow controller |
| MLP | multi-layer perceptron |
| NN | neural network |
| OCV | open circuit voltage, V |
| ORR | oxygen reduction rate |
| PEM | proton exchange membrane |
| SLPM | standard liter per minute |
| stoich | stoichiometry |

**Symbols**

| | |
|---|---|
| $a$ | Tafel constant |
| $A$ | load, A |
| $b$ | bias input to the neuron network |
| $C$ | capacitance, F |
| $C_{air}$ | air consumption, 0.0167 SLPM/A/cell |
| $C_{dl}$ | double-layer capacitance, F |
| $\Delta \bar{g}_f$ | Gibbs free energy |

| | |
|---|---|
| $dV_{est}$ | differential estimated voltage, V |
| $dV_{meas}$ | differential measured voltage, V |
| e | electron charge, $1.602 * 10^{19}$ Coulombs |
| $E$ | reversible open circuit voltage, V |
| $E^0$ | open circuit voltage at standard pressure, V |
| $E_{act}$ | electrode potential, V |
| *flow* | air flow of 20 and 50 A loads; 1.03 and 1.78 SLPM respectively |
| $F$ | faraday constant, 96500 Coulombs |
| $h_w(x)$ | neural network prediction |
| $i$ | current density, A |
| $i_0$ | exchange current density, A |
| $J(w)$ | cost function |
| $n$ | number of features in the training set |
| $N$ | number of cells in the fuel cell stack |
| $o$ | neural network output |
| $O_{2L}$ | oxygen left in the cathode, SLPM |
| $O_2\%$ | percentage of oxygen concentration at the cathode side |
| P | pressure, psig |
| $P_{H_2}$ | hydrogen partial pressure, P |
| $P_{H_2O}$ | water vapor partial pressure, P |
| $P_{O_2}$ | oxygen partial pressure, P |
| $Q_{H2}$ | hydrogen leak rate, SLPM |
| $R_n$ | fuzzy rules |
| $R$ | universal gas constant, $8.314\ JK^{-1}/mol$ |
| $R_{ct}$ | charge transfer resistance, ohm |
| $R_{HF}$ | high frequency resistance, ohm |
| $R_{mt}$ | mass transfer resistance, ohm |
| T | neural network targets |
| u (x) | fuzzy input value |
| u (y) | crisp value |
| $w$ | neural network weight |

| | |
|---|---|
| $x$ | neural network input |
| $X$ | input fuzzy set |
| $Y$ | output fuzzy set |
| $Z_{imaginary}$ | imaginary impedance axis, ohm |
| $Z_{real}$ | real impedance axis, ohm |

**Greek**

| | |
|---|---|
| $\lambda_{H2}$ | hydrogen stoichiometry |
| $\alpha$ | neural network learning rate |
| $\mu(x)$ | membership fuzzy degree |
| $\tau$ | time constant |

# Chapter 1.

# Introduction

Fuel cells transform chemical energy into electrical and thermal energy by electrochemical reaction that takes place in between electrodes and an electrolyte. In PEM fuel cells, hydrogen oxidation takes place on the anode side while oxygen reduction occurs at the cathode. After oxidation, hydrogen protons move from the anode to the cathode with the help of a thin layer of ion-conducting catalyst and electrons flow out of the cell to produce energy. In order to come up with enough power to satisfy the load, fuel cells are usually stacked in series.

PEM is one of the most important types of fuel cells due to its ability to work at low temperature, and its low weight and volume. This has made PEM fuel cells a competitive alternative power source in stationary and automotive applications. However, the extensive use of PEM fuel cell mainly depends on their reliability and cost efficiency. Over the years, the fuel cell industry has developed more durable membrane electrode assemblies (MEAs) to avoid failures and extend the operating lifetime. However, while the onset of membrane degradation can be delayed, the initiation of MEA pinholes is inevitable with existing technology measures. As a result, hydrogen crossover through the pinholes is eventually expected.

## 1.1. Motivation

Ballard Power Systems uses $6^{th}$ generation FCvelocity$^{TM}$-HD6 Modules that utilize state of the art automotive PEM stacks to power many buses around the world. This module contains multiple unit cells in series that are used to provide large amounts

of power; i.e. to the order of 10's of kW. Fuel cell system design targets optimum operating conditions and efficient systems to ensure sufficient humidification, and air and fuel supplies. However, if the reactant feed does not respond to the current demand fast enough such as during sudden load increases and/or start-up/shutdowns, full or transient fuel starvation may occur, causing cathode or anode degradation. Cells containing transfer or crossover leaks are at greater risk of fuel starvation.

Because of the large size and a lack of appropriate models, Ballard requires a diagnostic tool that is able to detect hydrogen leak in operation and quantify its rate effectively. In the current HD6 module, the safe threshold of hydrogen internal leaks can be detected using hydrogen sensors in the downstream cathode exhaust. Unfortunately, those sensors are expensive and not reliable over long periods of time. Knowing the amount of hydrogen crossover during operation will allow us to establish mitigation criteria to reduce its effect on stack performance. The goal of this project has been to arrive at a more reliable diagnostic technique for Ballard bus fuel cell modules to monitor hydrogen leakage online.

## 1.2. Objective

The objective of this research is to detect hydrogen crossover in a multi-cell stack during operation by using a proper diagnostic system that can efficiently identify the fault. An ideal system is a durable and efficient diagnostic tool that detects the advent of a significant hydrogen leak causing potentially flammable emissions, or smaller crossover leak levels to inform service staff that repairs are needed. Ultimately, this system is intended for Ballard's bus fuel cell modules to increase their overall reliability.

In this research, we intend to develop a proper diagnostic technique that continuously monitors hydrogen crossover by:

1 Identifying the type of signals able to detect hydrogen crossover in a multi-cell stack. The signals must be sensitive to leak rates at considerable stack size.

2 Conducting tests at different leak rates, oxygen concentrations and stack sizes to establish correlations between the identified signals and identify its resolutions.

3 Analyzing the signals to select appropriate features that are able to correctly recognize the leak while having minimal number of features to reduce computational load and the size of the diagnostic system.

4 Developing an accurate model to estimate the leak rate in the stack. This model will then be used to establish a diagnostic system that detects the crossover, identifies its intensity and estimates its amount.

## 1.3. Literature review

### 1.3.1. Fuel and air starvation

Internal combustion engines transform chemical energy into thermal energy and then mechanical work while fuel cells transform chemical energy into electrical work. As government agencies and organizations regulate combustion engine emissions to reduce greenhouse gas effects, the automotive industry will move to rely on alternative approaches. One approach is to use battery-powered electrical vehicles. However, the high initial cost, short driving range, long charging time and reduced passenger and cargo space have proved the limitation of battery-powered vehicles [1]. Another approach is the use of fuel cells (FC). Producing only water as a byproduct, FCs supply constant power when provided sufficient oxidant and fuel flows.

The FC was first demonstrated by Sir William Grove in 1839. He used separate platinum electrodes in oxygen and hydrogen gas, submerged in a dilute sulfuric acid electrolyte [2]. With the increasing knowledge of electricity, Sir Francis Bacon achieved in 1932 a high short-term power density of 0.66 $W/cm^2$ using an alkaline FC system. Low temperature PEM was first invented by William Grubb at General Electric in 1955. The use of PEM fuel cells were boosted through the development of MEAs led by researchers at Los Alamos National Laboratory in 1980s, enabling an-order-of magnitude reduction in noble metal catalyst. This was a major breakthrough, along with the ongoing environmental concerns, that led to continuing development in PEMFCs.

Beside PEM fuel cells, other types are used in an industry scale. Direct methanol fuel cell (DMFC) is generally used in portable applications as an alternative to lithium ion batteries. Similar to PEMFCs, it uses a polymer electrolyte membrane. However, the use of a liquid combination of water and methanol simplifies fuel storage. Solid oxide fuel cell (SOFC) operates at high temperature; 800-1000° C and uses inexpensive catalyst. This made it mostly applicable for stationary applications. Other types of fuel cells such as biological based fuel cells utilize the bacterial oxidation of organic material to generate electricity.

In PEM fuel cells, the membrane must be well hydrated for an efficient migration of hydrogen protons. If the membrane is dry, its conductivity is reduced. This leads to a decrease in the surface area possible for the electrochemical reaction, and a reduction in the fuel cell's potential. Eventually, cracks might be created at the membrane, and hydrogen can then directly combine with oxygen at the cathode side. If the membrane is flooded with water, it prevents the electrochemical reaction and the fuel cell potential is reduced. Thus drying out and flooding are important faults to be monitored. However, following proper water management techniques, the probability of those faults can be minimized.

During shut-down periods hydrogen is consumed by air that diffuses to the anode catalyst layer. Upon start-up, hydrogen mixes with the stagnant air and creates transient starvation of cells as the hydrogen supply is replenished at the anode. While the cell is starving of hydrogen, its local current density at the inlet can become very high. This increase in the local current increases the temperature near the inlet. As a result, pin-holes at the cell inlet are initiated [3]. Full fuel starvation can also result in reverse potential faults, where normal operating cells push current through the fuel starved cell. This causes a rise in the anode potential to the potential required to oxidize water or the anode catalyst carbon support:

$$2H_2O \rightarrow O_2 + 4H^+ + 4e^- \qquad (1.1)$$

$$C + H_2O \rightarrow CO_2 + 2H^+ + 4e^- \quad (1.2)$$

The protons then pass through the membrane to the cathode to produce hydrogen:

$$2H^+ + 2e^- \rightarrow H_2 \quad (1.3)$$

Tang *et al.* [4] studied the effect of fuel starvation on the fuel cell during start up and noticed a reduction of the catalysts surface areas over time. Carbon oxidation of the catalyst support reduces the catalyst active area due to agglomeration and also reduces the catalyst layer thickness, which often causes mass transport degradation. Other causes of membrane degradation might result from mechanical stresses or insufficient hydration. This usually leads to cracks in the fuel cell and eventually fuel starvation. Yousfi-Steiner *et al.* [5] reviewed the causes and consequences of fuel cell starvation faults in detail.

At sufficient rates of hydrogen cross-over leak, the fuel cell performance drops due to the direct recombination with reactant oxygen on the cathode side. This recombination affects the available amount of oxygen used for the electrochemical reaction. In severe cases, the fuel cell might suffer fuel and/or air starvation. Direct recombination of fuel with oxygen results in the formation of water on the cathode side. This was verified in a separate study [6] where a 10-cell stack was run with large hydrogen transfer leak, leading to air starvation of the affected cell because of the consumption of oxygen and/or water accumulation in the cathode. Kreitmeier *et al.* [7] studied the permeability of an MEA with one 10 µm pinhole as a function of gas humidity. The authors showed that, with the increase of the helium leak-testing gas relative humidity, the membrane swells and the size of the pinhole is reduced. When the humidity reached 100%, the helium crossover is completely eliminated. It was concluded that the reduction of helium leak was the result of water sealing off the pin-holes.

In our study, running the stack at large amounts of hydrogen leaking through the MEA showed no external emission of hydrogen in the stack cathode outlet. In contrast, when the fuel cell starves of air, the existence of hydrogen at the outlet was detected. This

agrees with the literature that when the fuel cell starves of oxygen, hydrogen protons pass through the MEA and combine directly with electrons at the cathode side [8, 9], in a phenomena called hydrogen pumping [10].

$$H_2 \rightarrow 2H^+ + 2e^- \qquad (1.4)$$

Similar to equation (1.3), hydrogen will be produced at the cathode side. Thus, with a scarcity of oxygen concentration, the stack will pump large amount of hydrogen rates that might pass the critical threshold of acceptable external leak rates. Using the impedance signature and the stack voltage we were able to recognize this fault precisely.

### 1.3.2. Detection techniques

#### *Voltage loss*

When the fuel cell starves of hydrogen, its anode and cathode potentials rise and drop respectively. In such a fault, the voltage of a single starved cell drops to zero [3]. If a hydrogen starving cell is placed in a stack, its voltage drops to negative values due to the high anode potential. The effect of fuel starvation on a large PEM fuel cell was studied by Liang *et al.* [11]. When the cell is air starved however, its voltage drops to almost zero with an anode potential little higher than the cathode [12]. Zhang *et al.* [3] studied the effect of fuel and air starvation on the voltage along a single PEM fuel cell. Reducing the air stoich to 1.5, the cell voltage drops due to the lack of oxygen concentration. As concentration drops along the flow channel, lower local current density was observed at the downstream of the cell. Running the cell at lower hydrogen stoich, the current density dropped sharply to zero at the downstream of the cell due to the insufficient hydrogen along the cell.

The prior-art dealing with MEA pinholes is limited in the literature. Weber [13] developed a mathematical model to simulate the effect of pinholes in a PEM fuel cell. He showed the performance drop in terms of cell voltage and current density. The drop in current density was also considered by Lin *et al.* [14]. Hydrogen leaks can also be

detected by the increase of leak current and drop in voltage [15, 16]. Khorasani *et al.* [17] and Tian *et al.* [18] studied the output voltage and pressure difference between anode and cathode to localize the leaky MEA in a small stack. The authors noticed a decrease in the voltage of the defected cell when increasing the anode pressure. This decrease in voltage resulted from the increased amount of hydrogen leak rate through the MEA, which results in depletion of oxygen in the cathode.

Wu *et al.* [19] reviewed several diagnostic techniques that can be used to detect fuel cells faults such as cell voltage monitoring (CVM) and electrochemical impedance spectroscopy (EIS). While CVM technique measures the voltage of each cell in the stack, it cannot be used to detect the voltage on board vehicles due to reliability issues. Our study also shows that the use of voltage in detecting small hydrogen leaks is not feasible, where the degraded voltage is very minimal with the gradual increasing of leak rates.

Cyclic voltammetry (CV) as a diagnostic tool was used in [20] to measure the active catalyst surface area that is reduced during starvation. The authors conducted tests at 50, 100, 250 and 500 reverse cycles. With increasing number of cycles, the fuel cell performance reduces due to the oxidation of carbon loss in the catalyst layer. CV records the current while sweeping the fuel potential back and forth between two sets of voltage limits. This method is usually used off-line while the fuel cell dynamic behavior cannot be controlled during operation.

### *AC impedance*

EIS or (AC impedance) is an experimental technique that can be used to perform impedance measurements over a wide frequency range for DC power generation devices during operation. The main advantage of EIS is the possibility to resolve, in the frequency domain, the individual contributions that affect the overall PEM fuel cell performance under load conditions [21]. Toward an understanding of the impedance signatures, we used, along with other researchers [22, 23], a Randles circuit to fit the experimental data. This circuit consists of a resistor in series with a resistor and double layer capacitance ($C_{dl}$) in parallel.

More complex circuits than the Randles circuit are proposed in the literature for different purposes. Researchers [21, 22, 24] have added additional elements to the Randles circuit to include mass transfer effects. Series connections represent subsequent events while parallel connections represent simultaneous events. Makharia *et al.* [25] used a transmission line circuit to include the catalyst layer resistance. Cano-Castillo *et al.* [26] compared the transmission line circuit with a circuit similar to the ones used by [21] and [24], where they added a resistive and capacitive element to the Randles circuit. Both the transmission line and the modified Randles circuit gave reasonable fits with the experimental data. Another equivalent circuit variant in [23] represented the mass transport phenomena with a Warburg impedance element in series with the Randles circuit.

More precise fit can be achieved by using a constant phase element (CPE) instead of $C_{dl}$ [27]. Andreasen *et al.* [28] used two Randles circuits with a CPE instead of a capacitor in the second circuit. The authors showed that using the circuit with the CPE fitted better to their impedance data. Others [29, 30, 31] also replaced capacitive elements with CEPs to adapt fitting their models to the deformed impedance arc. This deformation results from the porous structure of the electrodes where the electron charges are not distributed evenly inside the electrode. However, the lack of physical interpretation of CPE elements has limited its use in the literature. Fouquet [32] replaced the CPE with an increased order of the Randles model by adding R and C elements of the transmission line. This resulted in a better fit to the impedance data compared to the normal Randles model. However, more computational power was needed due to the complexity of the model.

Jespersen *et al.* [31] studied the effect of air and hydrogen stoichiometry; varying the ratio of provided to consumed flow on the impedance. With the lower air stoich, impedance signatures increase. This increase was mainly noticed at the low frequency part. With the lower hydrogen stoich the authors noticed no change in the impedance signatures. They concluded that changing air stoich has a dramatic effect on the ORR

while changing hydrogen stoich has a limited effect on the HOR and thus on the overall performance of the fuel cell.

Schneider *et al.* [33] considered the effect of air starvation on the impedance along a 63 cm2 single PEM fuel cell. At normal air stoich, the impedance spectra had two frequency loops. They suggested that the presence of the second loop indicates significant losses associated with oxygen diffusion through nitrogen in the gas diffusion layer (GDL) [34]. However, the loop increases in size with increasing the depletion of oxygen toward the air outlet. When the air stoich was reduced from 3.5 to 1.4, the loop increased sharply toward the end of the cell outlet. In a previous study done by our group [35], we observed similar behavior of the impedance signature of a single cell with either decreasing oxygen concentration or increasing leak rates. However, the reduction in impedance due to air starvation was not observed because the impedance measurement of a single cell collapsed at zero voltage.

At a stack level, Yan *et al.* [36] measured the impedance of a 20-cells stack with MEA active area of 270 $cm^2$ at reduced air stoich. They noticed that, as the stoich was reduced to 1.5, the impedance enlarged. However, further reduction of air stoich creates improper conditions that effect the fuel cell operation and measurements. Thus, in this research we measured the impedance of a multi-cell stack at reduced oxygen concentrations while keeping constant cathode flow. Driving the stack to air starvation using this method gave us a better understanding of the relationship between oxygen concentration and leak rate while in both cases lesser oxygen was available at the cathode.

Boillot *et al.* [37] studied similar effects on the impedance by diluting hydrogen and oxygen respectively; using nitrogen to change the fuel and oxidant concentrations. In the case of hydrogen dilution, the authors noticed an increase of the impedance arc at high and medium frequency regions with higher amounts of dilution. However, the difference in impedance with lower amounts of dilution was very small. In the case of oxygen dilution, the authors noticed a reduction in impedance with higher amount of

oxygen concentrations, more than 21%, at the low frequency region. However, the effect of concentrations at lower than the normal amount of oxygen in air was not considered. In our study, we reduced the amount of oxygen concentration until the stack reached air starvation.

### 1.3.3. Artificial intelligence systems

Fuzzy logic (FL) is about representing an *approximate* knowledge that cannot be represented by conventional, crisp methods [38]. This approximation gives an advantage to FL over mathematical models that cannot handle the fuzziness in numbers. Its ability to linguistically domesticate the expert knowledge made it easy to be used in control systems. Hissel *et al.* [39] used FL to detect drying and flooding in a FC vehicle. Shumacher *et al.* [40] used FL in water management of a miniature FC stack. Torreglosa *et al.* [41] used FL in energy management of a battery-FC hybrid tramway system. In our work, we established a FL rule-base to detect internal leak rate and hydrogen emission for a multi-cell stack.

Neural network (NN) is widely used in the literature because of its capability as a model-free system. Its demonstrated abilities in training, parallel computation and noise tolerance make it compatible for modeling complicated and nonlinear systems. Among various NN models, the feed-forward NN structure is widely used in literature. Other NN models are proposed in the literature [42, 43, 44]. However, Lobato *et al.* [45] found that multilayer feed-forward gave the best performance when compared with other networks. A special feed-forward NN training algorithm is the multilayer back propagation (BP) algorithm that is commonly used for pattern recognition and classification, and hence for machine fault diagnosis [46].

BP uses a set of input and output data to update the weights of the network in forward and backward directions until the error between the output and target reaches it threshold limits. Steiner *et al.* in [47, 48] used the BP technique in diagnostics of a PEM fuel cell. In their study, the NN was trained using fault free data at different operating

conditions. Then the residual between the fuel cell output and the NN output was calculated. Deviation from the predicted value of the NN was interpreted as a fault. However, the severity of the fault was not considered. In this research we used NN to estimate the amount of internal hydrogen leak in a stack.

## 1.4. Thesis outline

In the next chapters, we will present this thesis as follows. In chapter 2, we start by explaining the theory behind PEM fuel cells and discuss some major sources of voltage loss. Then, we consider EIS; our main diagnostic tool and its associated equivalent circuits. Finally, a brief background of neural network and fuzzy logic is presented as methods used for diagnostic applications in a later chapter.

In chapter 3, we explain the experimental setup used in this research. In this chapter we will prove the ability of the impedance to detect hydrogen leak rate. First, we represent the test-station, operating conditions. Then we discuss the single cell and multi-cell impedance measurements and their associated parameters. At the end of the chapter, we show the results of measured leak rates.

In chapter 4, we introduce the diagnostic system used in this thesis. We start this chapter by showing our technique in estimating leak rate using neural network. Next we present the model that we use to detect hydrogen leak. This chapter ends by representing the fuzzy logic rule-base that we use as a diagnostic technique.

Finally, we conclude our findings in chapter 5 by discussing the limitations of this research and suggesting future work.

## 1.5. Contributions

In this thesis the following contributions were met:

1 Using EIS to detect hydrogen crossover and emission faults in a multi-cell stack.

2 Using Neural network to estimate the hydrogen crossover at different leak rates.

3 Using fuzzy logic to fuse the stack impedance and voltage measurements in a non-intrusive diagnostic system.

The thesis outcomes are:

1 Ghassan Mousa, Daniel Zwart, Farid Golnaraghi, "Fuel Cell Bus Diagnostic System," poster was posted at the NSSERC May 2011.

2 Ghassan Mousa, Farid Golnaraghi, Jake DeVaal, Alan Young, "Detecting PEM Fuel Cell Hydrogen Leak using EIS Method," paper was published at Journal of Power Sources 246 (2014) 110-116.

3 Ghassan Mousa, Jake DeVaal, Farid Golnaraghi, "Use of Neural Network and EIS Signal Analysis to Quantify H2 Crossover In-Situ in Operating PEM Cells," paper was submitted to the Journal of Power Sources.

4 Ghassan Mousa, Jake DeVaal, Farid Golnaraghi, "Diagnosis of PEM Fuel Cells Hydrogen Crossover and Emission using EIS Method and Fuzzy Logic Technique," paper was submitted to the Interantional Journal of Hydrogen Energy.

5 "Use of Neural Network and EIS Signal Analysis to Quantify H2 Crossover," was filed for US Provisional Patent number USAN 61/941,927. Applicant: Ballard Power Systems. Inventors: Ghassan Mousa, Jake DeVaal, Farid Golnaraghi.

6 Ghassan Mousa, Farid Golnaraghi, Jake DeVaal, "PEM Fuel Hydrogen Leak Diagnostic using Artificial Intelligence," paper was submitted to the World Hydrogen Energy Conference 2014.

# Chapter 2. Theory and background

## 2.1. PEM fuel cells

In this section we will briefly discuss the fuel cells theoretical background and its system. We start with an explanation of the electrochemical reaction. Then we will discuss the fuel cell potential and its associated losses. Finally, a concise demonstration of the fuel cells system is illustrated.

### 2.1.1. Electrochemistry background

FCs use electrochemical reactions to generate the circulation of current through a continuous circuit to produce power (Figure 2.1). The electrochemical reactions occur on the electrode surfaces where ions conduct through the electrolyte. Fuel oxidation occurs due to the loss of electrons in the anode, equation (2.1), and the oxygen reduction occurs due to the consumption of electrons in the cathode, equation (2.2). In PEMFCs, those reactions happen in the MEA.

$$H_2 \rightarrow 2H^+ + 2e^- \qquad (2.1)$$

$$O_2 + 4H^+ + 4e^- \rightarrow 2H_2O \qquad (2.2)$$

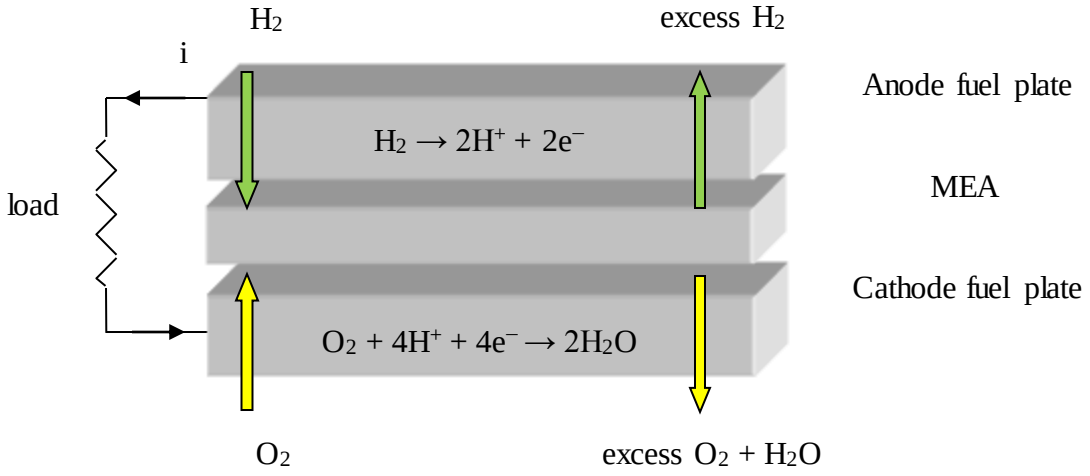


Figure 2.1. Schematic diagram of a PEM fuel cell

The MEA contains gas diffusion layers (GDL), catalyst layers and a membrane. The GDL allows the gas to diffuse in to the catalyst and water to diffuse out. The catalyst layer is where the reaction takes place and it contains porous architecture to allow reactant transportation. The successful reaction occurs between the platinum particles, carbon connection and ionomer coat in the catalyst layer. This is called the 3-points reactions. After the reaction, hydrogen protons pass through the membrane to recombine with oxygen and produce water.

For the fuel cell to work at its designated power capacity, sufficient amounts of fuel and air must be provided. This amount; s*toichiometry* or in short *stoich* is the ratio of the provided flow to consumed flow in the cell, equation (2.3) and it is kept in values more than 1.

$$stoich = \frac{provided}{consumed} \qquad (2.3)$$

Fuel cell reactant flows are usually calculated in a standard liter per minute (SLPM) unit. SLPM is an industry standard where gases are affected substantially by temperature, pressure and RH. This volumetric flow unit is measured at 20˚C, 101 kPa absolute pressure and 36% relative humidity (RH).

### *Open circuit voltage*

The standard voltage of PEMFC in 25˚C and 1 bar is 1.23V. This is the voltage derived from the Gibbs free energy $\Delta\bar{g}_f$ in reversible state. $\Delta\bar{g}_f$ is the energy available to do external work, moving electrons around an external circuit, neglecting any work done by changes in pressure and/or volume. For a reversible state, all the fuel cell energy is transformed into electrical energy with no losses. So:

$$\Delta\bar{g}_f = -2F \cdot E \qquad (2.4)$$

where

$F$ is the Faraday constant, or the charge of one mole of electrons; and it is equal to 96485 C.

$E$ is the reversible open circuit voltage (OCV) of the fuel cell.

The value of $E$ at various temperatures and liquid or gas states of water product is tabulated in the fuel cell textbooks.

To take into consideration the change in $\Delta\bar{g}_f$ with respect to reactant pressure and concentration, the Nernst equation is used. Considering the general reaction of hydrogen/oxygen, the fuel cell potential is provided by:

$$E_{cell} = E^0 + \frac{RT}{2F} ln\left(\frac{P_{H_2} \cdot P_{O_2}^{\frac{1}{2}}}{P_{H_2O}}\right) \qquad (2.5)$$

where

$E^0$ is the open circuit voltage at standard pressure

R is the universal gas constant; 8.314 $JK^{-1}\,mol^{-1}$

$P_{H_2}$, $P_{O_2}$ $P_{H_2O}$ are the partial pressures of the gas mixtures.

Using equation (2.5), the reversible cell voltage can be calculated at a given temperature and pressure.

### *Polarization curve*

In its equilibrium state, the fuel cell thermodynamic potential is described by equation (2.5) where no current was obtained. However, during cell operation, overpotential losses are noticed, see Figure 2.2. At low currents, the FC tends to overcome the activation energy required to initiate the reaction. Thus, the cell voltage drops nonlinearly due to the transfer of electrons to or from the electrode. At moderate currents, the voltage drops due to the ohmic loss resulting from the resistance to the flow of electrons through the MEA. This drop in voltage is usually linear. At high currents, the cell voltage drops faster due to insufficient reactants that are needed to satisfy the electrochemical reaction. This loss is called mass transport or concentration loss. Beside those losses, FCs may also lose some of its potential due to improper operating conditions and/or faults such as insufficient water contents, improper operating temperature, existence of holes, etc.

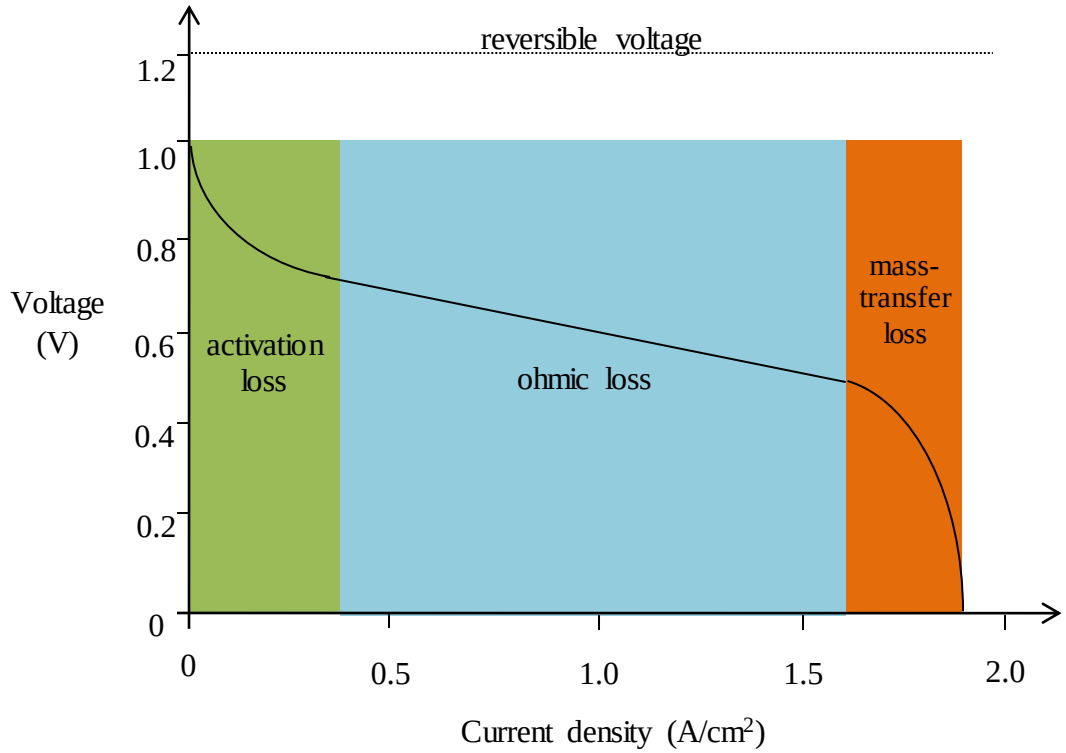


Figure 2.2: Typical polarization curve of PEM fuel cell with overpotential losses

In the activation region, the electrodes activity are taken place even at zero current density where a continual forwards and backwards flow of electrons to and from the electrolyte is flowed [49]. The current resulting from this flow of charges is known as an *exchange current density* $i_0$, equation (2.6). Tafel reported in 1905 that the overpotential at the surface of an electrode plotted against current density represented a straight line. This logarithmic kinetic response to current is commonly described by:

$$E_{act} = a \log\left({}^{i}/_{i_o}\right) \qquad (2.6)$$

where

$E_{act}$ : electrode potential (V)
$i$ : current density (A)
$i_o$: exchange current density (A)
$a$ : Tafel constant

To reduce the loss in the activation region, fuel cell manufacturers tend to increase the value of $i_0$ by raising the cell temperature, using effective catalyst, etc. Increasing $i_0$ has the effect of raising the cell potential and its actual OCV value. Another factor that affects OCV is the fuel cell crossover. This loss happens due to the waste of some internal electrons as a result of fuel migrating through the electrolyte.

### 2.1.2. Fuel cell stack module

In order for the FC stack to work, it needs to be supported by a system that keeps it running. The HD6 system module used by Ballard Power Systems can be categorized into the following main parts:

1 Stack
2 Fuel subsystem
3 Air subsystem
4 Coolant subsystem
5 Control subsystem

Air relative humidity circulating into the stack is controlled by a humidifier. To have a better stack efficiency and humidification, a heat exchanger is used to heat up the humidified air going into the stack. While air temperature cools down on exit, it condenses and excess water is collected out of the system. The coolant fluid used in the stack is a mixture of de-ionized water and Glycol. This mixture prevents the development of ground faults through the coolant and the freezing of coolant at very low ambient temperatures. The coolant conductivity has to be maintained at low levels at all times. Thus, the vehicle control system keeps track of any ground faults in the module or other high voltage systems.

In the fuel side, hydrogen coming out of the stack is re-circulated through the anode in what is called the anode loop. To avoid the effect of accumulated depleted gases, a solenoid valve is used at the stack outlet for purging. A pre-established purge model is programmed into the HD6 module to control the purge algorithm. The purge timing is controlled based on the current output from the stack. At the stack outlet, two hydrogen sensors are used, at the cathode outlet and at the ventilation outlet. These sensors are used to ensure that the hydrogen percentage in the cathode and vent exhaust is less than 4%. A smoke detector is also installed in the vent outlet as safety precaution. A small stirring fan is used to eliminate any dead-zones in the module where hydrogen might build up in the case of leak, and a larger vent fan is used to force-ventilate the module.

## 2.2. An Overview of EIS

As described in the Introduction section, Impedance spectroscopy has the ability to characterize many of the electrical properties of materials and their interfaces with electrodes. This ability has made the EIS technique widely used in modeling and diagnostics of PEM fuel cells, where individual contributions affecting cell performance can be distinguished by fitting the impedance spectrum to parameters of an equivalent circuit model. Electrical circuits with different configurations, components, and degree of

complexity have been proposed in the literature. In our study, the use of Randles circuit in fitting the impedance signatures made the understanding of the stack behavior easier. The fitting was made by using Zplot software.

### 2.2.1. Nyquist plot

Parameters used in the Randles circuit are shown in Figure 2.3. $C_{dl}$ is the double layer capacitance of the catalyst surface, and it represents the build-up of charges on the electrode/electrolyte interface. Due to this capacitive element, the operating voltage takes some time to reach equilibrium when the current suddenly changes. $R_{HF}$ describes the movement within a conducting media and illustrates the sum of contribution from contact resistance between components and the high frequency resistance of the cell components. $R_{ct}$ is the resistance that occurs when electrons transfer at the electrode/electrolyte interface and it decreases when overpotential increases due to the faster oxygen reaction rate. Kang *et al.* [20] noticed an increase in $R_{ct}$ with increasing the degree of the reverse potential fault in a fuel cell caused by fuel starvation. This increase in the resistance was due to the degradation of the catalyst layer where the reaction site area reduced by the electrical shorting.

This circuit yields to the following transfer function:

$$Z = R_{HF} + \frac{1}{C_{dl}(j\omega)+1/R_{ct}} \qquad (2.7)$$

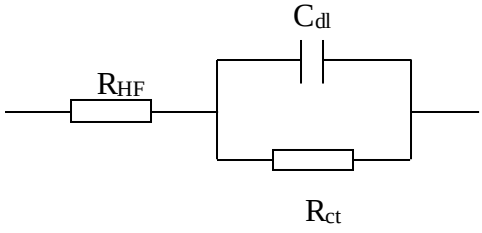


Figure 2.3: Randles circuit

Nyquist plots show the resistance versus reactance at multiple frequencies, as obtained by the EIS measurements, Figure 2.4. The high frequency region of the

impedance spectrum represents the high frequency resistance, whereas the low frequency region represents the high frequency resistance and charge transfer resistance respectively [50]. At high frequency, the $C_{dl}$ is short circuited and the $R_{HF}$ is measured. As frequency decreases, the impedance becomes a combination of resistance and reactance from the capacitive element. At low frequency, $C_{dl}$ acts like a blocking diode and the total resistance is equal to $R_{HF}$ and $R_{ct}$.

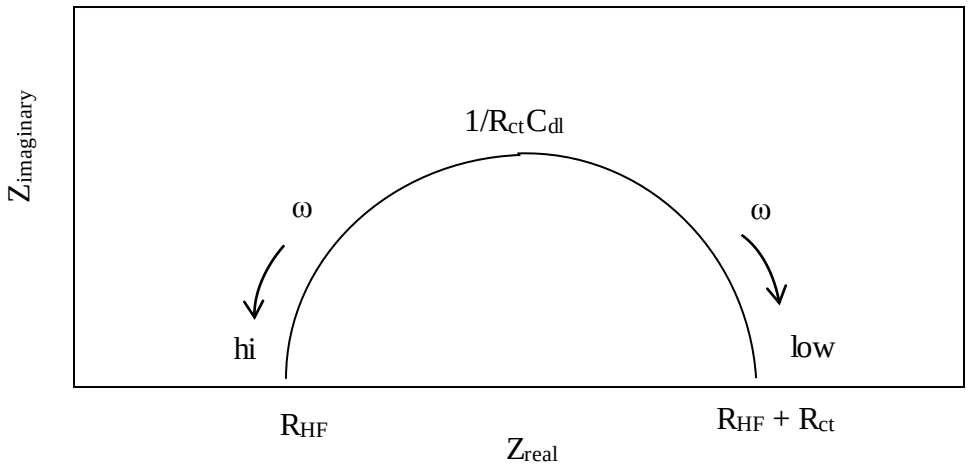


Figure 2.4: Nyquist plot

Our study shows that a single arc Nyquist is applicable when we run the fuel cell at low overpotential either at very high air stoich or with pure oxygen. This arc is called the mass transfer arc and it illustrates the electrochemical reaction dominated by the oxygen reduction rate (ORR) at the cathode. In normal operating conditions however, another arc is introduced to the impedance signature due to the kinetic movements of charges across the fuel cell. This arc represents the high frequency measurements and it is known as the charge transfer arc.

### 2.2.2. Impedance measurement

EIS usually employs a frequency response analyzer (FRA) to apply either a small AC voltage or current perturbation signal to the cell, and measures its output signal for a wide frequency range. The impedance is calculated by dividing the voltage by current, in

the form of a magnitude and phase angle, at each specific frequency. For instance, the Kikisusi fuel cell impedance measurement system used in our work is capable of measuring impedance in the frequency range from 20 kHz to 10 mHz. To fine tune the measurement, the impedance is measured at various moving averages. Using the dedicated load bank, an AC signal in the range of [0.1 - 10] % can be superimposed on the DC load current.

The use of AC current in measuring the impedance is called galvanostatic mode. If AC potential is used instead, the impedance is measured in potentiostatic mode. No significant difference is seen in the results from the two modes, but depending on the application, one mode may be more suitable than the other. The galvanostatic impedance is more suitable for measuring most high-energy electrochemical devices where current levels are high [51]. Impedance measurement is usually preformed in a two-electrode configuration where the EIS reference electrode is connected to the anode. In this configuration, the contribution of an individual electrode cannot be distinguished. This drawback can be omitted due to the fact that cathode polarization is dominant compared to anode polarization where ORR is several orders of magnitude slower than the hydrogen oxidation rate (HOR) [52].

For a stable impedance measurement, linearity and stability must be ensured. To ensure that the impedance measurement is linear, a small AC perturbation is applied to the fuel cell. In fact, using a very small AC signal made it hard for us to measure the impedance due to noise interference. Thus, we superimposed the signal with 10% of the DC current. To keep the fuel cell steady all through the measurement, we conditioned the fuel cell system over quite a long period of time. The impedance measurement was then conducted over a small number of moving average; 4 to reduce the measuring time. Consecutive measurements were taken successively after changing one variable at a time to avoid shifting the fuel cell state over time.

## 2.3. Artificial intelligence

### 2.3.1. Neural network

The brain is capable of performing very complicated tasks such as memorization, identification, calculation, etc. However, brain activity starts from very simple interaction between its computing units; neurons. Neurons are connected to each other by synapses that generate electrical signals. When the signals surpass the threshold of the neural excitation, it propagates to other neurons. With the magnificent number of neurons and connections in the human brain, we are able to grasp knowledge. This knowledge is processed to allow us learn, adapt and estimate new information. Using a similar system that mimics brain activity through the simple interaction between neurons, machines can learn.

***NN structure***

Multilayer perceptron (MLP) neural network is known by its ability to approximate complex nonlinear functions using a number of neurons ordered in layers and connected to each other by weights. Weights are optimally adjusted to map an input/output (or target) relationship in a process called training. In this process, networks use data available beforehand, in what is called supervised training, where data is illustrated to the network. Illustrating the input and output data to the network relates the number of independent and dependent variables respectively, see Figure 2.5. The network final structure is obtained after setting the number of neurons and layers in the hidden layer by trial and error. Once the relationship between input/output is established, the weights are fixed and the network is able to predict outputs from a new set of inputs.

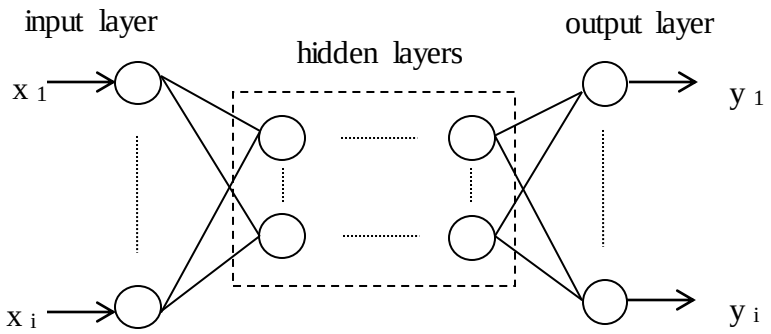


Figure 2.5: Schematic representation of the neural network structure

At the hidden layers, the nonlinearity is usually introduced by a sigmoidal function $f$ that bounds the layer's outputs to either 0 or 1, see Figure 2.6. The use of the sigmoidal function is convenient because it combines the linear and hard thresholds applications, equation (2.8). At the output layer, the linear activation function is usually used to allow the network to produce values outside the range of 1 and -1.

$$f(x) = {}^{1}/_{1 + e^{-(w^T x)}} \qquad (2.8)$$

where

$f(x)$ is the log-sigmid function,

$w^T x$ is the output of the neuron,

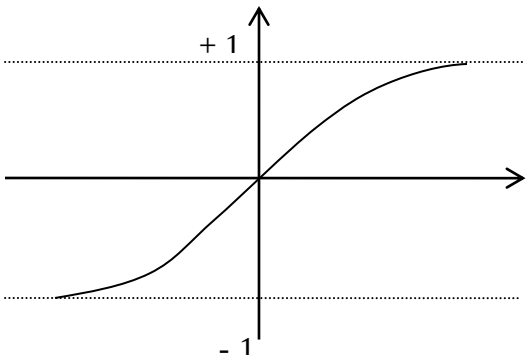


Figure 2.6: Sigmodial function

At each node, input weights from other nodes are summed and substituted to an activation function $f$ that transfers the output to the next layer.

$$o = f(\sum_{i=1}^{n} w_i x_i + b) \quad (2.9)$$

where $b$ is the bias that is used to adjust the output of the neuron. Its value is usually 1, and it is treated like an external weight to the network.

***NN training***

NN as a learning algorithm uses the training set to choose appropriate weights. The relationship between input and output of the network is represented by hypothesis $h$

$$h_w(x) = \sum_{i=0}^{n} w_i x_i \quad (2.10)$$

where

$h_w(x)$ is the network prediction,
$w$ is the weight or the parameters of the network,
$n$ is the number of features in the training set,
$x$ is the NN input.

In its general form, $h$ can be represented as:

$$h_w(x) = w^T x \quad (2.11)$$

where $h_w$ is a function of all weights of the network.

For the NN to choose the right set of weights that represents an accurate output prediction of a new input, the quadratic least square function is minimized.

$$J(w) = \frac{1}{2}\sum_{i=1}^{n}\left(h_w(x^i) - y^i\right)^2 \quad (2.12)$$

where $J(w)$ is the cost function and $y^i$ is the network target. The use of $1/2$ is only to simplify the calculation of the cost function where after differentiation it is cancelled.

The optimization algorithm that is usually used to minimize $J(w)$ is the gradient descent where a step by step optimization is implemented in the direction of the decay.

$$w_i := w_i - \alpha \frac{\partial}{\partial w_i} J(w) \qquad (2.13)$$

where $\alpha$ is the learning rate that illustrates the steps towered updating $J(w)$

Solving the gradient for one variable by applying the chain rule derivative:

$$\frac{\partial}{\partial w_i} J(w) = (h_w(x) - y) \frac{\partial}{\partial w_i} (h_w(x) - y) \qquad (2.14)$$

Taking the derivative of $i$ element at a time results in:

$$\frac{\partial}{\partial w_i} J(w) = (h_w(x) - y) x_i \qquad (2.15)$$

The updated weight is then:

$$w_i := w_i - \alpha (h_w(x) - y) x_i \qquad (2.16)$$

Gradient descent algorithm is usually implemented by the back-propagation (BP) method where weights are updated from output layer backwards. To reduce computational time, NN usually updates weights after summing the gradient of all training data $m$ to the network in what is known batch training.

$$w_i := w_i - \alpha \sum_{j=1}^{m} \left(h_w\left(x^j\right) - y^j\right) x_i^j \qquad (2.17)$$

The feedforward BP neural network training works in two directions, forward and backward. In the forward direction, the network starts by randomly initiating weights

with small values. Using those weights, it predicts the network output, $h_w(x)$. Then the error between targets and the predictions is calculated, $J(w)$. In the backward direction, the gradient of the least square error is calculated, equation (2.15). Then weights are updated, equation (2.17). The network continues in the forward and backward directions till the error between the network targets and predictions is below the preset threshold. Each update in weights is called an epoch. When the network is successfully trained with a sufficient data set it becomes ready to predict outputs from new data that was not in the training set.

The successful training of the network is highly dependent on the proper selection of number of training data, features, hidden layers and neurons. If the number of training data is too small, the network will be more prone to underfitting, where the solution cannot be generalized to new set of data. If the number of training data is huge, the network will be more prone to overfitting where the solution is too rigid to generalize from a new set of data. One possible criteria to check if the data is enough for generalization is to divide it into three sets: training, validation and testing. The training set is usually the biggest while the validation set is used to stop the training before overfitting, and the testing set tests the network generalization. However, if the data is scarce, it is preferred to use all of the data for training only.

### 2.3.2. Fuzzy logic

In a fuzzy logic system, human knowledge is represented by *If-then* rules in which an input-output relationship is linguistically represented and characterized by continuous membership functions. Applying those membership functions, the crisp measurement is fuzzified for a value between 0 and 1. Then inference mechanism finds the match between the fuzzy value *u(x)* and its corresponding rule. Once the compositional rule is applied, the control action is defuzzified to a crisp value *u(y)*, see Figure 2.7.

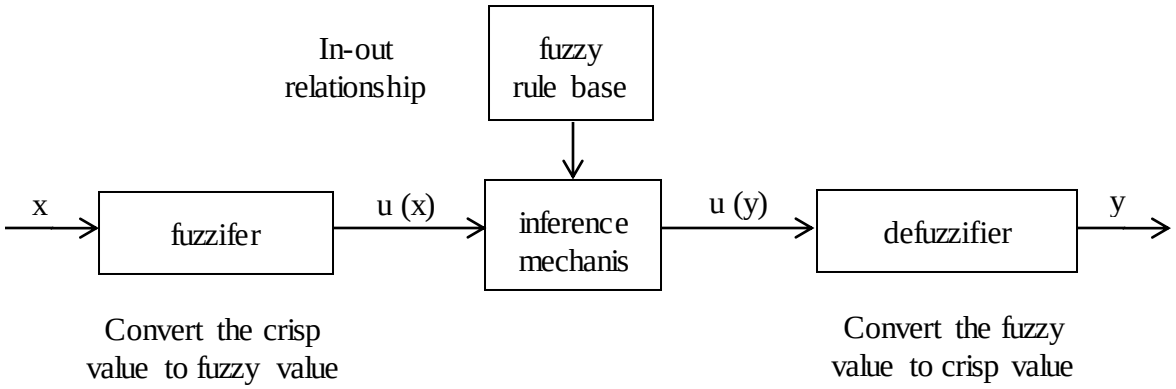


Figure 2.7: Schematic of fuzzy logic system

Similar to the NN, FL is often used when the exact mathematical model is too complex. However, the ability of FL to represent the inexactness in the system widened its applications in the literature, where the crisp value is represented by a fuzzy degree $\mu_x(x)$ in the interval [0 - 1]. $\mu_x(x)$ reflects the belonging of the crisp value to the fuzzy set $X$. The fuzzy set can be represented graphically by the means of membership functions. A membership function of either zero or one respectively means that the corresponding element does not belong or is definitely an element of the set. A membership function in between 0 and 1 corresponds to non-crisp element that fall in the fuzzy boundary of the set, see Figure 2.8.

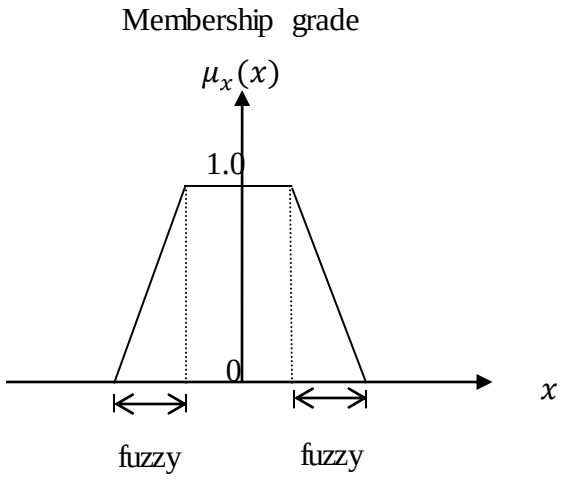


Figure 2.8: The membership function of a fuzzy set

The inference mechanism describes the fuzzy logic reasoning in the form of *if-then* rules where the premise and consequent are illustrated respectively. The premise part represents the fuzzy set X of the input x and the consequent part represents the fuzzy set Y of the output y, equation (2.18). Both parts are antecedent linguistically; i.e. has been partitioned by the use of membership function. Several input variables might be connected by AND operation. For instance, if A and B are two fuzzy sets that belong to X, their fuzzy rule can be in the form:

$$R: IF\ x\ is\ X\ THEN\ y\ is\ Y \qquad (2.18)$$

This rule represents the Mamadani approach, where its output has to be defuzzified for the use of practical tasks. The Mamadani approach is useful for the knowledge representation where the consequent is represented linguistically. If the output of the rule needed to be a crisp value, the Sugeno or TSK model can be used:

$$R: IF\ x\ is\ A\ AND\ IF\ b\ is\ B\ THEN\ y = f(x, b) \qquad (2.19)$$

Logical AND operation represents the fuzzy-set intersection, where the smallest of the two membership grades governs the outcome. The resulting membership function is governed by the minimum function:

$$\mu_{A\cap B}(x) = \mu_Y(y) = min\ \left[\mu_A(x), \mu_B(x)\right] \quad \forall_x \in X \qquad (2.20)$$

After executing the rule base, the overall membership function for the complete rule base is obtained using OR operation. In this operation, the larger of the two membership grades is selected using the maximum function:

$$\mu_{A\cup B}(x) = max\left[\mu_A(x), \mu_B(x)\right] \quad \forall_x \in X \qquad (2.21)$$

For n number of rules in the fuzzy rule base system, the overall resulting membership function for the complete rule base is:

$$R_1 \cup \ldots \cup R_n: \mu_R(y) = max\left[\mu_{Y_1}(y), \ldots, \mu_{Y_n}(y)\right] \quad (2.22)$$

The defuzzification of $\mu_R(y)$ can be done by several methods, such as centroid, mean of maxima, etc. The centroid method calculates the center of gravity of the overall membership function:

$$y = \frac{\sum_{i=1}^{m} area_i m_i}{\sum_{i=1}^{m} area_i} \quad (2.23)$$

In this section we introduced the theory behind PEM fuel cells and the tools used in this research. We explained the electrochemical background of PEMFCs. Then we gave an overview of the EIS method and its application as a diagnostic tool. Finally, we discussed the neural network and fuzzy logic theories.

# Chapter 3. Experiment Implementation of EIS

In this chapter we tested the ability of voltage and impedance in detecting hydrogen leak for a single cell and a multi-cell stack. Aiming to understand the behavior of the stack at increased leak rates, we analyzed the signals at reduced oxygen concentrations. For a single cell, our analysis was limited due to the collapse of the cell voltage at large leak rate and/or low oxygen concentration. Using a multi-cell stack, we were able to further increase leak rates and decrease concentrations without collapsing the voltage. This allowed us to understand the stack behavior at air starvation. The measurements of the signals at various amounts of leak rates and stack sizes allowed us to identify the signal that is able to detect the leak with high resolution.

## 3.1. Experimental setup

The full-size FCvelocity$^{TM}$-1100 fuel cells were tested at Ballard Power Systems at 20 and 50 A loads. Cells with small, medium and large hydrogen leaks were tested with a differential pressure (dP) of 2, 4, 6 and 8 psig (13.8, 27.6, 41.4 and 55.2 kPa) using air as oxidant. The normal and leaky cells were also tested with different oxygen concentrations; see Table 1 for the test plan details. The reduction in concentration was made by mixing oxygen with nitrogen at different rates, and the increase in hydrogen leak rate was made by controlling the dP between anode and cathode.

To separate the single contributions of the performance loss of the fuel cell during load, impedance measurements were conducted while changing only one variable at a time. All EIS tests were made at low currents; 20A and 50A to insure that hydrogen leak was not hindered by the increasing content of water resulting from higher ORR at higher loads. Running at low loads ensures an adequate hydration on the anode and cathode

where water diffuses between those two compartments. This ensured that cathodic overpotential was the main contribution to the impedance signature. At higher current densities, the anode tends to dry-out as a result of higher proton migration to the cathode carrying water molecules. This adds an anodic overpotential contribution to the impedance spectra.

Table 3.1: The test plan

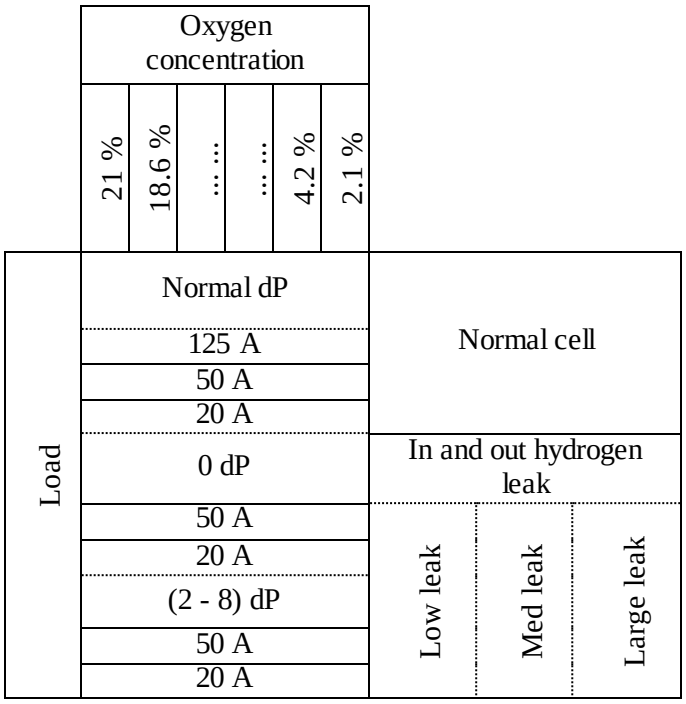


To allow a fair comparison between the impedance of leaky cells and the normal cell, hydrogen leakage across the leaky cells was minimized by keeping 0 dP across the holes. All measurements were conducted using the Kikusui EIS equipment in galvanostatic mode with a 10% AC amplitude over the frequency range 20k - 80m Hz. EIS measurements were conducted once the stack reached equilibrium for each operating condition tested. In order to avoid the change in current and voltage relationship during measurements, the total frequency sweeps of the impedance were conducted in the

shortest time possible, about 6 minutes. Thus the system can be assumed to be at steady-state conditions during the measurement. To avoid frequency interference, the power supply and loadbank (see Figure 3.1) were turned off while measuring the impedance.

The test bed used a TDI - Dynaload loadbank RBL488 400-600-4000 and Xantrex DC power supply XPR 10-600 connected in series to satisfy the voltage limitation of the loadbank. The Kikusui EIS equipment consisted of an FC impedance meter KFM2150 and three electronic loads, PLZ664WA. The loadbank and power supply were connected to the fuel cell and EIS machines in parallel. This configuration provided the required load by using either the EIS equipment or the test station loadbank between test periods. The power supply was used to overcome voltage limitations of the loadbank when higher voltage was needed for higher current testing.

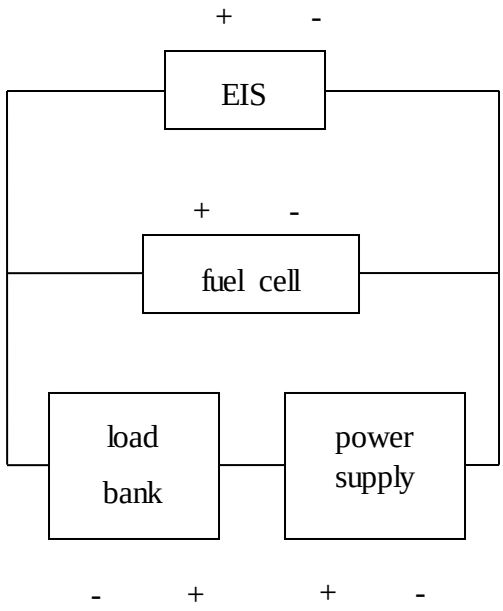


Figure 3.1: Schematic view of the test bed

Prior to testing, leak rates were evaluated at 0.5 bar air pressure across the MEA. The MEA was then placed in an open-faced fixture with 3 to 5 psi dP to identify the holes' location. Submerged in DI water, bubbles appear at the surface of the MEA revealing the location of the leaks. In testing, temperatures of the anode and cathode were

kept equivalent by providing similar coolant flows through the stack. The cell voltage was recorded between the terminals of the stack, which is shown in Figure 3.2.

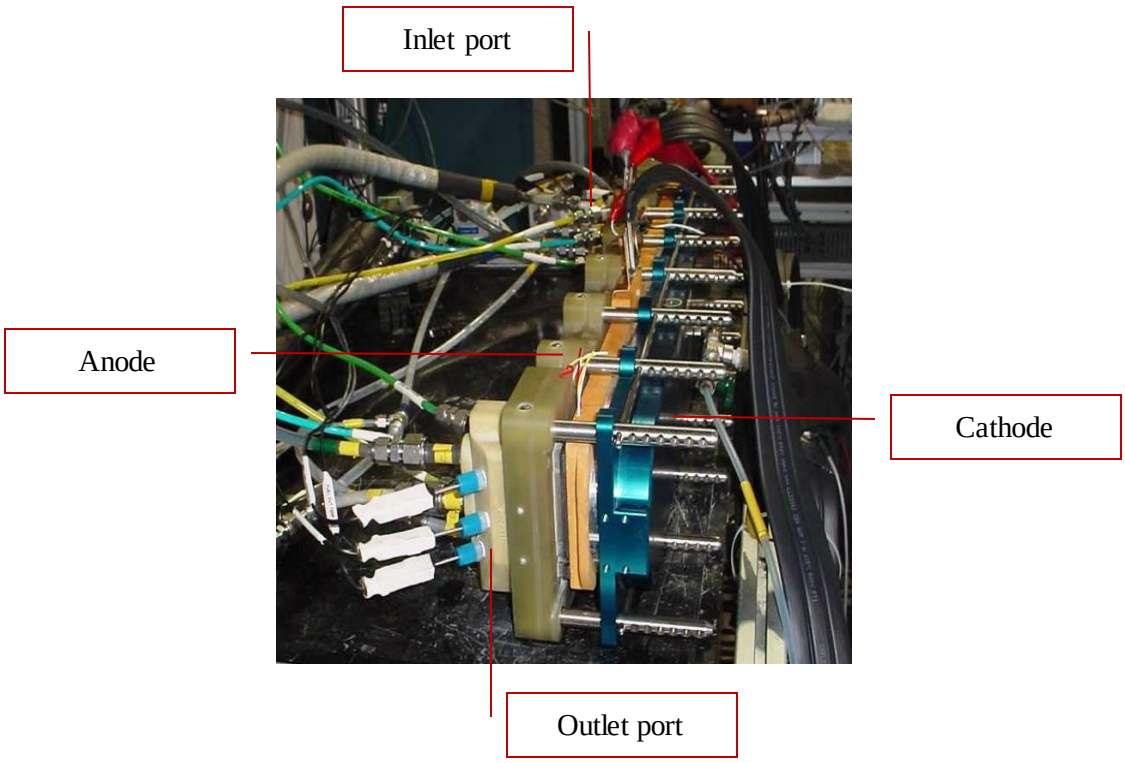


Figure 3.2: The single-cell fuel cell stack

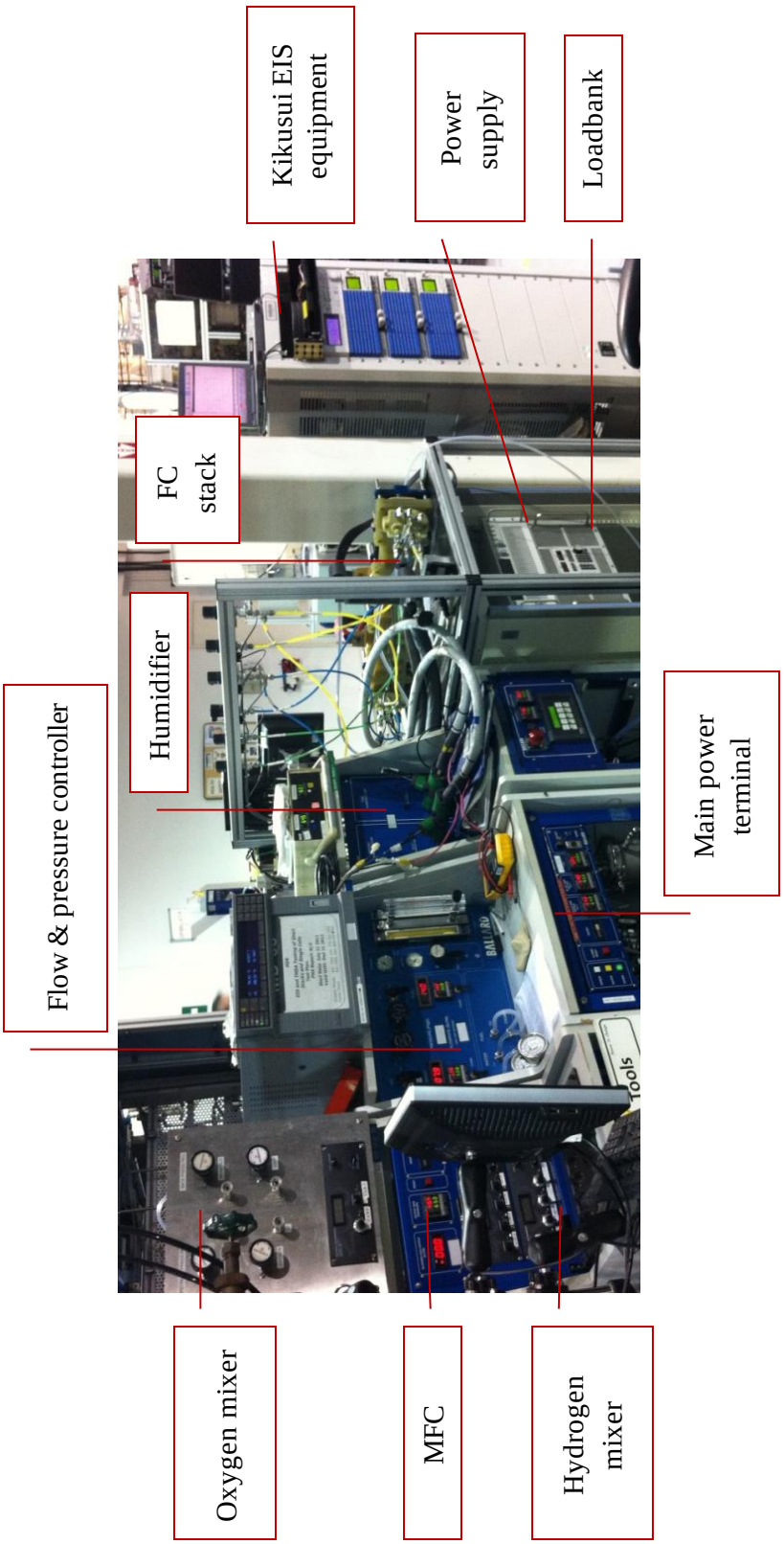


Figure 3.3: The test bed

The test bed controlled and monitored the stack temperature, fuel and air humidity, gas and coolant flow rates, pressures, and load current; see Figure 3.3. Two MFC's for oxidant and fuel were installed in the test bed to allow low and high flow rates. Gas mixers were used in this experiment to control the oxygen and hydrogen concentrations balanced with nitrogen. The use of mixers allowed the testing of various oxygen and hydrogen concentrations while maintaining constant flow rates, Table 2. Using constant flows made the EIS measurements more stable due to improved water management. Aiming to represent the signatures with their associated external leak rates, we installed a hydrogen sensor at the downstream of the stack.

Table 3.2: The fuel cell operating conditions

| Loads (A) | | 125 | 50 | 20 |
|---|---|---|---|---|
| Hydrogen parameters | Fuel stoich | 2.76 | 4.02 | 4.7 |
| | Fuel flow (SLPM) | 2.43 | 1.42 | 0.66 |
| | Fuel In Pressure (psig) | 13.63 | 9.86 | 8.27 |
| | Fuel Dew Point (°C) | 62.07 | 62.74 | 61.74 |
| | | | | |
| Oxygen parameters | Air stoich | 1.87 | 2.13 | 3.1 |
| | Ox flow (SLPM) | 3.89 | 1.78 | 1.03 |
| | Air In Pressure (psig) | 11.6 | 7.98 | 6.24 |
| | Air Dew Point (°C) | 60.83 | 61.29 | 60.2 |

## 3.2. Results and discussion

### 3.2.1. Impedance of a single cell

Four cells in total were used in this study; a normal working cell and three leaky cells. The leaky cells were selected from working bus modules with low, medium and

high crossover leak rates of approximately 50, 300 and 500 ccm, with air at 0.5 barg. All leak locations were determined to be at the inlet side of these fuel cells. Outlet port leak tests were conducted by switching the inlet and outlet ports of the stack. To approximate the operating conditions of the stack, 1 SLPM fuel flow at a 66% hydrogen concentration was used with a 20A load. The rest of the flow was nitrogen.

Similar to the studies done by [32], [33] and [53], we noticed a reduction in impedance with the increasing amounts of loads, see Figure 3.4. This is due to the activation loss described by Tafel, equation (2.6). However, the mass transport part of the impedance increased with the increasing of the load. This increase in the mass transfer at high currents is usually associated with improper water management due to higher ORR or insufficient reactant feeding.

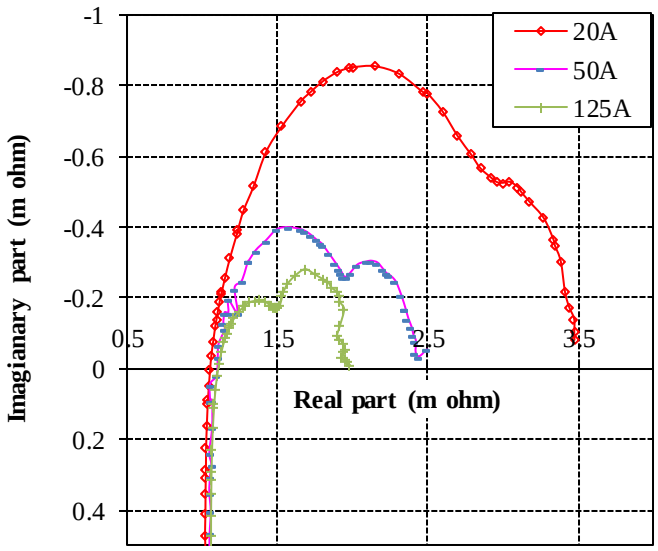


Figure 3.4: Impedance of a normal cell at 20, 50 and 125 A load

For a single cell, it was sufficient to represent the impedance spectra with the modified Randles equivalent circuit shown in Figure 3.5, utilizing resistive and capacitive elements to describe both kinetic and mass transport phenomenon. More specifically, $R_{mt}$ describes the oxygen diffusion resistance, while C has been used to describe the diffusion layer in the Pt/C agglomerate structure where oxygen is consumed at the Pt surface [22].

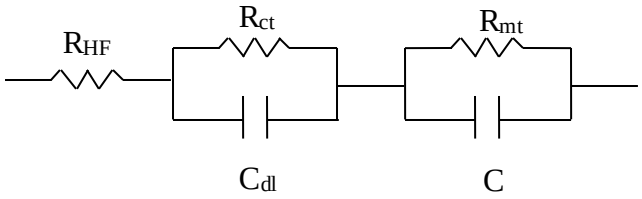


Figure 3.5: Equivalent fuel cell circuit for experimental fitting

### *Changing hole location*

Increasing leak rates at 50A increased $R_{mt}$ but did not affect $R_{ct}$ where the parasitic current is a smaller portion of the total current, see Figure 3.6. As expected, no change in the parameters were noticed with the increasing leak rates at the outlet port, except at high hydrogen leaks, where most of the fuel recombined with air throughout the stack length electrochemically. In all cases $C_{dl}$ changed in a small range. This reflects the intact property of the MEA material throughout the tests. The signatures of leak rates at the outlet of the stack barely changed at 20A. Thus their associated parameters were omitted.

The effect of hole location on the impedance agrees with our other studies – outside the scope of this work – that examined the recombination effectiveness of hydrogen transfer leaks in the upstream and downstream of the cathode on the performance of a stack. It was noticed that increasing the hydrogen concentration at the cathode inlet reduced the voltage of a cell gradually up to a limit where cell voltage became unstable and hydrogen appeared at the oxidant outlet. When the hole was placed at the cell air outlet, the cell didn't suffer much air starvation and most of the hydrogen leaked through the hole was measured at the oxidant outlet. One can hypothesize that the shorter the distance of the hole to the exhaust, the lesser the reaction of the transfer hydrogen leak with air inside the cell.

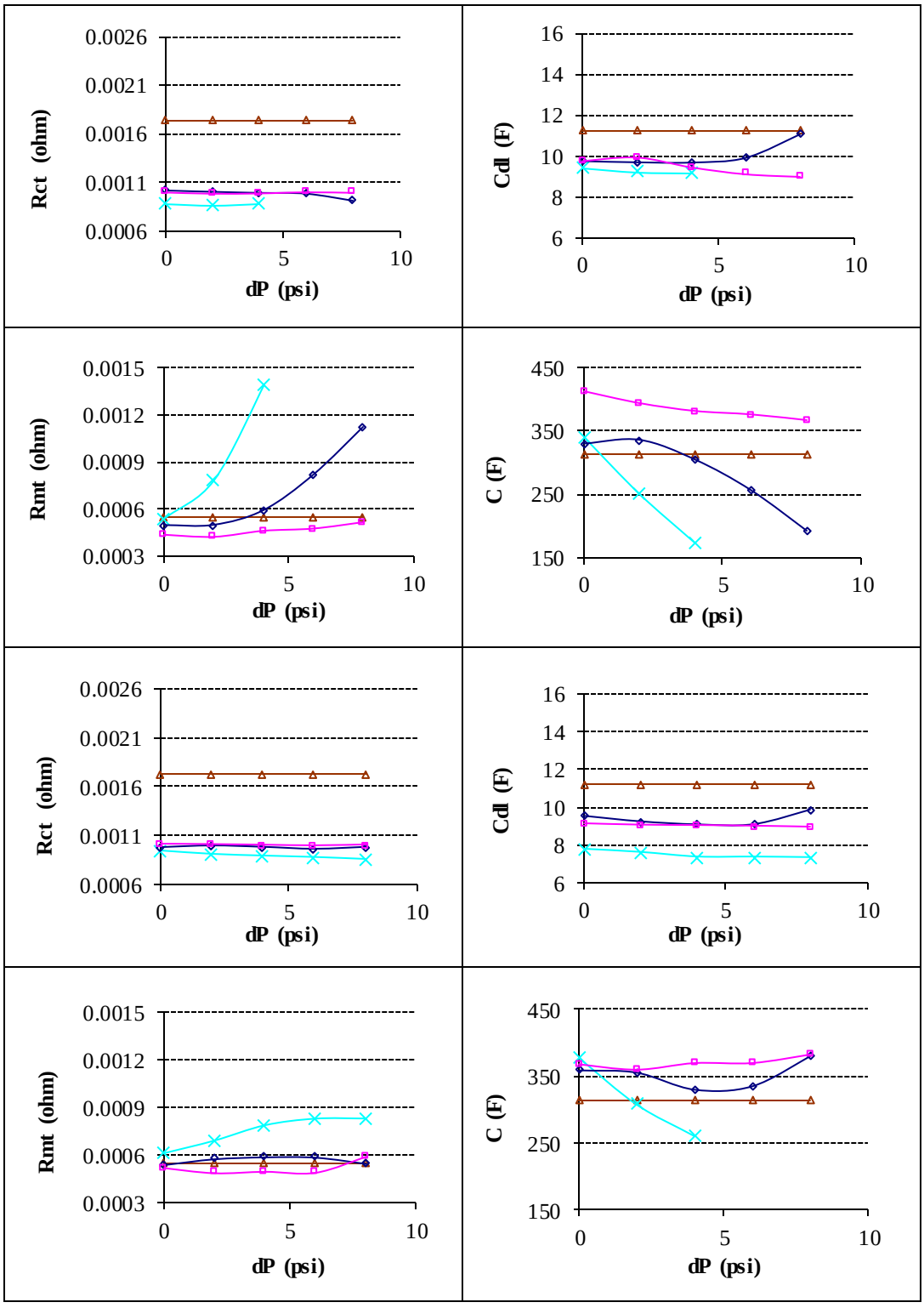


Figure 3.6: Effect of differential pressure on the parameters of the 50A load inlet (top) and outlet (bottom) ports.

Note: (Δ normal cell, □ small leaky cell, ◊ medium leaky cell, × large leaky cell)

### *Oxygen concentration and dP*

The effects of hydrogen dilution in impedance signatures were minimal, and major changes in the impedance with different hydrogen concentrations were not apparent. With lower amounts of oxygen concentrations, we found a steady increase in the impedance. This increase was mostly at the mass transport region, second arc. When oxygen concentration was reduced to an amount less than needed by the stack, air starvation occurred and the impedance increased significantly, as shown in Figure 3.7. At concentrations lower than 10% oxygen, the cell voltage was unstable and impedance could not be measured.

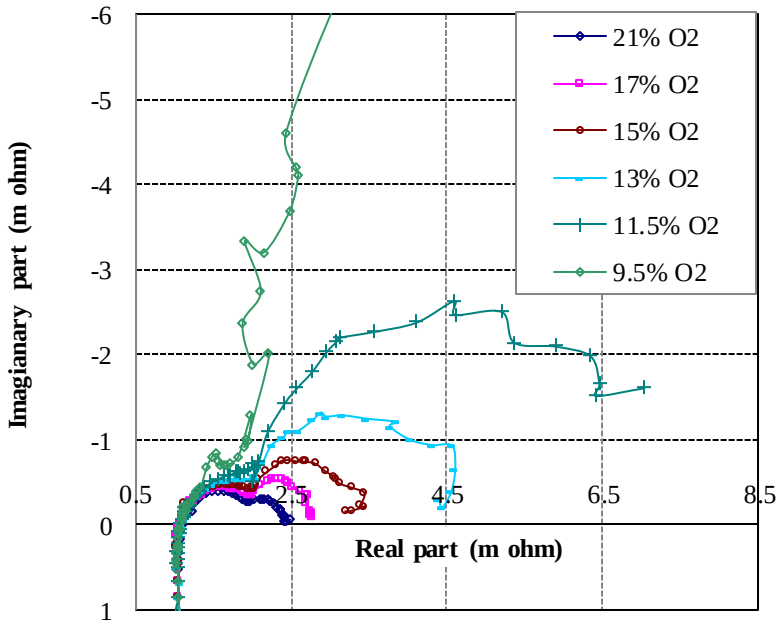


Figure 3.7: Impedance of a normal cell at 50 A load

Because the leaky cells used in the experiment were rejected from operating bus modules, their impedances were bigger than the impedance of the normal cell due to degradation, see Figure 3.8. For the sake of comparison, the impedance spectra were normalized by the high frequency resistance of 1.34 +/- 0.25 m ohm.

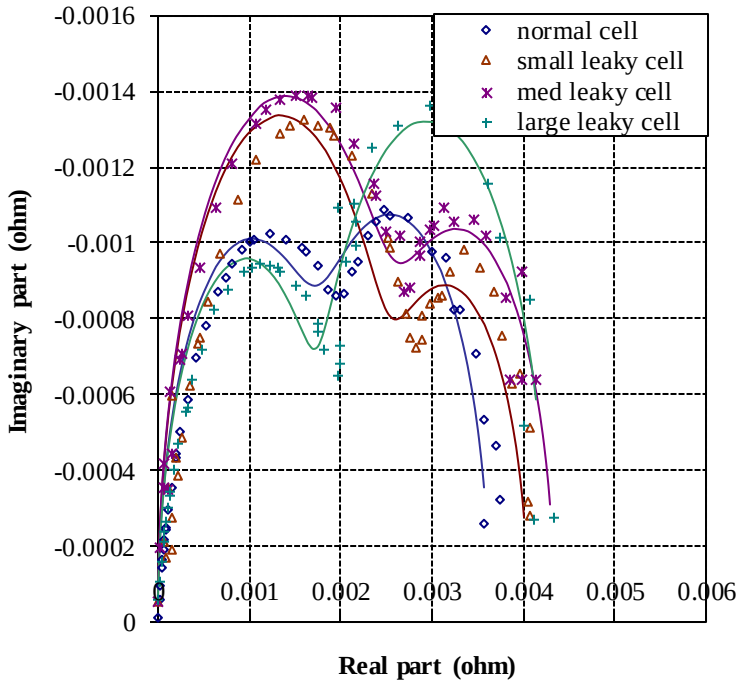


Figure 3.8: 20A impedance of the normal cell and leaky cells with inlet holes for 13% O2 concentration

In our study, leak rates were controlled by adjusting the anodic overpressure across the hole. The higher the dP, the greater the amount of hydrogen leaking through the MEA. When leaks occurred at 20A load, the charge transfer impedance, first arc, decreased and mass transfer impedance, second arc, increased, see Figure 3.9. The reduction of the charge transfer impedance is similar to the reduction of impedance at high load currents, and the increase of impedance mass transfer is similar to the increase of impedance at low oxygen concentrations. This similarity in impedance drives us to the conclusion that, at high dP, there is a greater internal parasitic current due to greater hydrogen crossover that affects the kinetics. The greater current generated by the catalyst (loadbank and parasitic) drives the charge transfer arc down due to the logarithmic Tafel relationship between voltage and current described earlier. Further when the reaction of hydrogen leakage increases at the cathode, the second arc increases due to the limitation in oxygen mass transport. When leaks occurred at 50A load, the first arc impedance did not change while the second arc increased, Figure 3.10. This was due to the increase in ORR resulting from running the stack at higher load.

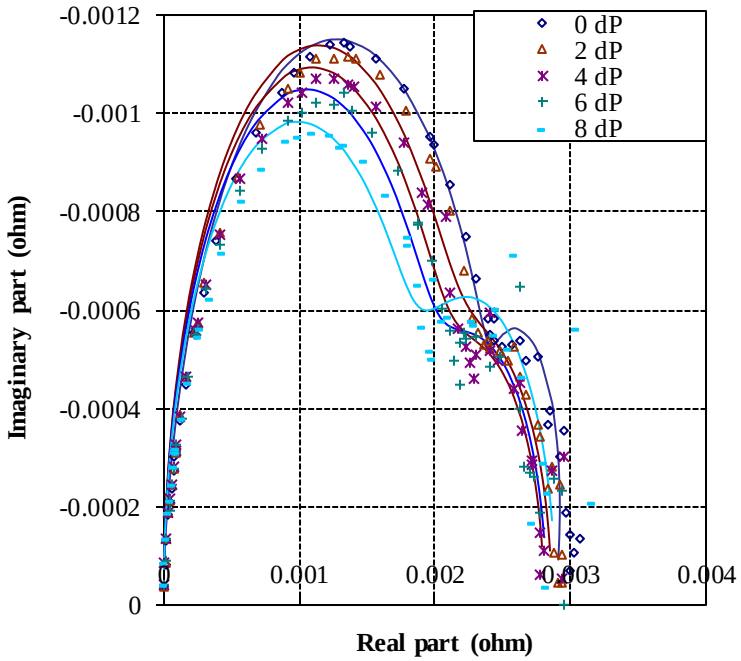


Figure 3.9: 20A impedance of the medium leaky with holes located at the inlet at different dP

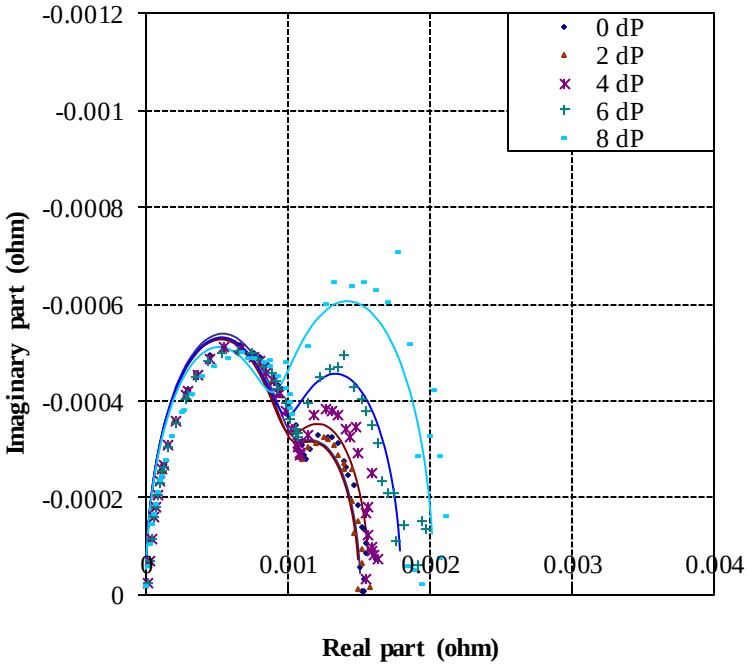


Figure 3.10: 50A impedance of the medium leaky with holes located at the inlet at different dP

As shown in Figures 3.11, the change in parameters at 20A for oxygen concentration and dP are somewhat related. The leaky cells had lower $C_{dl}$ compared to the normal cell, signifying catalyst degradation. The change in $R_{mt}$ with the change in oxygen concentration and dP was minimal. Similarly $R_{mt}$ increased and C decreased due to oxygen mass transport limitations The change in C and $R_{mt}$ with oxygen concentration agreed with the findings by Kawaji *et al.* [24], and show a significant sensitivity to the oxygen concentration as expected. At lower oxygen concentration, Rct increased while it decreased with the increasing of leak rates across the MEA due to parasitic current. One can deduce that oxygen concentration and dP have similar behavior in the mass transport region while they are differ in the charge transfer region.

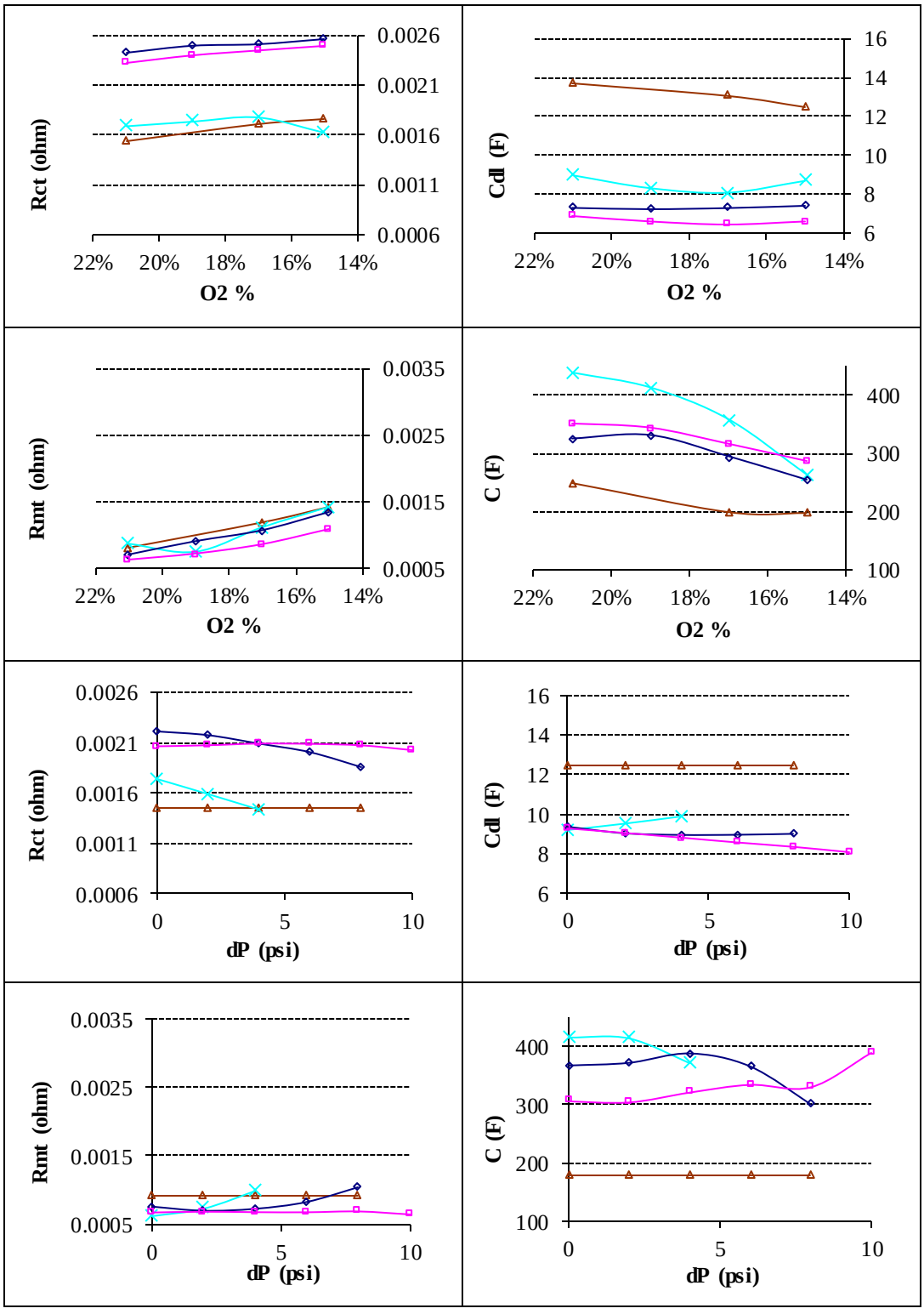


Figure 3.11: Effect of oxygen concentration (top) and dP (bottom) on the parameters of the 20A load,

Note: (Δ normal cell, □ small leaky cell, ◊ medium leaky cell, × large leaky cell)

### 3.2.2. Impedance of multi-cell in a stack

Two sets of data were obtained in our study with stack sizes of 5, 9 and 19-cell. The first set of data was measured at reduced oxygen concentration rates on the cathode side while keeping the dP across the membrane at the inlet of the stack at 0 psi. The second set of data were measured at increased dP between the anode and cathode while keeping oxygen concentration in air at normal level; i.e. 21%. The two impedance data sets were interrelated by the recombination of oxygen with the leaking hydrogen through the pinholes. However, oxygen concentration impedance was obtained by an equal reduction of oxygen in all cells whereas the dP impedance was obtained by the reduction of oxygen at only the leaky cell in the n-cells stack.

Using the same experimental setup for a single cell, we investigated the effect of hydrogen leak rate in a stack of various sizes and leak rates. Experiments were conducted for a stack with small, medium and large leak rates at the inlet side of the leaky cell. The leaky cell was placed in the middle of normal cells. To be consistent with the single cell measurements, we measured the impedance at the same operating conditions of a single cell. However, in the multi-cell tests, reactant and oxidant flow rates were proportional to the number of cells in the stack. Oxygen concentration was reduced gradually by controlling the mixture of nitrogen and oxygen at the cathode side. The oxidant flow rate was kept constant to isolate and minimize the effect of water accumulation on the impedance signatures.

#### *Air starvation*

A direct correlation between oxygen concentrations and impedance signatures was noticed. With the increasing of oxygen concentrations, impedance signatures increased. This increase continued with the reduction of concentration until the impedance shrank to values less than the signature at normal operating conditions, see Figure 3.12. The behavior of the impedance signatures can be explained by calculating the air stoich, that is the ratio of provided to consumed air. Using the equation in [54]:

$$stoich = \sum_1^N (flow * N * O_2\%) \Big/ \sum_1^N (C_{air} * N * I * 0.21) \qquad (3.1)$$

where

*flow* is air flow of 20 and 50 A loads; 1.03 and 1.78 SLPM respectively.

*N* is the number of cells in the stack

$O_2\%$ is the percentage of oxygen concentration at the cathode side

$C_{air}$ is air consumption, 0.0167 [SLPM/A/cell]

*I* is the load [A]

As concentration decreases, air stoich decreases and impedance increases due to the lack of oxygen in the cathode side. At low stoich, the stack lacks enough oxygen that is needed for electrochemical reaction. As a result, the impedance increases significantly and a sharp voltage reduction was noticed. For an air stoich less than 1, the impedance reduced to very small values due to air starvation, where the stack voltage also dropped to almost zero, Figure 3.13.

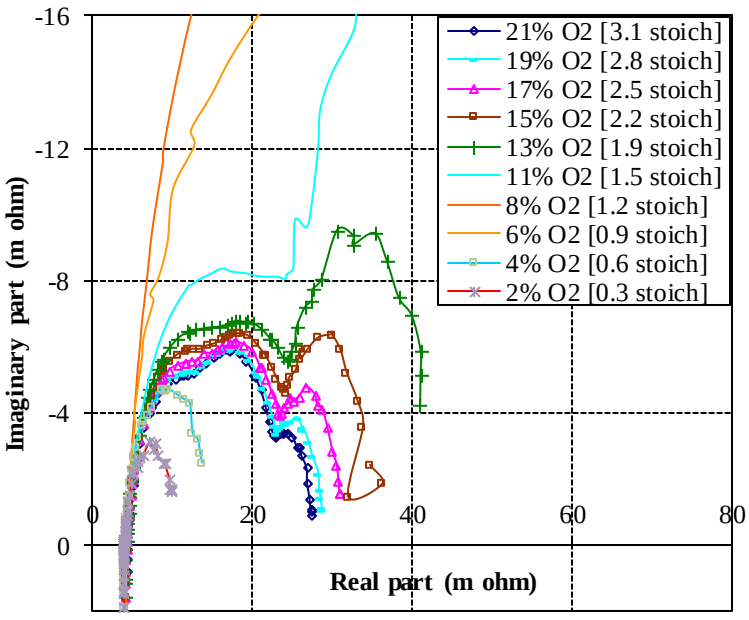


Figure 3.12: 20A impedance of a 9-cell normal stack at different oxygen concentration

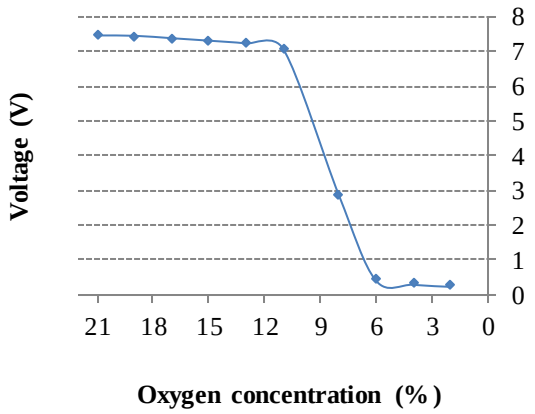


Figure 3.13: 20A voltage of a 9-cell normal stack at different oxygen concentration

A similar impedance pattern was noticed with increasing dP, see Figure 3.14. First, the impedance increased due to the decreasing of air stoich resulting from recombination of oxygen with hydrogen at the leaky cell. With further increasing of leak rates, the leaky cell suffered air starvation and its voltage dropped to zero, Figure 3.15. As a result, the impedance started decreasing until it reached saturation at high leak rates where the leaky cell was not contributing to the overall stack impedance. Thus, no significant reduction in impedance was noticed with further increasing of leak rates. At the highest leak rate, no external hydrogen was noticed. As a result, we concluded that the hydrogen crossing over was typically totally recombined with oxygen throughout the MEA length. This recombination produced extra water that might also have self-sealed or partially self-sealed the pinholes.

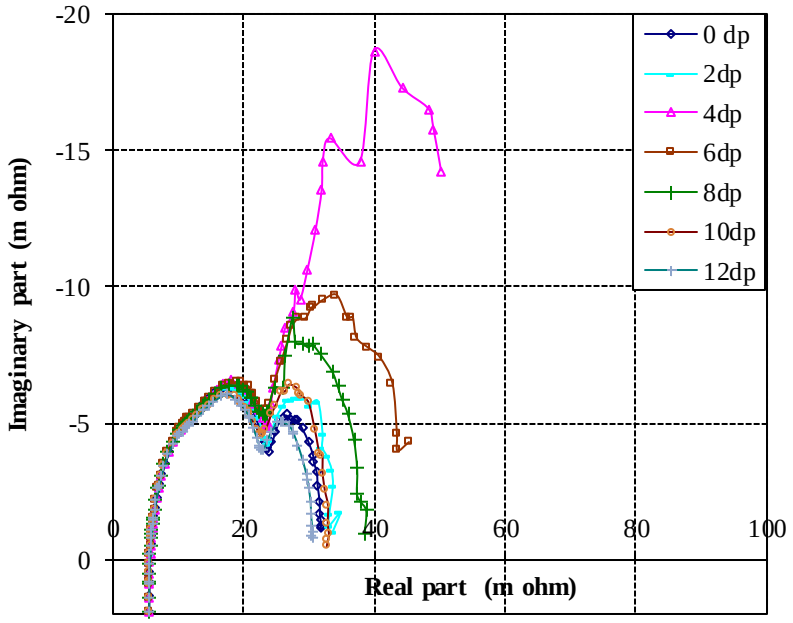


Figure 3.14: 50A impedance of 19-cell short stack with large leaky cell at different dP

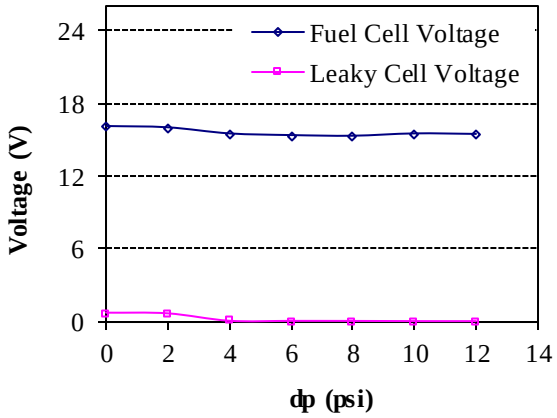


Figure 3.15: 50A voltage of 19-cell short stack with large leaky cell at different dP

To check its percentage in the air exhaust, two hydrogen sensors were installed at the stack outlet; Neodym and RKI sensors respectively, see Figure 3.16. The Neodym sensor is placed immediately after the oxidant outlet and its reading range is 0 - 100 % hydrogen. It is outfitted with trace heating in order to prevent water condensation in the oxidant outlet from interfering with the measurement. As a safety precaution, an air dilution line of known flow is used to keep the ventilated oxidant output below 4%

hydrogen. We insure the safe ventilation of hydrogen by using an RKI sensor that is calibrated between 0.5 - 4.5 V corresponding to 0 - 4 % hydrogen. The dilution flow is adjusted based on the reading of the RKI sensor.

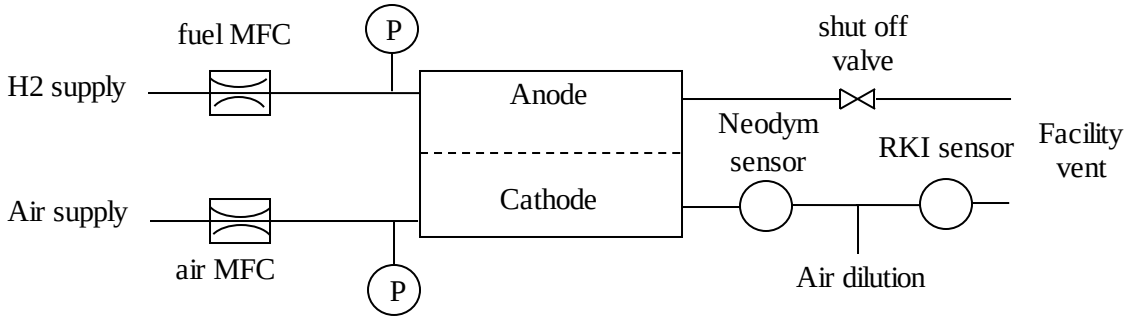


Figure 3.16: A schematic diagram of experimental setup

External hydrogen leak was noticed while air starving the stack. At very low oxygen concentrations, a considerable amount of hydrogen was measured at the stack outlet, see Figure 3.17. Hydrogen pumping effect was noticed with oxygen concentrations less than 6%. At 2% concentration, the cathode outlet contains about 10% hydrogen. Obviously, these increasing amounts of hydrogen could put the stack at risk and should be taken into consideration while designing the diagnostic system. Besides monitoring the external hydrogen leak, the change in impedance signatures could be used to show the intensity of the leak. Decreasing the concentrations, the charge transfer part of the signature diminished and the mass transfer part increased due to the increasing resistance of the oxygen loss.

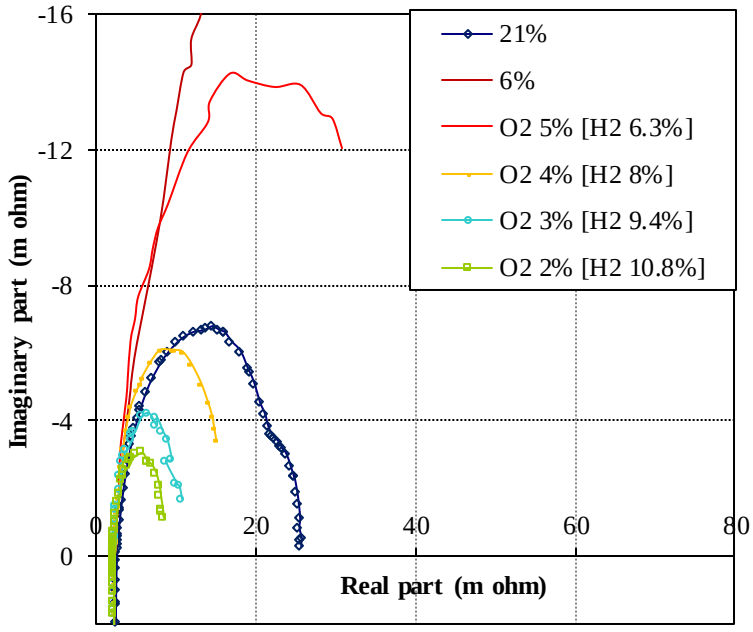


Figure 3.17: 20A impedance and hydrogen at the outlet of a 9-cell stack with a medium leak cell

### *Oxygen concentration and dP*

When the impedance of a single leaky cell was measured, the pattern of the impedance signatures changed with the reduction amounts of oxygen in the cathode. However, the change in impedance of a stack with the reduction of oxygen was only noticed in the mass transport region. Thus, an equivalent circuit that fits the complete impedance signature was unfeasible. Instead we used a simple Randles circuit to fit the mass transport region, see Figure 3.18. Initially with the signatures at low oxygen consumption, the fitting was matching the impedance data. At higher consumption; namely low concentration and high dP, the fitting was affected due to the flatness of the signatures. The impedance got flatter due to the lack of oxygen in the cathode as a result of low concentration and high leak rate respectively, see Figure 3.19.

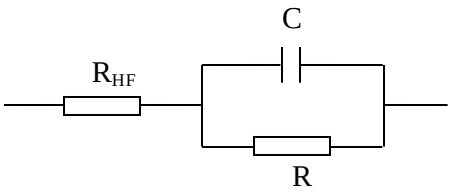


Figure 3.18: Randles model

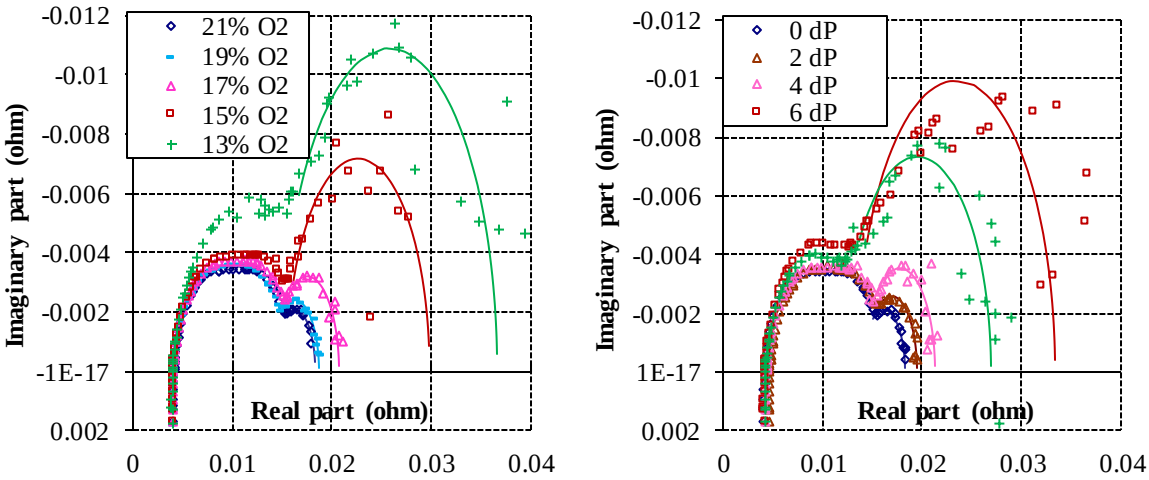


Figure 3.19: 20A impedance of a large leaky cell with 5-cell stack at different oxygen concentration (left) and dP (right)

By analyzing the parameters of the Randles circuit we noticed similarities between the impedance behavior of the oxygen concentration and dP, see Figure 3.20. In the case of decreased concentrations, the mass transfer resistance increased due to the lesser amount of oxygen in the cathode. This increase was high with the higher load. The steady decrease of C resulted from the continuous increase of impedance with decreasing oxygen concentrations. In the case of increasing dP, R initially increased due to the recombination effect. With higher recombination, the leaky cell was air starved and the resistance started declining. However, the behavior of C was similar to the oxygen concentration capacitance. In contrast to the resistance, no significant change was noticed in the capacitance with the change of the loads.

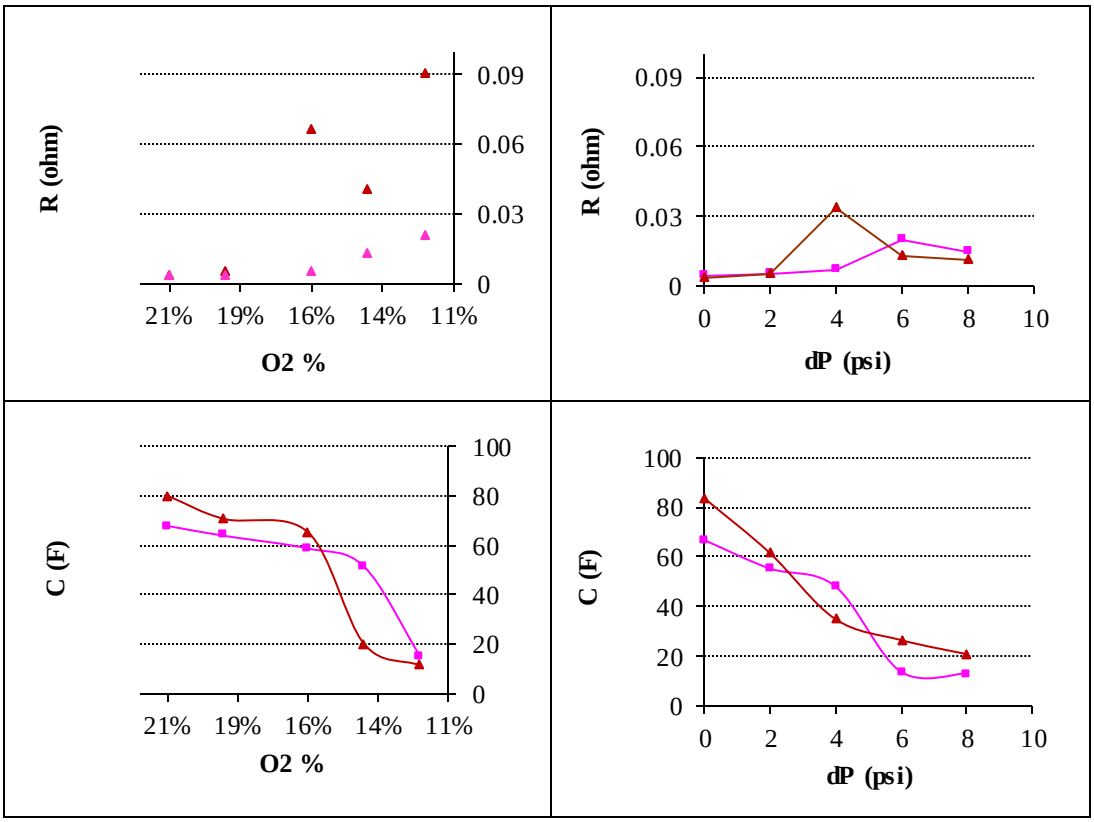


Figure 3.20: The parameters of 20A 5-cell stack of oxygen concentration (left) and dP (right).
Note: (■ 20A, ▲ 50A)

Similar to the single cell, impedance signatures were observed to increase with decreasing amounts of oxygen concentration. This pattern was consistent with the decreased amount of oxygen at different stack sizes. However, when the amount of oxygen was insufficient to deliver enough power to the stack, the impedance increased sharply, see Figure 3.21.

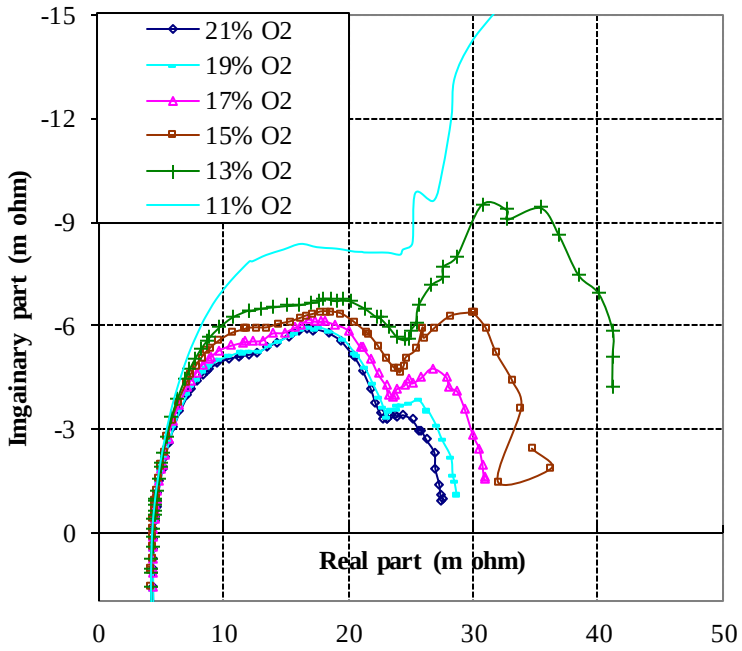


Figure 3.21: Oxygen concentration impedance signatures at 20A load of a 9-cell stack

Similar behavior was noticed with increasing dP across the MEAs, where impedance signatures increased due to the recombination of oxygen at the cathode due to increased leak. However, with an increasing amount of leak, the impedance signature then reduced; see Figure 3.22 (a). This reduction in impedance was due to the loss of power of the leaky cell in the stack. In other words, the leaky cell was not contributing to the stack impedance at high dPs. With further increase in leak rates, the impedance was saturated and no reduction in the signatures were noticed. With the increase of stack size, the significance of signatures reduced, see Figure 3.22 (b). The change in impedance signatures were insignificant with the smaller leak rate, see Figure 3.23. Similar impedance behavior was also noticed at higher loads.

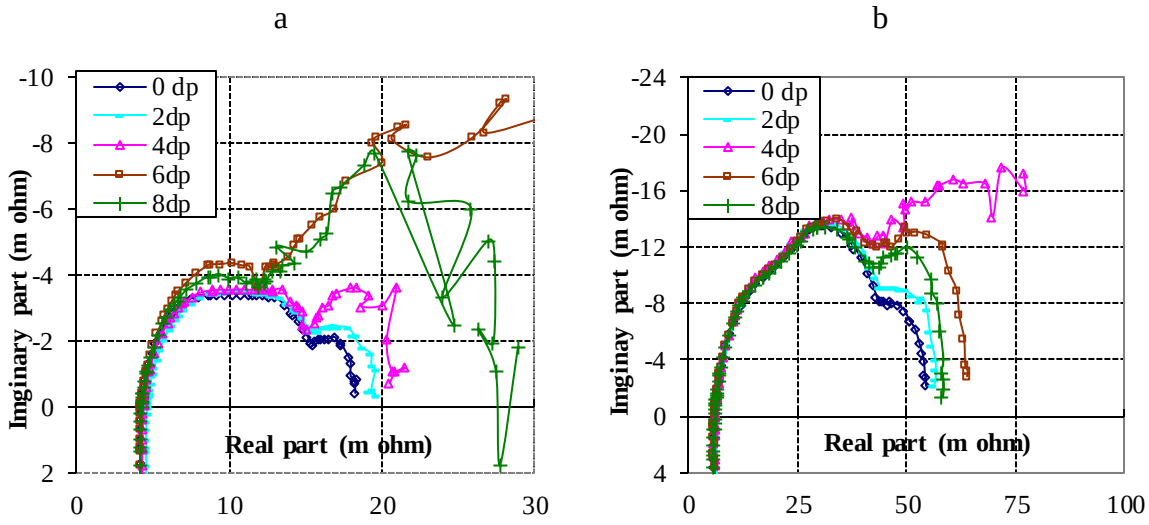


Figure 3.22: dP Impedance at 20A load of a 5-cell stack (a) and 19-cell stack (b) with a large leaky cell

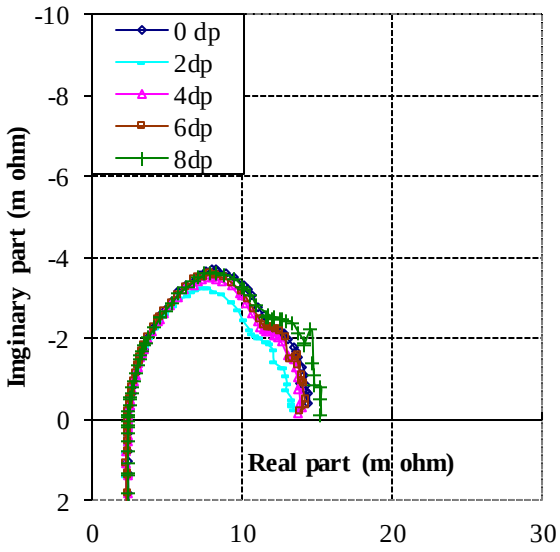


Figure 3.23: dP Impedance at 20A load of a 5-cell stack with medium leaky cell

The significance of impedance signatures were proportional to the number of cells in the stack and the amount of leak rates. The larger the stack size and the lower the amount of leak rate, the less significant the impedance signatures were. Increasing the stack size, no difference in the change in the impedance pattern of oxygen concentration comparing to smaller stack size was noticed, however, the change in the dP pattern was small, see Figure 3.24. This can be seen in the R and C parameters of the 19-cell stack,

see Figure 3.25. An important phenomena can be noticed in the separation between the capacitance parameters of the two loads with reducing the amount of leak rate for the same stack size. The lower the leak rate, the larger the gap between C of the 2 loads, see Figures 3.26 and 3.27.

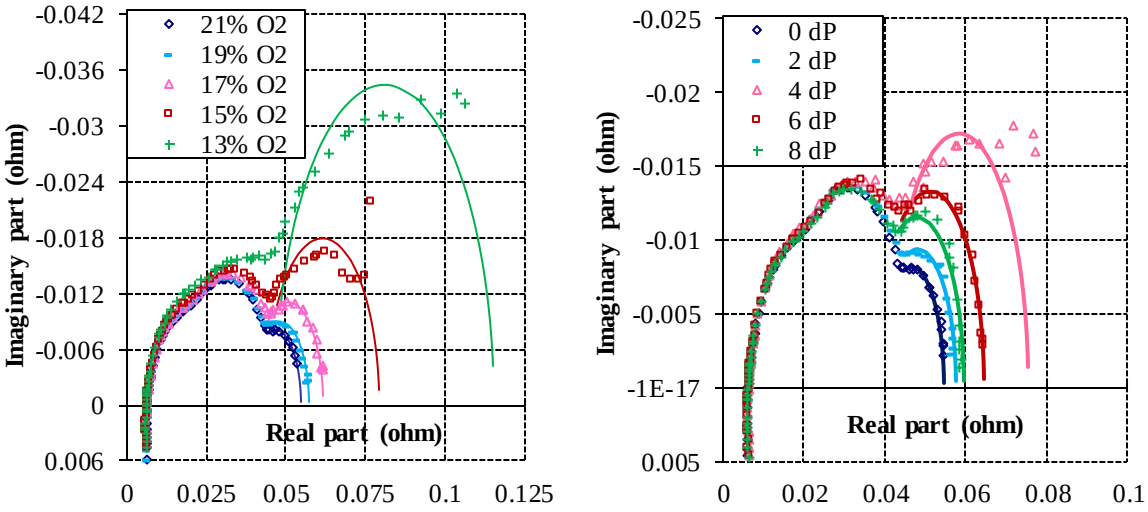


Figure 3.24: 20A impedance of a large leaky cell with 19-cell stack at different oxygen concentration (left) and dP (right)

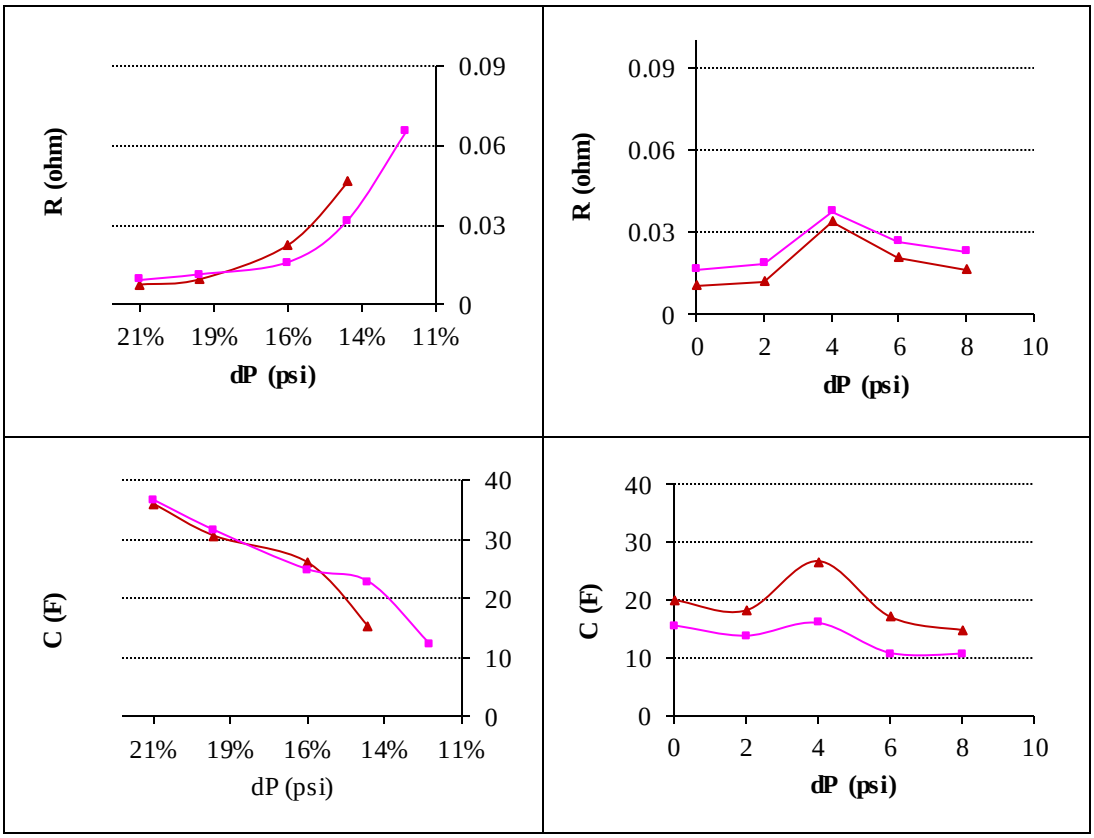


Figure 3.25: The parameters of 20A large leaky cell with 19-cell stack of oxygen concentration (left) and dP (right).
Note: (■ 20A, ▲ 50A)

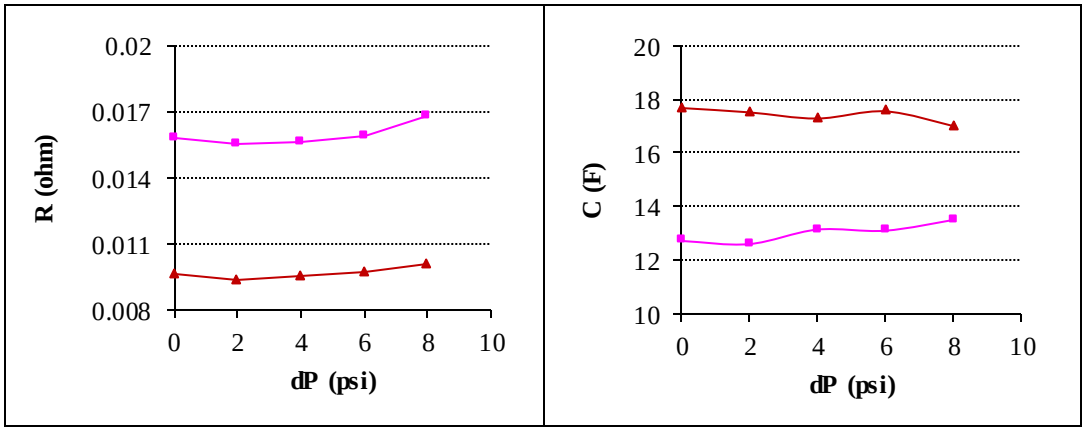


Figure 3.26: Effect of differential pressure on the parameters of 19-cell stack with medium leak MEA.
Note: (■ 20A, ▲ 50A)

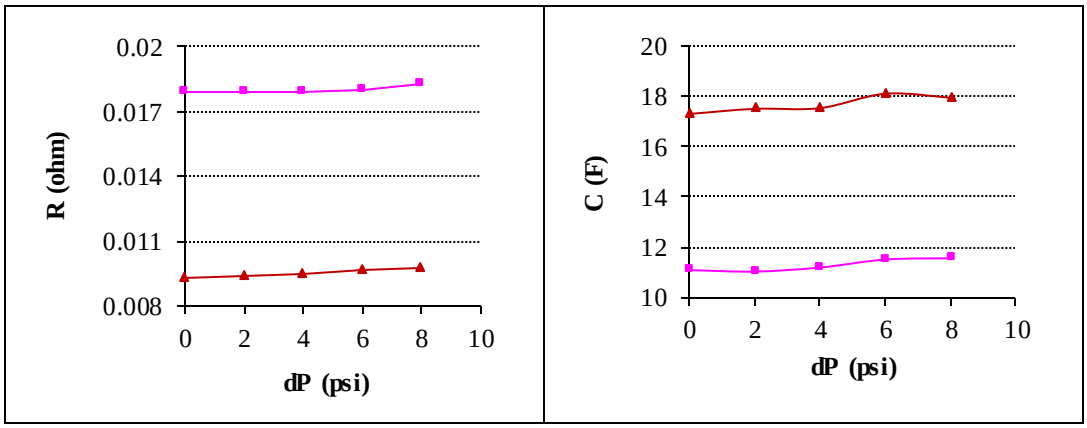


Figure 3.27: Effect of differential pressure on the parameters of 19-cell stack with small leak MEA.
Note: (■ 20A, ▲ 50A)

### *Measured leak rate*

To check with the NN estimation in the later chapter, we measured the impedance of known amounts of hydrogen directly injected into the cathode side of a cell. The hydrogen was injected by adding hydrogen injection MFCs to the experimental setup, as shown schematically in Figure 3.28. While only one hydrogen injection MFC is shown in the Figure, two injection MFCs were actually used in the experiment, one with a maximum range of 200 cm3 $min^{-1}$ (ccm), and another with a maximum range of 2000 ccm respectively. To minimize the leak through the pin holes, we initially kept pressure across the MEA anode and cathode inlet at 0 psi. Impedances were measured at 20 and 50 A loads.

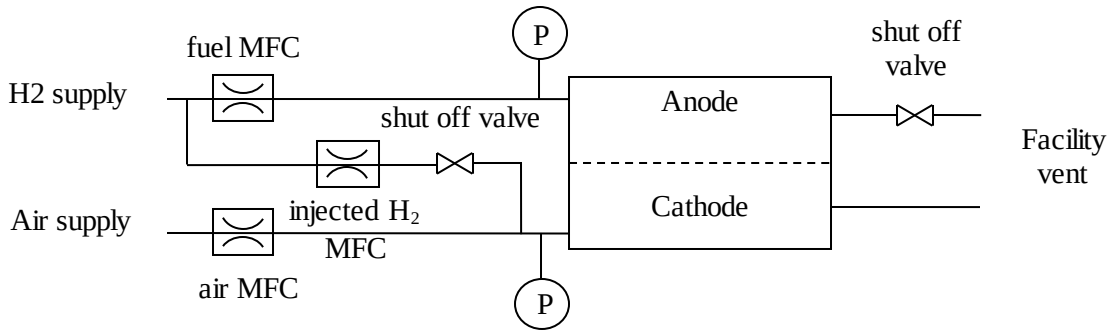


Figure 3.28: A schematic diagram of experimental setup

While keeping dP across the medium leaky fuel cell at 0 psi, we injected hydrogen at the cathode side during operation. Impedance of the injected hydrogen at 0 dP were compared with the impedance of the same cell with no injection at higher dP levels. Comparing the matching impedance, we were able to experimentally quantify the amount of hydrogen leaked through the MEA, see Figure 3.29. The solid lines used to fit data of matched impedance signatures. Impedance signatures at 8 dP was distorted due to the insufficient voltage produced by the cell. One can notice that leak rates at higher load were slightly higher than the rates at lower load, see Figure 3.30. Although the water production at 50A would be higher, the reason for the higher amounts of leak rates was due to the higher flow rate of hydrogen, namely 1.42 and 0.66 SLPM for 50A and 20A loads respectively.

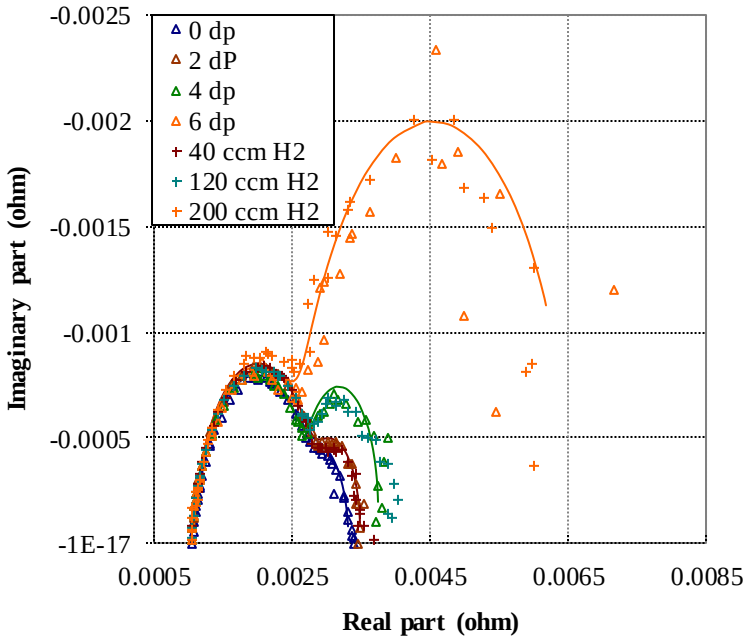


Figure 3.29: dP Impedance of a single cell and injected hydrogen at 20A load

The effect of water production on leak rate during operation can be analyzed by testing the amount of hydrogen leak rate off-line in a single leaky-cell test at OCV. In order to eliminate recombination of the leaked hydrogen with oxygen, nitrogen was used instead of air in the cathode side. In this off-line test, the hydrogen flow rate is increased

slowly while the anode outlet shut-off valve (see Figure 3.28) is closed. In this configuration, the hydrogen entering the anode has nowhere to go except through the membranes of the good cells and (mostly) through the pinhole of the leaky-cell, where increasing the hydrogen flow at the anode side, increases the dP through the inlet of the MEA, where this was measured as shown in Figure 3.31. To reduce the condensation at the stack, the medium leaky cell was placed in between two normal MEAs. As it can be noticed from the Figure 3.32 (a), the dP of the anode above the cathode was increasing steadily while increasing the flow rate. However, between 6 and 8 psi dP the flow was hindered due to the condensation of water in the stack. This drop in dP can be noticed between 1:15 to 1:30 hours where resistance to the flow was not corresponding to the increase in the hydrogen leak rate, see Figure 3.32 (b).

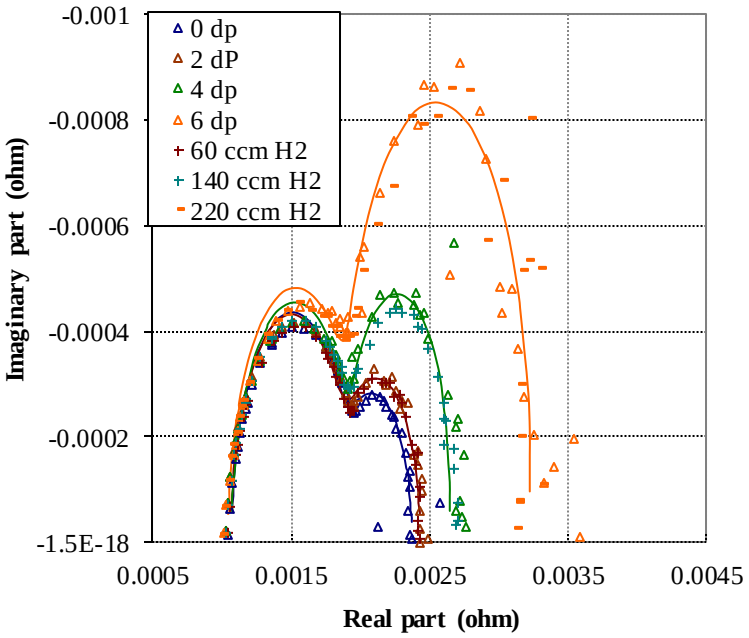


Figure 3.30: dP Impedance of a single cell and injected hydrogen at 50A load

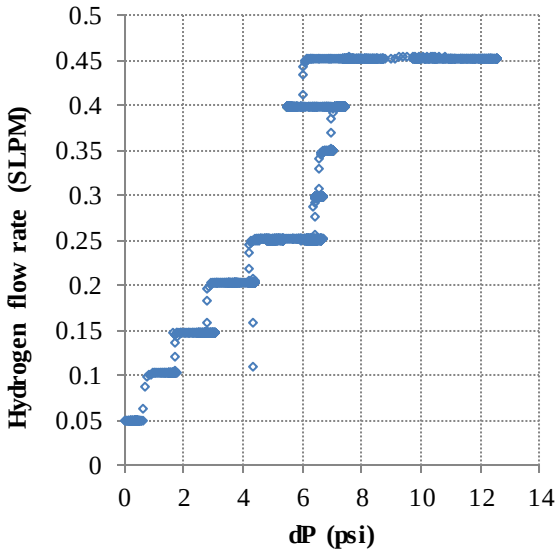


Figure 3.31: dP versus hydrogen leak rate of a medium leaky cell during off-line

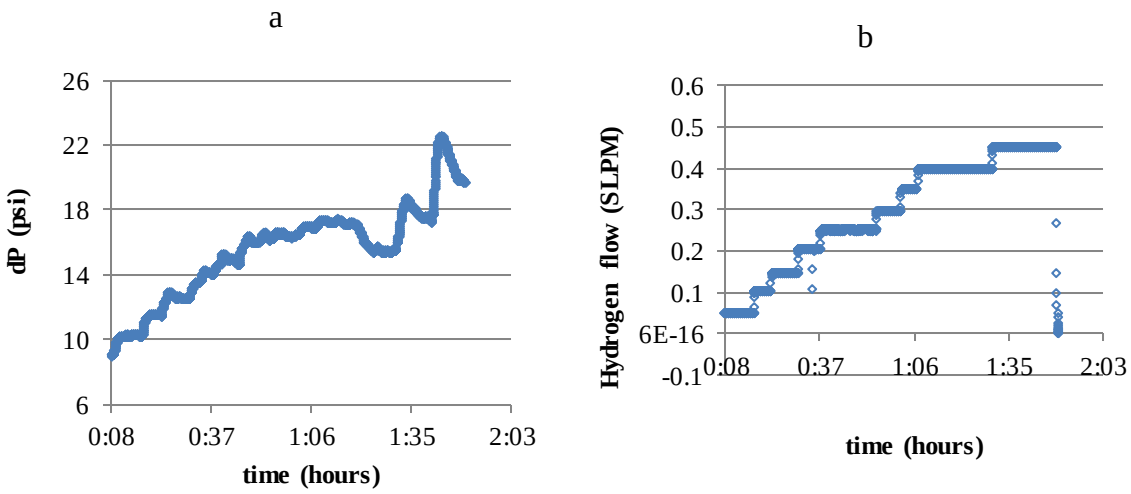


Figure 3.32: dP versus time (a) and hydrogen flow versus time (b)

## 3.3. Conclusion

Compared with the voltage signature, EIS showed superior ability in detecting hydrogen leak for either a single cell or a multi-cell stack. With the increasing leak rate and/or reducing oxygen concentration in the cathode side, the drop in the stack voltage

was minimal. In contrast, the impedance change was clear and consistent even with very small leak rates. Studying the effect of leak on a single cell, we detected hydrogen crossover leaks at different rates in the state of the art automotive PEM cell by using EIS. Studying the effect of membrane leak on a stack level, we confirmed the ability of EIS to detect leaks in large number of PEM fuel cells. EIS were mainly changing in the mass transport region. This indicated the reduction of oxygen in the cathode side with increasing leak rate. The higher the leak rate was, the larger the change in the signature and the more the consumption of oxygen at the cathode.

The impedance signatures were analyzed by using an equivalent circuit model. Fitting the signatures to the equivalent model, we found similarity in the parameter behavior between the leak rates and oxygen concentration signatures. The change in the parameters was especially clear with the large leak rate in a small stack size. However, with decreasing the leak rates and/or increasing the stack size, the change in the parameters was not significant. This reduction in the parameters resolution was partially due to the water sealing of pin-holes at smaller leak rates. In the next chapter we examine the existence of water at the cathode experimentally. The effect of water on the leak rate is analyzed using NN method.

# Chapter 4. Design and Implementation of a Neuro/Fuzzy EIS diagnostic system

The word diagnostic usually implies detection, isolation and identification of faults. As discussed in Chapter 3, the use of EIS in detecting transfer leak was very effective. However, EIS gave no information about the amount of leak rates. Thus, we used NN to estimate the amount of leak in the stack counting the effect of extra water resulting from the leak. We proposed a fuzzy rule base as a diagnostic system that can be used during the operation of the stack. This system will be analyzed using different amount of leak rates.

## 4.1. Estimation of hydrogen leak rate

Impedance signatures showed a clear relation between oxygen consumption and hydrogen leaks. However, the signatures alone cannot be used to quantify leak rates. Thus, NN was used to quantify the recombined amount of oxygen in the cathode due to leak. Aiming to identify the amount of hydrogen leak in the stack without measuring it directly, NN was used to map oxygen concentration impedance data with dP impedance data. This mapping was made by training the network using oxygen concentration impedance with its associated concentrations, see Figure 4.1.

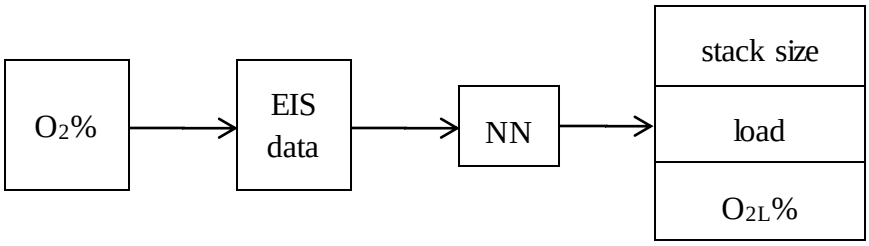


Figure 4.1: A schematic diagram of neural network training

With the increasing amount of dP at the inlet of the MEA, hydrogen leak increases through the pinholes. Having no access to the upstream of the MEA where the pinholes are, we estimated the leak rate by using oxygen concentrations simulated by the NN at different dPs. Oxygen stoich (utilization) was calculated by using equation (3.2).

The oxygen left in the cathode after consumption for a single cell is:

$$O_{2L} = [flow \cdot O_2] - [0.0167 \cdot I \cdot 0.2095] \quad (4.1)$$

The change in impedance signatures due to the reduction of oxygen concentrations was linked to the percentages of $O_{2L}$ using NN. Simulating the amount of recombined oxygen at different dPs using the trained network, we can calculate the amount of oxygen used in the electrochemical reaction by subtracting $O_{2L}$ flow from the regular amount of oxygen in the air flow. Then the current resulted from the consumption of oxygen at the cathode can be calculated. Subtracting the current at 0 dP from the current at higher leak rates, the leak current can be derived. This current was then used in estimating the consumed hydrogen due to leak by:

$$Q_{H2} = I_{leak} \cdot 0.0069478 \cdot \lambda_{H2} \quad (4.2)$$

A study by Hsueh [55] used the absolute value and phase angle of the impedance signatures in training the NN. Instead, we used the imaginary and real parts of the impedance in training the network, see Figure 4.2. The training signatures contained 112 impedance values measured over the range of 1260 to 0.156 Hz. Several trials were conducted in training the feed-forward network, until a proper network structure was achieved – including size of data, number of hidden layers, and number of neurons. As a general rule of thumb, the larger the training data is, the better the conversion of the network.

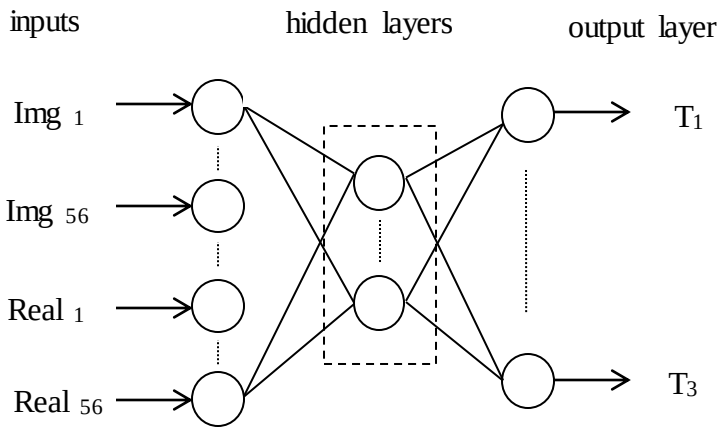


Figure 4.2: Neural network topography 112:20:3

The training was performed with 144 impedance data of the stack sizes 5, 9 and 19-cell and 20 neurons in the hidden layer. Experiments conducted for the no leaks stack and the stacks with small, medium size leaky cells at 20 and 50 A loads were used in training. The network targets were: number of cells in the stack, load, and the percentage of oxygen concentration left in the cathode after consumption $\%O_{2L}$, as shown in Table 4.1. The $\%O_{2L}$ at 20A was less than the $\%O_{2L}$ at 50A due to the higher flow at higher loads, (see Table 3.2). In training the network we used MATLAB 7.5 with a Levenberg-Marquardt backpropagation function (trainlm) of MATLAB optimization algorithm that is usually the best suited for function approximation problems. The network was trained until sum of the square of errors reached just below 0.01.

Table 4.1: Target vectors of n-cell stack network

| | | | | | | | | | | | | | | | | | | |
|---|---|---|---|---|---|---|---|---|---|---|---|---|---|---|---|---|---|---|
| # cells | 5 | ... | 5 | 9 | ... | 9 | 19 | ... | 19 | 5 | ... | ... | 9 | ... | ... | 19 | ... | 3 × 144 |
| load | 20 | ... | 20 | 20 | ... | 20 | 20 | ... | 20 | 50 | ... | ... | 50 | ... | ... | 50 | ... | |
| $O_2$ % | 14.58 | ... | 3.8 | 14.58 | ... | 3.8 | 14.58 | ... | 3.8 | 19.8 | ... | ... | 19.8 | ... | ... | 19.8 | ... | |

After training, we used the network in simulating dP impedance data. The oxygen concentrations resulting from the simulation were then used in calculating the hydrogen leaks at different stack sizes. Using the average oxygen concentration in 20A and 50A loads, hydrogen leaks in the small, medium and large leaky cells were estimated. The estimated leak rates were proportional to the size of measured ex-situ leak rates of the leaky cells (measured with air). For the small leaky cell, a small drop in oxygen

concentration was noticed over the range of dP. This drop was represented in the small number of hydrogen leak rates at 20A and 50A loads, see Figure 4.3. A larger drop was noticed for the medium leaky cell, see Figure 4.4. For the large leaky cell, the concentration drop was significant with the increase of dP. This drop was reflected in the increasing of leak rates at higher dP, see Figure 4.5.

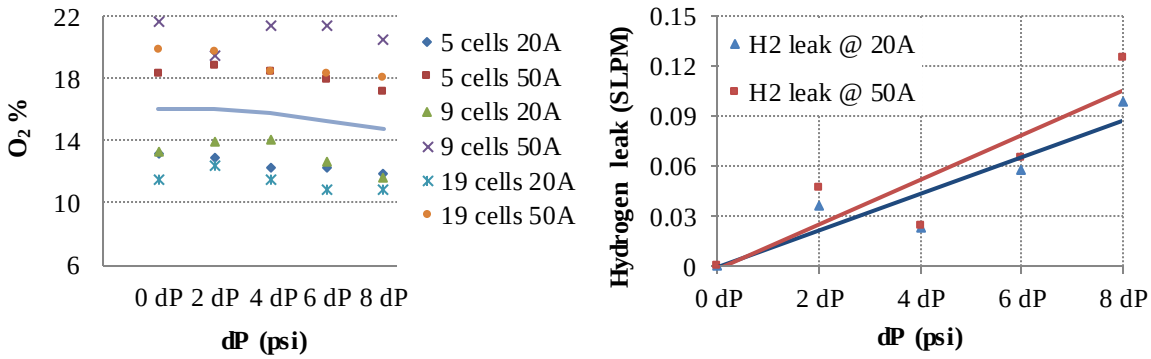


Figure 4.3: Oxygen concentration (left) and hydrogen leak rate (right) of a small leaky cell in n-cells stack

NN simulation shows a continuous reduction in oxygen concentration with the increasing of dP. This agrees with our observation that the reduction of impedance at higher dP is the result of loss in the leaky cell due to the loss of sufficient amounts of oxygen. The continuous reduction in concentration gives a clear indication that the network was able to learn the correct behavior of the impedance. However, the hydrogen leak estimation was less than the off-line ex-situ measured leak rates, see Figure 4.6. This difference might be the result of an excess amount of water in the cathode due to recombination partially sealing the pin holes.

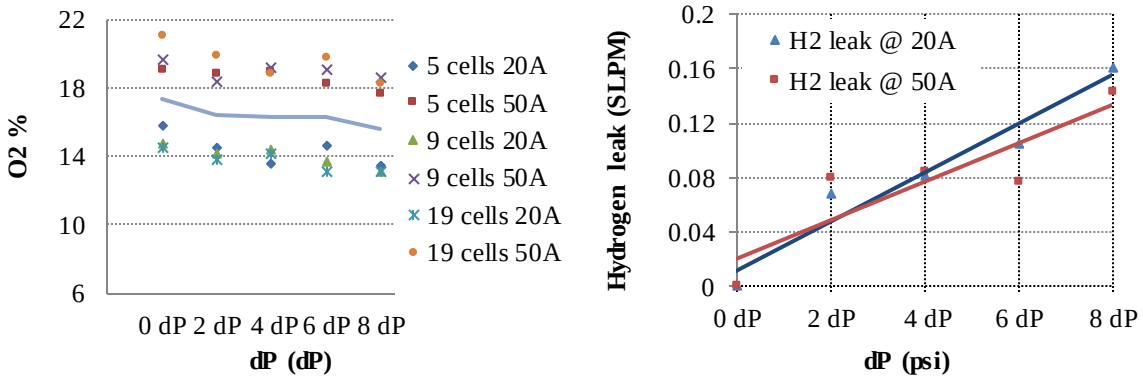


Figure 4.4: Oxygen concentration (left) and hydrogen leak rate (right) of a medium leaky cell in n-cells stack

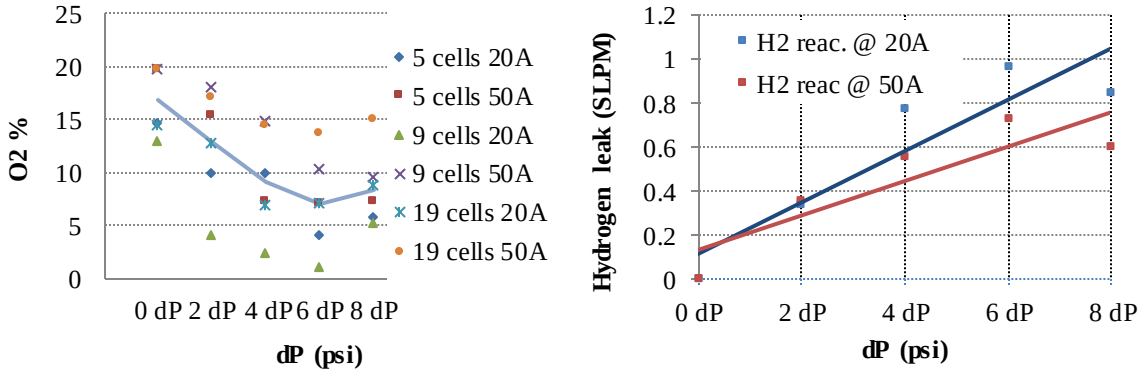


Figure 4.5: Oxygen concentration (left) and hydrogen leak rate (right) of a large leaky cell in n-cells stack

Comparing the leak rate during operation at 20A load and during off-line, the effect of recombination can be noticed, in Figure 4.6. As expected, the maximum leak rate was measured during the off-line mode, and the estimated leak rate was closer to the on-line leak rate. Error between estimated and on-line leak rates were negligible at 2 psi dP. However, at higher dP the error was higher. This should not affect the feasibility of the estimation method where anode pressure is usually kept a little higher than the cathode pressure in most systems. Thus, this method suits the diagnostic criteria needed for the fuel cell stack.

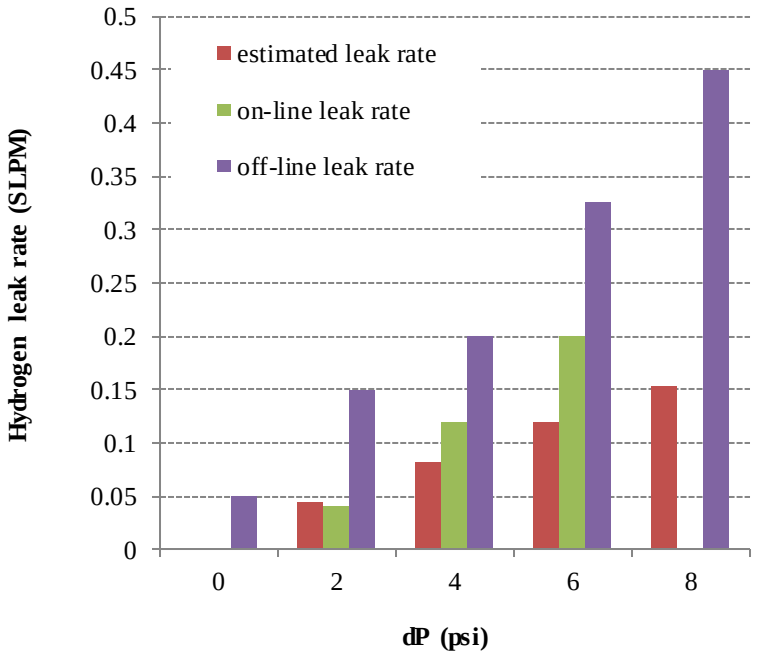


Figure 4.6: Measured and estimated leak rates

## 4.2. Modeling the impedance signature

The Randles circuit is a first-order differential, equation (2.7). The transfer function of this circuit can be represented in the Laplace form by:

$$Z(s) = R_o + \frac{1/C}{s + 1/RC} \tag{4.3}$$

Applying a unit step input, $I(s)$ to the impedance resulted in:

$$V(s) = I(s) \cdot Z(s) = \frac{A}{s} \cdot \left[ R_o + \frac{1/C}{s + 1/RC} \right] \tag{4.4}$$

To solve this expression, a partial fraction expansion can be used:

$$V(s) = \frac{A \cdot \left[ sR_o + \frac{1}{C}\left(\frac{R_o}{R} + 1\right) \right]}{s\left(s + 1/RC\right)} = \frac{X}{s} + \frac{Y}{\left(s + 1/RC\right)} \tag{4.5}$$

Solving for X:

$$X = \frac{A\cdot\left[sR_o+\frac{1}{C}\left(\frac{R_o}{R}+1\right)\right]}{s\left(s+{}^{1}/_{RC}\right)} \xrightarrow{s=0} A(R_o + R) \qquad (4.6)$$

Solving for Y:

$$Y = \frac{A\cdot\left[sR_o+\frac{1}{C}\left(\frac{R_o}{R}+1\right)\right]}{s} \xrightarrow{s=-{}^{1}/_{RC}} AR \qquad (4.7)$$

Substituting $X$ and $Y$ in equation (4.5) and converting back to time domain:

$$V(t) = A\left[(R_o + R) - Re^{-t/\tau}\right] \qquad (4.8)$$

where $\tau$ is the time constant $RC$ and $A$ is the load.

Using the parameters resulting from fitting the impedance data in the previous chapter, we can now estimate the voltage resulting from the change in concentrations and dPs. Taking the difference in voltage between two consequent measures, we can estimate the voltage resulting from the change in the mass transport region. This voltage represents the change in the impedance signatures where the charge transfer region was mostly not affected, as it can be seen from Figure 3.22. For the first three consecutive signatures; namely [21, 19, 17] $O_2$%, the difference in estimated and measured voltages were in a good match, see Figure 4.7. This was mainly due to the good fitting of the Randles circuit with the impedance signatures. However, the tumbling of the fitting at later signatures at lower concentrations resulted in a bigger difference between the estimated and measured voltages.

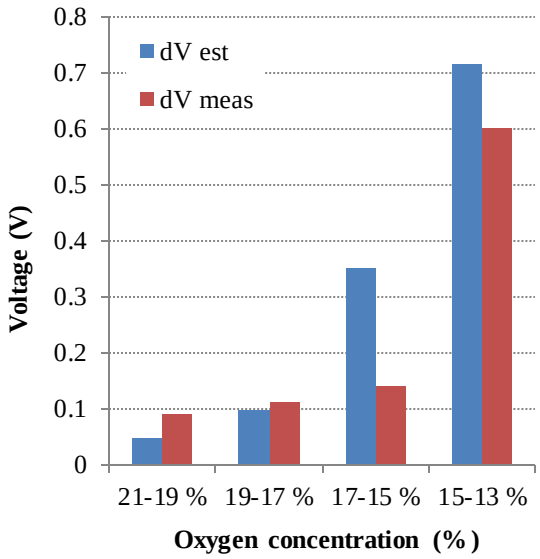


Figure 4.7: Estimated and measured voltages of a 19-cell stack at 20A at low oxygen concentration

The difference between the estimated and measured voltages is an indication of oxygen loss in the cathode side. When the stack suffers air starvation, the estimated voltage difference was higher than the measured voltage difference due to the sharp drop in the measured stack voltage, see Figure 4.8. The estimated voltage was also high in case of a large stack size at high dP with a large and medium leaky cell respectively, see Figure 4.9 (a) and (b). However, for the same stack size with a small leaky cell, the estimated voltage difference cannot detect the leak, see Figure 4.9 (c). Using the estimated voltage difference derived from the circuit parameters we added a new feature to the diagnostic system beside the impedance signature. This will increase our ability to detect crossover in a multi-cell stack.

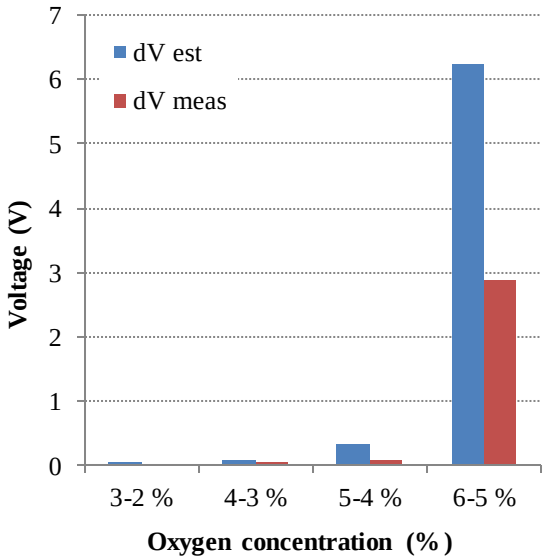


Figure 4.8: Estimated and measured voltages of a 9-cell stack at 20A at air starvation

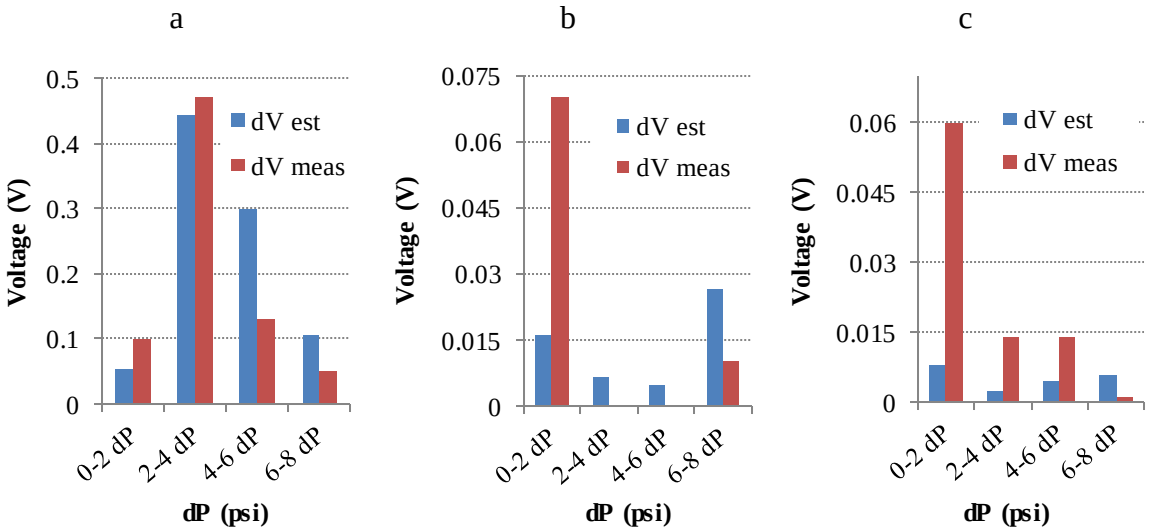


Figure 4.9: Estimated and measured voltages of a 19-cell stack at 20A load with large leaky cell.

Note: (a), medium leaky cell (b) and small leaky cell (c) with different dP

## 4.3. Detecting hydrogen leak

Measuring two consecutive impedance signatures and estimating their voltages is not feasible during the stack operation where we only have an access to the impedance

we measure. To avoid this issue we can compare the measured impedance to the stack impedance at normal operating conditions. For a large stack with a large leaky cell, the measured voltage difference is increasing with the increasing of leak rate, see Figure 4.10 (a). At the heights leak rate, the difference between the normal voltage at 0dP and the voltage at 8dP was 0.75V. This was a clear indication that the leaky cell is losing its contribution to the total stack voltage due to air starvation where each the cell voltage in normal operating condition is about 0.8V. In the other hand, the estimated voltage difference was small due to the shrinking of the impedance signature at 8dP. Such clear voltage difference signatures were not noticed in case of the large stack size with a medium leaky cell, see Figure 4.10 (b). When the stack was air staving, the difference between measured and estimated voltages were big due to the drop in stack voltage, see Figure 4.11.

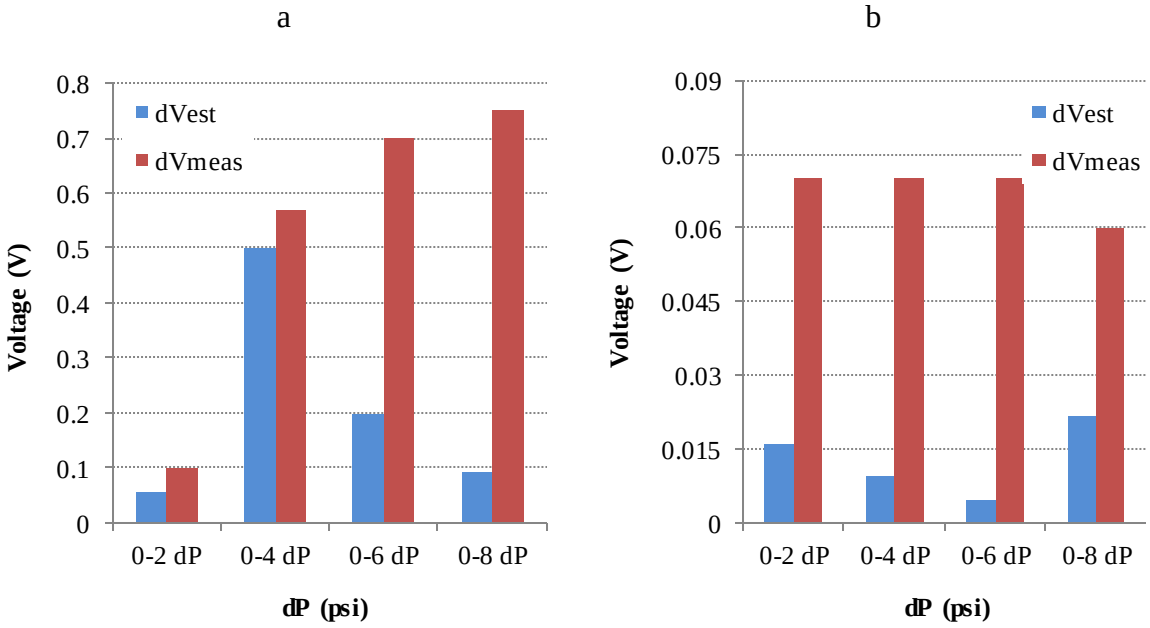


Figure 4.10: Estimated and measured voltages of a 19-cell stack at 20A.
Note: a large leak cell (a) and a medium leak cell (b)

Using the relationship between the estimated and measured voltages, we built a fuzzy logic rule-base as:

1 If *dVmeas* is small and *dVmeas - dVest* is small then leak is *VSleak*.

2 else If *dVmeas* is med and *dVmeas - dVest* is small then leak is *Sleak*.

3 else If *dVmeas* is large and *dVmeas - dVest* is med then leak is *Mleak*.

4 else If *dVmeas* is large and *dVmeas - dVest* is large then leak is *Lleak*.

5 else If *dVmeas* is very large and *dVmeas - dVest* is very large then leak is H2 emission.

where:

dVmeas is the change in measured voltage

dVmeas- dVest is the difference between the change in measured voltage and the change in estimated voltage

VSleak is very small leak rate

Sleak is small leak rate

Mleak is the medium leak rate

Lleak is the large leak rate

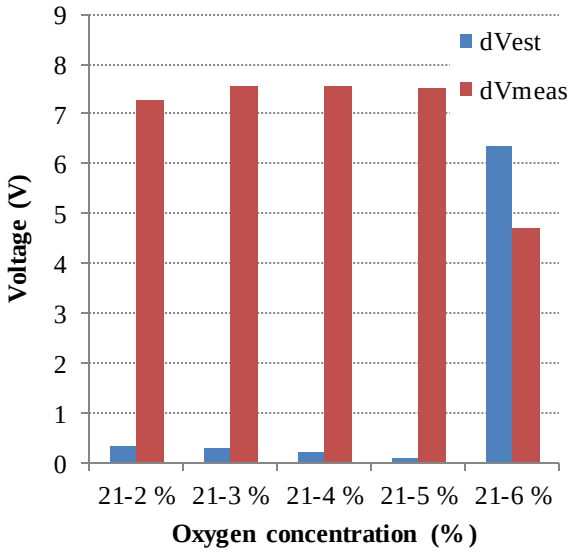


Figure 4.11: Estimated and measured voltages of a 9-cell stack at 20A t air starvation

The fuzzy rule base can be utilized by fuzzifying the readings of the dV measured voltage, dV estimated voltage and the difference between them using membership functions in Figure 4.12. Based on our previous knowledge, we selected the small, medium and large input values of those functions respectively. Based on those inputs, the

output of the fuzzy system showed the amount of leak as very small (VSleak), small (Sleak), medium (Mleak), large (Lleak), very large (VLleak) and hydrogen emission (H2emission).

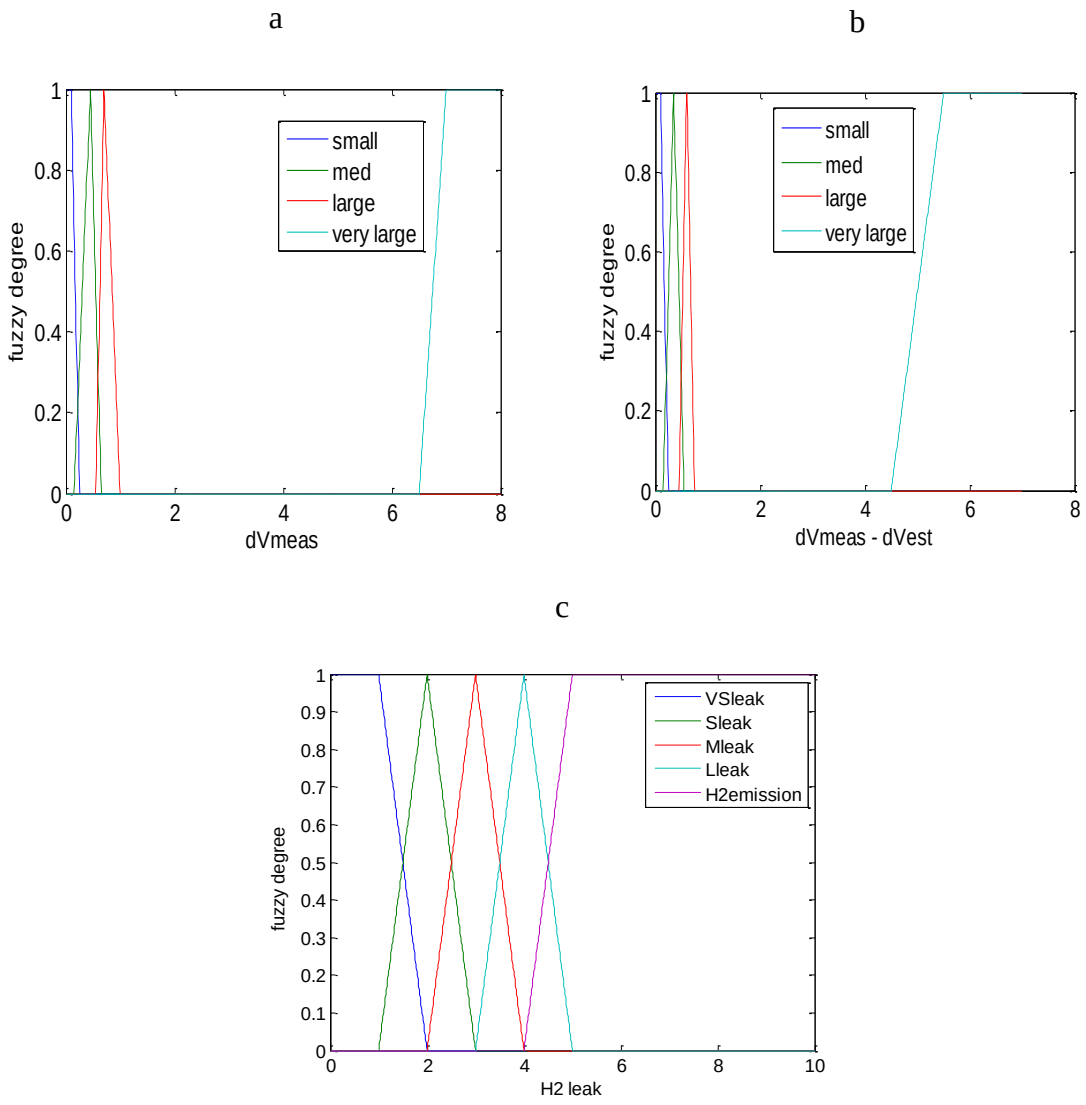


Figure 4.12: Fuzzy membership functions of a 9-cell stack at 20A.
Note: (a) dV measured, (b) the difference between the dV measured and dV estimated, (c) hydrogen leak

The proposed diagnostic system was tested with the impedance of a 19-cell stack with two leaky cells placed at the middle of normal cells, see Figure 4.13. The leaky cells

are a medium leaky cell and staved cell. The staved cell leak rate is similar to the leak rate of the medium leaky cell. Calculating dV for this impedance signature:

$$dVmeas = Vmeas_{0dP} - Vmeas_{8dP} \quad (4.9)$$

= 16.06 - 15.31

= 0.75 V

Taking the limits of the estimated voltages and substitute it in equation (4.10):

$$dVest = Vest_{0dP} - Vest_{8dP} \quad (4.10)$$

= 1.09 - 1.18

= 0.09 V

One can notice the difference between the values of Vmeas and Vest. This was due to the fact that Vmeas is the stack total voltage while Vest is the voltage resulted from fitting only the second arc of the impedance. Applying the rule-base on this measured impedance resulted in a large leak rate, rule 4, where the *dVmeas* is large and *dVmeas - dVest* is large. This agreed with our leak rate estimation where the contribution of both leaky cells is counted as a large leaky, see Figure 4.4 and 4.5. However, the diagnostic system was not able to count the number of leaky cells where the dVmeas is within the range of a single cell.

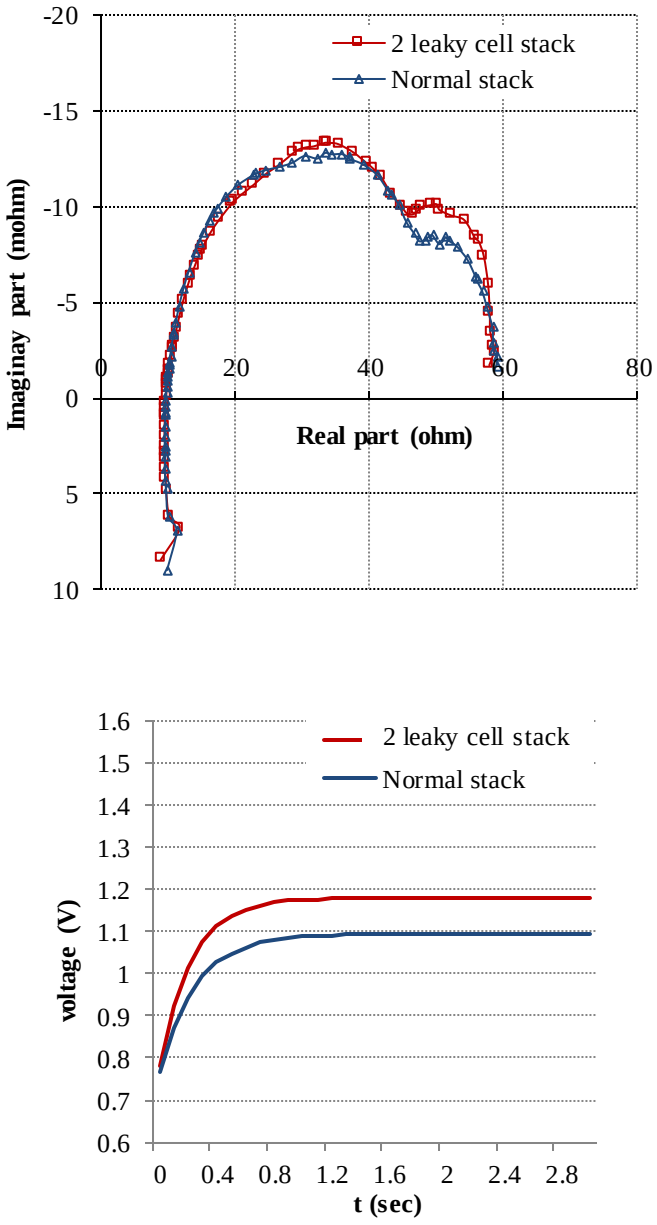


Figure 4.13. Impedance signatures of a 19-cell stack and its estimated voltages with two leaky cells (medium and starved cell)

## 4.4. Conclusion

We used NN in detecting hydrogen crossover to represent the complex behavior of the fuel cell system without the need of deriving a mathematical model. This allowed

us to take into consideration the effect of leak rate on the fuel cell system without the need of prior knowledge to the interior mass and heat transfer encountered. We employed the relationship between the reduction of oxygen concentration and the increase of leak rate in training the network. The similarity in both of the impedance signatures allows us to utilize the impedance measurements in back calculating the hydrogen leak rate. The network training was successful because of the consistent patterns of the impedance signatures and the availability of a large set of experimental data.

To count the overall faults encountered due the crossover, we used the FL method. Based on the relationship between the change in estimated voltage and measured voltage, we built the fuzzy logic rule-base. The estimated voltage can be calculated by first fitting the impedance signature to the Randles circuit, and then by getting the circuit parameters. The use of the difference between the change in estimated and measured voltages introduced a new feature to the diagnostic system. This feature fuses the impedance and voltage measurements of the stack in a simple and straightforward criteria.

# Chapter 5. Conclusions

In this multidisciplinary research, we proposed a Neuro-fuzzy diagnostic system for PEM fuel cell stacks, based on the EIS technique. The purpose of this system was to detect, isolate and identify the type of hydrogen crossover fault. We started by analyzing the effect of hydrogen leak on a single cell using EIS. Based on the ability of EIS to detect hydrogen leak in a single cell, we extended our study to a stack with larger number of cells. Using a multi-cell stack, we were able to understand the behavior of the impedance at air starvation. We analyzed the impedance behavior based on the voltage measurements and equivalent electrical circuit used to fit the impedance data. In our diagnostic system, we first estimated the amount of leak rate using neural network. Then we proposed the use of fuzzy logic to determine the hydrogen crossover leak and emission faults.

Experimental work

We conducted more than 200 experiments (see the Appendices) using cells with various leak rates placed in different stack sizes. Our purpose was to understand the stack behavior in the case of leaks, identify a proper detection tool, and finally recognize the effect of faults on signatures. Toward our understanding of the stack behavior, we tested many leak configurations. Cells with small, medium and large leak rates with pin-holes located at the MEA inlet or outlet were tested and compared to the normal cell behavior. To check the effect of the existence of two leaky cells on the impedance, we placed large and medium leaky cells in a multi-cell stack. No major effect was noticed due to the domination of the large leak on the impedance signature.

A shorted cell with pin-holes distributed all over the MEA was also tested. The distribution of holes resulted in a distorted impedance signatures compared to the leaky cells with holes located at the outlet especially with lower load. One explanation of the noisy signal associated with lower load is that when dP increases, the leak is intermittent through the MEA. This intermittence in the hydrogen leak was due to the 'self-sealing' of holes by the existence of water at the cathode side. However, when water production increased with the increase of load, lesser amount of hydrogen is leaking through the holes. This resulted in a cleaner impedance signature at higher loads.

Our experimental analysis showed that the important part of the impedance was the mass transport region where the impedance was measured at low frequencies. In this region the measurements were slower than the charge transfer region that was measured at high frequencies. To reduce the measurement time, we reduced the moving average. One problem we noticed while measuring the impedance is the signal interference with the surrounding devices. This affected the impedance signature and resulted in distortion of the data. After we isolated the interference source, i.e. the power source, the distortion was eliminated from the impedance data. We concluded that the bandwidth is required to be uniquely selected for a successful implementation of EIS measurement.

Hydrogen crossover detection

EIS was very efficient in detecting hydrogen leaks and oxygen concentrations in a single and multi-cell PEMFC stack with different sizes and leak rates. With the increase of hydrogen leak rates at the stack inlet, impedance signatures changed mostly in the mass transport region. Similar behavior was noticed with the reduction of oxygen concentrations in the cathode. This similarity in the impedance signatures showed us that leak rate and oxygen concentration were interchangeable where the increase of leak resulted in more oxygen recombination at the cathode. Using the equivalent circuit, we were able to identify the important parameters associated with the change in impedance signatures. Analyzing parameters of the signatures with pin-holes located at the stack

outlet, we noticed no significant change. This was due to the consumption of hydrogen along the MEA.

With the decreased amounts of oxygen at the cathode, impedance signatures at the mass transport region increased due to the lack of oxygen available for electrochemical reaction at the cathode side. At air starvation however, the impedance shrank down due to the reduction of stack voltage. Monitoring the stack voltage was useful in detecting the onset of air starvation where the voltage-drop with air stoich was less than 1.5. However, the fall in voltage after full starvation was barely noticed compared to the impedance that kept changing even with very small amounts of oxygen at the cathode. At this low percentage of oxygen concentration in the cathode, we detected unsafe levels of hydrogen emission.

Diagnostic system

The interchangeable effect in the leak rates and oxygen concentrations impedance was used to estimate the amount of hydrogen leak rate in a stack using a neural network method. The network training was conducted using the oxygen concentrations impedance data. The network simulation was then used in back-calculating the hydrogen leak rate in the stack. Leak rates were estimated effectively during operation of the fuel cell system. However, this estimation differs from the off-line ex-situ leak measurements, likely because of the existence of water produced in operation blocking or partially-blocking the pinholes. At lower dPs, the on-line and estimated leak rates are almost identical, while at higher dPs the off-line measured leak rates are typically higher. This showed the feasibility of the diagnostic method, where most the dPs across the MEAs are usually kept small in most fuel cell systems.

In the case of hydrogen internal leak, the impedance resolution decreases with the reduction of hydrogen leak rate and/or the increase of stack size. This affects the ability of the impedance to detect crossover fuel leaks. To overcome this issue, we used the impedance signature to estimate the voltage. Aiming to increase the diagnostic ability

especially at small amount of leak rate and/or large stack size, we fused the impedance and voltage measurements by using a first order differential equation model. We compared the difference in the estimated voltage to the measured voltage with respect to the stack at normal operation. Using an 'if/then' fuzzy rule base, we monitored the internal hydrogen leak and hydrogen emissions in a multi-cell stack. Comparing the difference between estimated and measured voltages allowed us to detect hydrogen leaks where the impedance signature by itself cannot.

In conclusion, this study allowed us to understand and diagnose hydrogen crossover in PEM fuel cells. We showed that the use of impedance in detecting hydrogen leak and/or air starvation is very useful in any potential on-board health monitoring system. The use of neural network in estimating the amount of hydrogen leak rate might determine the useful operation of the bus module before maintenance and increase the warranty period. Fusing the stack impedance and voltage measurements by using fuzzy method intensified the ability of the fault detection. Such a fuzzy system can be used in the future to monitor the stack health during operation. This will increase the durability of Ballard's fuel cells buses and increase its market share as a promising alternative power source.

Future work

For a successful implementation of the diagnostic system on-board a vehicle, compact size and low cost must be taken into consideration. The system needs to monitor the performance of hydrogen sensors installed at the stack cathode outlet and the module vent outlet. This allows for effective condition-based maintenance where the sensors calibration and/or replacement are performed only when needed. Upon identification of an onset of a fault, a mitigation criterion is required. This can be done by installing a control system that is able to reduce hydrogen leak through the MEA by the means of controlling the differential pressure between anode and cathode, and/or by increasing cathode air flow to mitigate emissions. In general, specific steps are required for a feasible, durable and low cost on-line diagnostic system:

- Optimizing the numbers of impedance measurements that illustrate the status of the leak at different rates. This can be done by selecting a specific number of frequencies that give full description of the stack status.
- Identifying the resolution of the impedance signature that can recognize the smallest amount of leak rate at the biggest stack size.
- Studying the effect of the existence of other faults in the signal. Isolation and proper identification of each fault must be established.

A proper design should consider the aforementioned steps. This design should be able to measure the impedance of a large stack size. Further, an appropriate design of a loadbank and frequency analyzer able to deal with the power of a large module is needed. Integration with the control system is required to reduce power loss in the case of leak. A potential interface with the hydrogen sensors, pressure valves and air pump may also be needed for an efficient diagnostic system design.

For a new MEA design with a different active area, a new set of experimental work can be established. The impedance of a 19-cell stack with a leaky cell can be measured at different oxygen concentrations and dPs. A set of leaky cells with different leak rates can be tested. The measured impedance can be used to estimate the amount of hydrogen leak rate using NN. A fuzzy rule base can combine the readings of impedance and voltage using to detect the hydrogen leak and emission in a FC stack.

# References


[1] C. C. Chan. The state of the art of electric, hybrid, and fuel cells vehicles. roceedings of IEEE, 95 (4): 704-718, 2007.

[2] M. Mench. *Fuel Cell Engines*. Wiley, 2008.

[3] G. Zhang, S. Shen, L. Guo, H. Liu. Dynamic characteristics of local current densities and temperatures in proton exchange membrane fuel cell during reactant starvation. *International Journal of Hydrogen Energy*, 37 (2): 1884-1892, 2012.

[4] H. Tang, Z. Qi, M. Ramani, J. F. Elter. PEM fuel cell cathode carbon corrosion due to the formation of air/fuel boundary at the anode. *Journal of Power Sources*, 158 (2): 1306-1312, 2006.

[5] N. Yousfi-Steiner, Ph. Mocoteguy, D. Candussoc, D. Hissel. A review on polymer electrolyte membrane fuel cell catalyst degradation and starvation issues: Causes, consequences and diagnostic for mitigation. *Journal of Power Sources*, 194 (1): 130-145, 2009.

[6] Mk902 Recombination Effectiveness Test 2,Ballard internal report, RPT5101914, 2004.

[7] S. Kreitmeier, M. Michiardi, A. Wokaun, F. N. Buchi. Factors determining the gas crossover through pinholes in polymer electrolyte fuel cell membrane. *Electrochimica Acta*, 80: 240-247, 2012.

[8] S. D. Knights, K. M. Colbow, J. St-Pierre, and D. P. Wilkinson. Aging mechanisms and lifetime of PEFC and DMFC. *Journal of Power Sources* 127 (1-2): 127–134, 2004.

[9] X.-G. Yang, Q. Ye, and P. Cheng. Hydrogen pumping effect induced by fuel starvation in a single cell of a PEM fuel cell stack at galvanostatic operation. *International Journal of Hydrogen Energy*, 37 (19): 14439–14453, 2012.

[10] M.-T. Nguyen, S. A. Grigoriev, A. A. Kalinnikov, A. A. Filippov, P. Millet, and V. N. Fateev. Characterization of a electrochemical hydrogen pump using electrochemical impedance spectroscopy. *Journal of Applied Electrochemistry*, 41 (19): 1033-1042, 2011.

[11] D. Liang, Q. Shen, M. Hou, Z. Shao, and B. Yi. Study of the cell reversal process of large area proton exchange membrane fuel cells under fuel starvation. *Journal of Power Sources*, 194 (2): 847–853, 2009.

[12] A. Taniguchi, T. Akita, K. Yasuda, and Y. Miyazaki. Analysis of degradation in PEMFC caused by cell reversal during air starvation. *International Journal of Hydrogen Energy*, 33 (9): 2323–2329, 2008.

[13] A. Z. Weber. Gas-crossover and membrane-pinhole effects in polymer-electrolyte fuel cells. *Journal of the Electrochemical Society*, 155 (6): B521-B531, 2008.

[14] R. Lin, E. Gülzow, M. Schulze and K. A. Friedrich. Investigation of Membrane Pinhole Effects in Polymer Electrolyte Fuel Cells by Locally Resolved Current Density. *Journal of the Electrochemical Society*, 158 (1): B11-B17, 2011.

[15] S. Nakamura, E. Kashiwa, H. Sasou, S. Hariyama, T. Aoki, Y. Ogami, and H. Nishikawa. Measurement of leak current generation distribution in PEFC and its application to load fluctuation testing under low humidification. *Electrical Engineering in Japan*, 174 (1): 1-9, 2011.

[16] B.T. Huang, Y. Chatillon, C. Bonnet, F. Lapicque, S. Leclerc, M. Hinaje, and S. Rael. Experimental investigation of pinhole effect on MEA/cell aging in PEMFC. *International Journal of Hydrogen Energy*, 38 (1): 543-550, 2013.

[17] M.R. Ashraf Khorasani, S. Asghari, A. Mokmeli, M.H. Shahsamandi, and B. F. Imani. A diagnosis method for identification of the defected cell(s) in the PEM fuel cells. *International Journal of Hydrogen Energy*, 35 (17): 9269-9275, 2010.

[18] G. Tian, S. Wasterlain, D. Candusso, F. Harel, D. Hissel, and X. Francois. Identification of failed cells inside PEMFC stacks in two cases: Anode/cathode crossover and anode/cooling compartment leak. *International Journal of Hydrogen Energy*, 35 (7): 2772-2776, 2010.

[19] J. Wu, X. Z. Yuan, H. Wang, M. Blanco, J. J. Martin, and J. Zhang. Diagnostic tools in PEM fuel cell research:

Part I, electrochemical techniques, *International Journal of Hydrogen Energy*, 33 (6): 1735 – 1746, 2008.

Part II, Physical/chemical methods, international journal of hydrogen energy 33 (6): 1747–1757, 2008.

[20] J. Kang, D. W. Jung, S. Park, J. Lee, J. Ko, and J. Kim. Accelerated test analysis of reversal potential caused by fuel starvation during PEMFCs operation. *International Journal of Hydrogen Energy*, 35 (8): 3727-3735, 2010.

[21] C. Brunetto, A. Moschetto, and G. Tina. PEM fuel cell testing by electrochemical impedance spectroscopy. *Electric Power Systems Research*, 79 (1): 17–26, 2009.

[22] M. Ciureanu, and R. Roberge. Electrochemical impedance study of PEM fuel cells. experimental diagnostics and modeling of air cathodes. Journal of Physical Chemistry, 105 (17): 3531-3539, 2001.

[23] S. Rodat, S. Sailler, F. Druart, P.-X. Thivel, Y. Bultel, and P. Ozil. EIS measurements in the diagnosis of the environment within a PEMFC stack. Journal of Applied Electrochemistry, 40 (5): 911–920, 2010.

[24] J. Kawaji, S. Suzuki, Y. Takamori, T. Mizukami, and M. Morishima. Microstructure of platinum-carbon agglomerates with hydrocarbon-based binder and its effect on the cathode performance of PEFC. *Journal of Electrochemical Society*, 158 (8): B1042-B1049, 2011.

[25] R. Makharia, M. F. Mathias, and D. R. Baker. Measurement of catalyst layer electrolyte resistance in PEFCs using electrochemical impedance spectroscopy. *Journal of the Electrochemical Society*, 152 (5): A970-A977, 2005.

[26] U. Cano-Castillo, A. Ortiz, S. Cruz, L. G. Arriaga and G.Orozco. Parameter changes during gradual flooding of a PEM fuel cell through EIS studies. *ECS Transactions*, 3 (1): 931-939, 2006.

[27] H. Kuhn, B. Andreaus, A. Wokaun, and G.G. Scherer. Electrochemical impedance spectroscopy applied to polymer electrolyte fuel cells with a pseudo reference electrode arrangement. *Electrochimica Acta*, 51 (8-9): 1622-1628, 2006.

[28] S. J. Andreasen, J. L. Jespersen, E. Schaltz, and S. K. Kær. Characterisation and modelling of a high temperature PEM fuel cell stack using electrochemical impedance spectroscopy. *FUEL CELLS*, 9 (4): 463–473, 2009.

[29] X. Yuan, J. C. Sun, M. Blanco, H. Wang, J. Zhang, and D. P. Wilkinson. AC impedance diagnosis of a 500W PEM fuel cell stack, Part I: stack impedance. *Journal of Power Sources*, 161 (2): 920–928, 2006.

[30] A. M. Dhirde, N. V. Dale, H. Salehfar, M. D. Mann, and T.-H. Han. Equivalent electric circuit modeling and performance analysis of a PEM fuel cell stack using impedance spectroscopy. *IEEE Transactions on Energy Conversion*, 25 (3): 778-786, 2010.

[31] J. L. Jespersen, E. Schaltz, and S. K. Kær. Electrochemical characterization of a polybenzimidazole-based high temperature proton exchange membrane unit cell. *Journal of Power Sources*, 191 (2): 289–296, 2009.

[32] N. Fouquet. Real time model-based monitoring of a PEM fuel cell flooding and drying out. *Vehicle Power and Propulsion Conference*: 1-8, 2010.

[33] I. A. Schneider, D. Kramer, A. Wokaun, and G. G. Scherer. Oscillations in gas channels, II. Understanding the characteristics of the low frequency loop in air-fed PEFC impedance spectra. *Journal of the Electrochemical Society*, 154 (8): B770-B782, 2007.

[34] I. A. Schneider, S. A. Freunberger, D. Kramer, A. Wokaun, and G. G. Scherer. Oscillation in gas channels, I. The forgotten player in impedance spectroscopy in PEFCs. *Journal of the Electrochemical Society*, 154 (4): B383-B388, 2007.

[35] G. Mousa, F. Golnaraghi, J. DeVaal, and A. Young. Detecting proton exchange membrane fuel cell hydrogen leak using electrochemical impedance spectroscopy method. *Journal of Power Sources* 246: 110-116, 2014.

[36] X. Yan, M. Hou, L. Sun, D. Liang, Q. Shen, H. Xu, P. Ming, and B. Yi. AC impedance characteristics of a 2 kW PEM fuel cell stack under different operating conditions and local changes. *International Journal of Hydrogen Energy*, 32 (17): 4358-4364, 2007.

[37] M. Boillot, C. Bonnet, N. Jatroudakis, P. Carre, S. Didierjean, and F. Lapicque. Effect of gas dilution on PEM fuel cell performance and impedance response. *Fuel Cells*, 6 (1): 31-37, 2007.

[38] F. O Karray. and C. de Silva. *Soft Computing and Intelligent Systems Design, Theory, Tools and Applications*. Addison Wesley, 2004.

[39] D Hissel, M.C Péra, and J.M Kauffmann. Diagnosis of automotive fuel cell power generators. *Journal of Power Sources*, 128 (2): 239–246, 2004.

[40] J. O. Schumacher, P. Gemmarb, M. Denneb, M. Zeddaa, and M. Stueberb. Control of miniature proton exchange membrane fuel cells based on fuzzy logic", Journal of Power Sources, 129 (22): 143–151, 2004.

[41] J.P. Torreglosaa, F. Juradoa, P. Garcíab, and L.M. Fernándezb. Application of cascade and fuzzy logic based control in a model of a fuel-cell hybrid tramway. *Engineering Applications of Artificial Intelligence*, 24 (1): 1–11, 2011.

[42] C. Changzheng and M. Changtao. A method for intelligent fault diagnosis of rotating machinery. *Digital Signal Processing*, 14 (3): 203–217, 2004.

[43] J.-D. Wu, and C-H. Liu. An expert system for fault diagnosis in internal combustion engines using wavelet packet transform and neural network. Expert Systems with Applications, 36 (1): 4278–4286, 2009.

[44] S. Ou, and L. E.K. Achenie. A hybrid neural network model for PEM fuel cells. *Journal of Power Sources*, 140 (2): 319–330, 2005.

[45] J Lobato, Pablo Canizares, M. A. Rodrigo, J. J. Linares, C.-G. Piuleac, and S. Curteanu. The neural networks based modeling of a polybenzimidazole-based polymer electrolyte membrane fuel cell: Effect of temperature. *Journal of Power Sources,* 192 (1): 190–194, 2009.

[46] A. K.S. Jardine, D. Lin and D. Banjevic. A review on machinery diagnostics and prognostics implementing condition-based maintenance. *Mechanical Systems and Signal Processing*, 20 (7): 1483-1510, 2006.

[47] N. Yousfi-Steiner, D. Candusso, D. Hissel, and Ph. Mocoteguy. Model-based diagnosis for proton exchange membrane fuel cells. *Mathematics and Computers in Simulation,* 81 (2): 158–170, 2010.

[48] N. Yousfi Steiner, D. Hissel, Ph. Mocoteguy, and D. Candusso. Diagnosis of polymer electrolyte fuel cells failure modes (flooding and drying out) by neural network modeling. *International journal of hydrogen energy* 36 (4): 3067-3075, 2010.

[49] J. Larminie, and A. Dicks, *Fuel Cell System Explained*, second edition, 2003.

[50] X. Yuan, C. Song, H Wang, and J. Zhang. Electrochemical Impedance Spectroscopy in PEM Fuel Cells, Fundamentals and Applications. Springer-Verlag, 2010.

[51] X. Yuan, H. Wang, J. Colin Sun, and J. Zhang. AC impedance technique in PEM fuel cell diagnosis - A review. *International Journal of Hydrogen Energy*, 32 (17): 4365-4380, 2007.

[52] N. Yousfi-Steiner, Ph. Mocoteguy, D. Candusso, D. Hissel, A. Hernandez, and A. Aslanides. A review on PEM voltage degradation associated with water management: Impacts, influent factors and characterization. *Journal of Power Sources*, 183 (1): 260-274, 2008.

[53] S. Asghari, A. Mokmeli, and M. Samavati. Study of PEM fuel cell performance by electrochemical impedance spectroscopy. *International Journal of Hydrogen Energy*, 35 (17): 9283-9290, 2010.

[54] FCgen®-1310 Fuel Cell Stack, Product Manual and Integration Guide, Ballard internal report, MAN5100304, 2011.

[55] K.L. Hsueh. A Study of Artificial Neural Networks for Electrochemical Data Analysis., ECS Transactions, 25 (28): 47-58, 2010.

# Appendix A.

## Impedance of 20A load

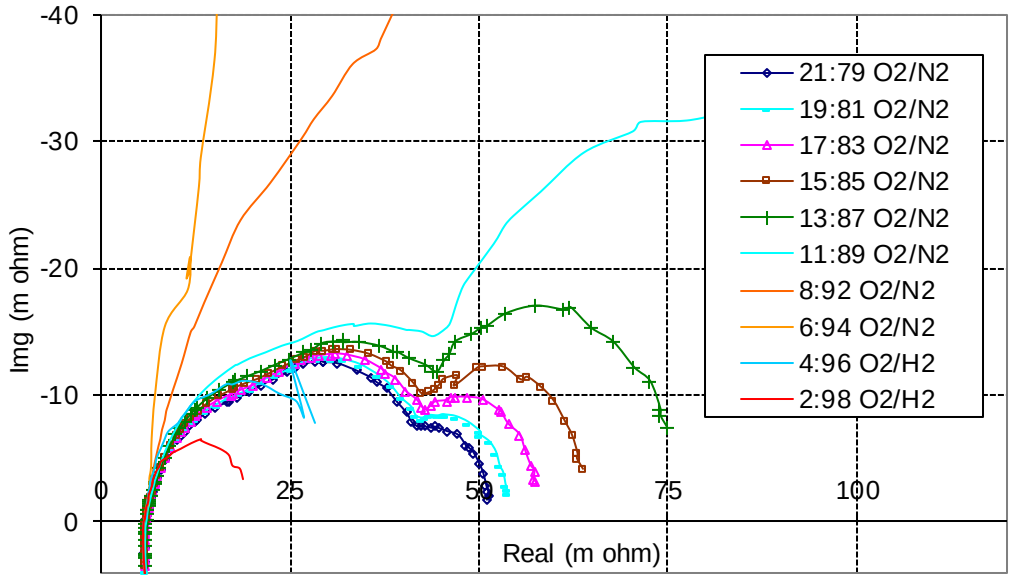


**Figure A.1: Oxygen concentration impedance signatures of 19 normal cells**

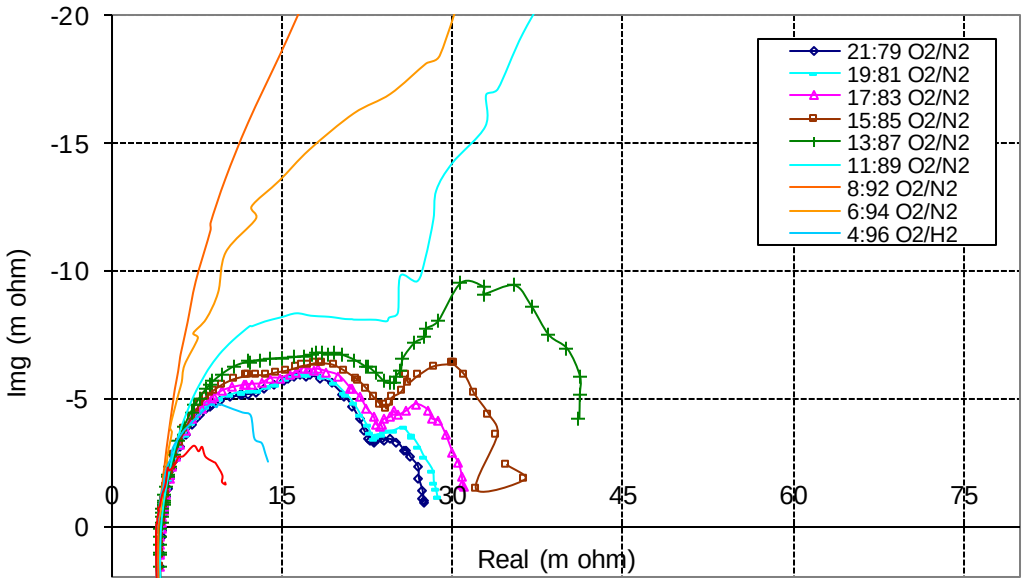


**Figure A.2: Oxygen concentration Impedance signatures of 9 normal cells**

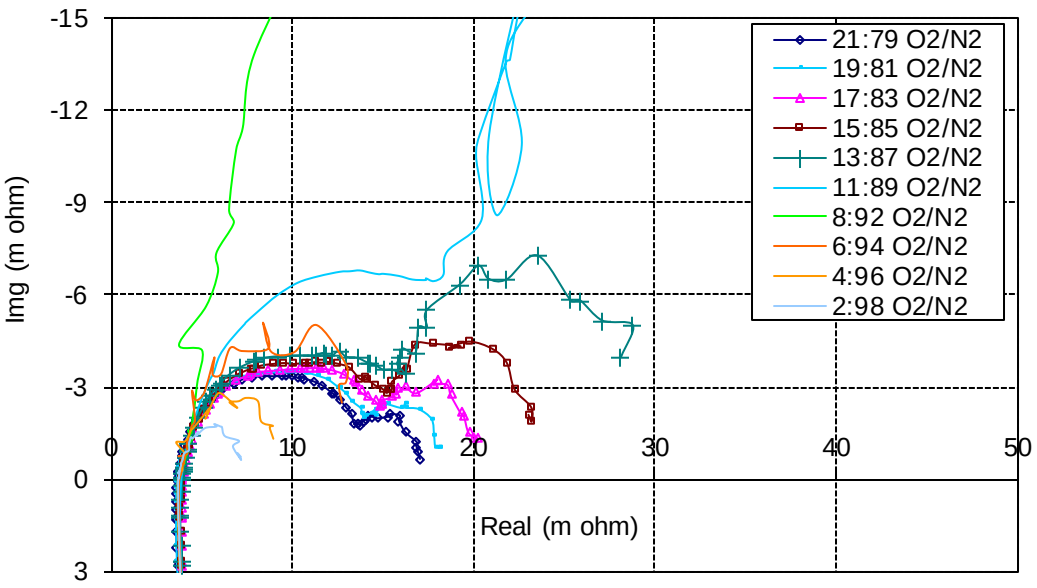


**Figure A.3: Oxygen concentration impedance signatures of 5 normal cells**

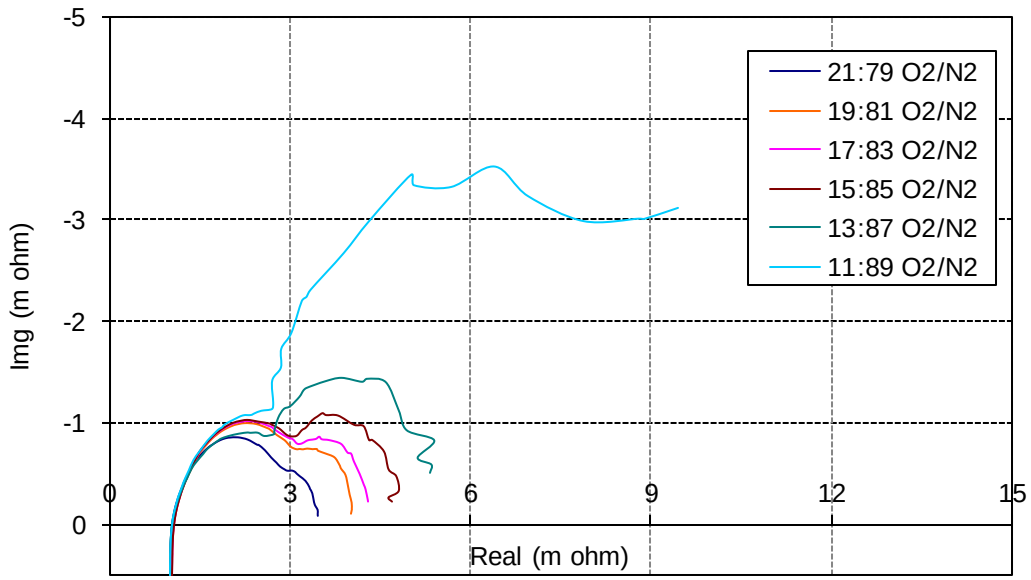


**Figure A.4: Oxygen concentration impedance signatures of a normal cell**

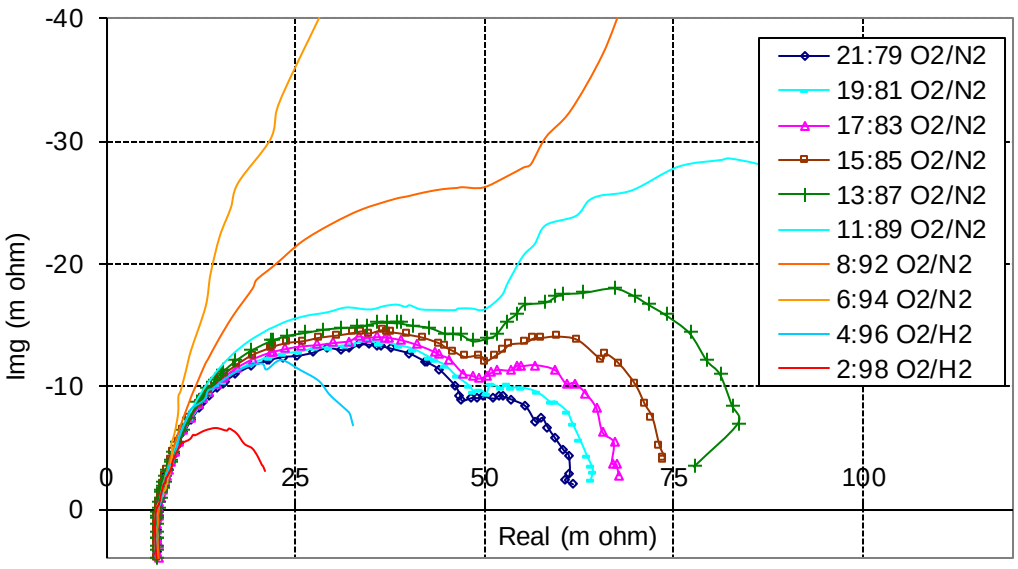


**Figure A.5: Oxygen concentration impedance signatures of 19-cell with a shorted cell**

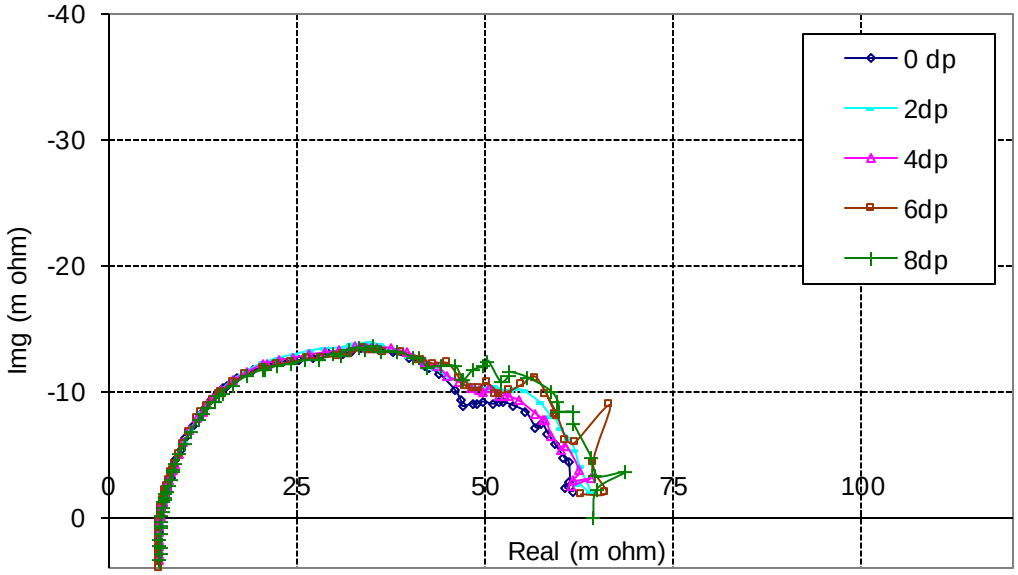


**Figure A.6: Differential pressure impedance signatures of 19-cell with a shorted cell**

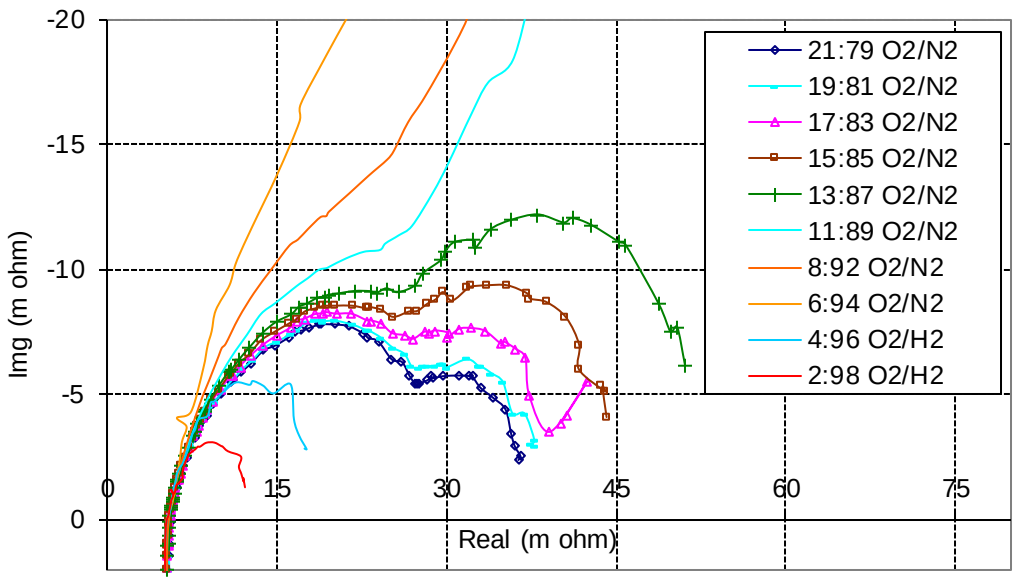


**Figure A.7 Oxygen concentration impedance signatures of 9-cell with a shorted cell**

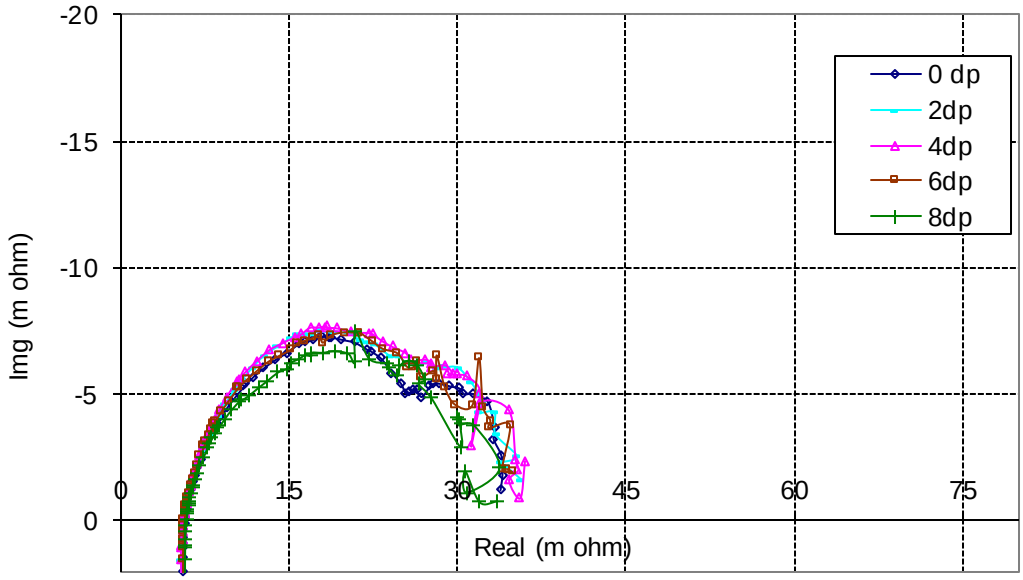


**Figure A.8: Differential pressure signatures of 9-cell with a shorted cell**

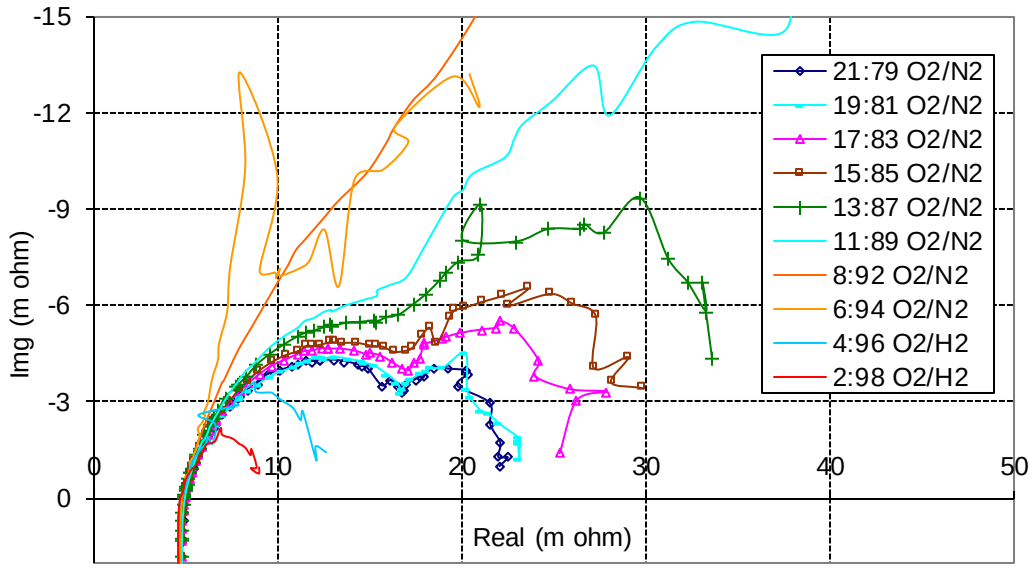


**Figure A.9: Oxygen concentration impedance signatures of 5-cell with a shorted cell**

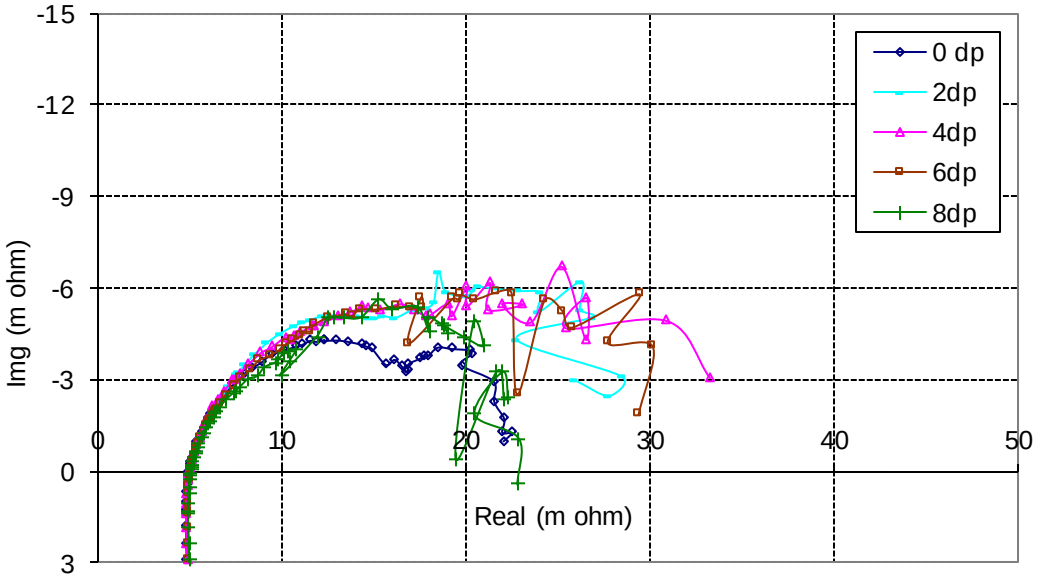


**Figure A.10: Differential pressure impedance signatures of 5-cell with a shorted cell**

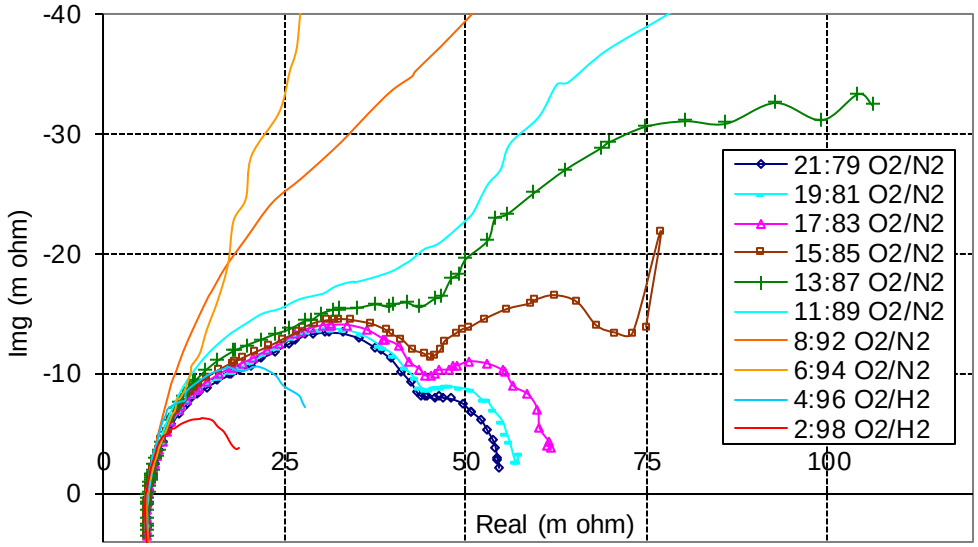


**Figure A.11: Oxygen concentration impedance signatures of 19-cell with a large leaky cell**

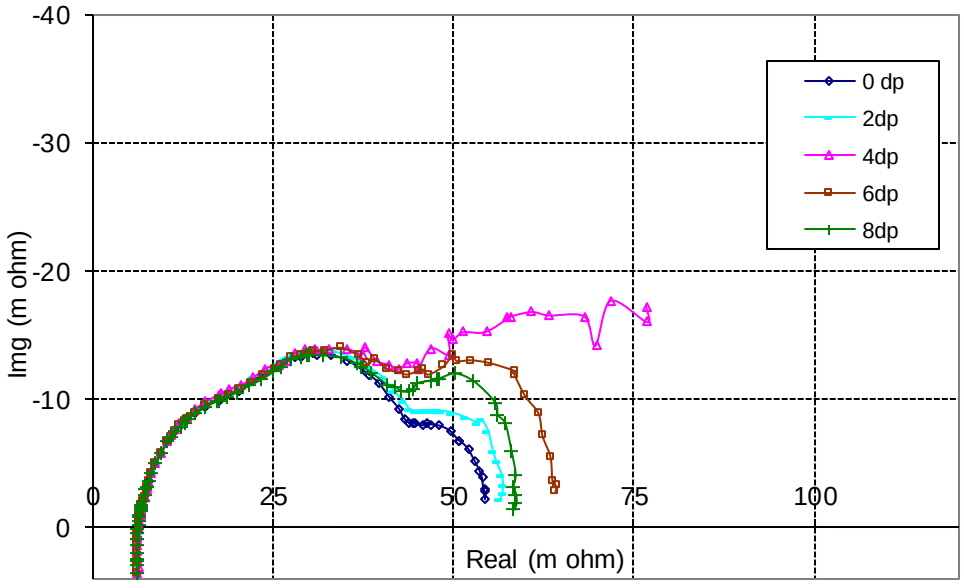


**Figure A.12: Differential pressure impedance signatures of 19-cell with a large leaky cell**

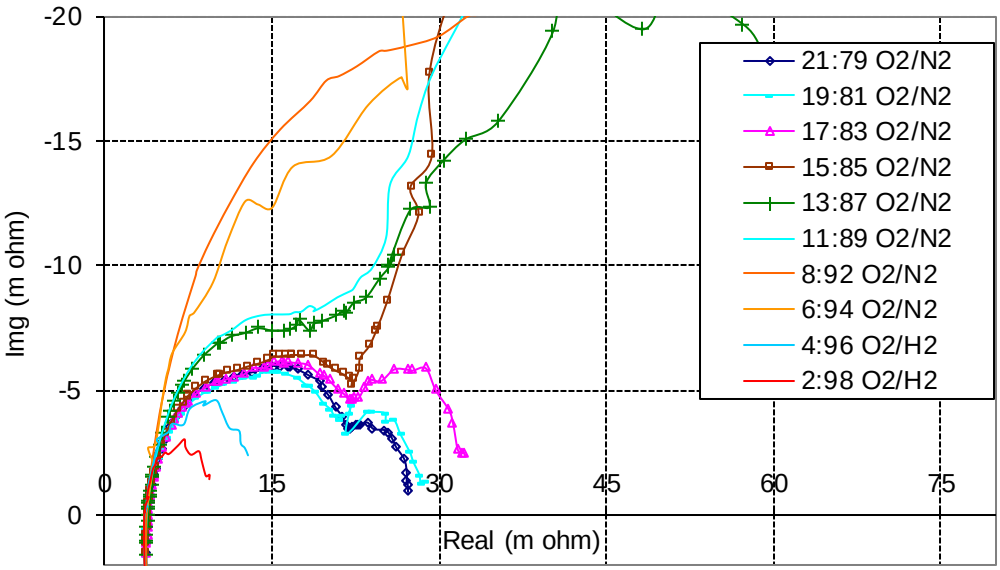


**Figure A.13: Oxygen concentration impedance signatures of 9-cell with a large leaky cell**

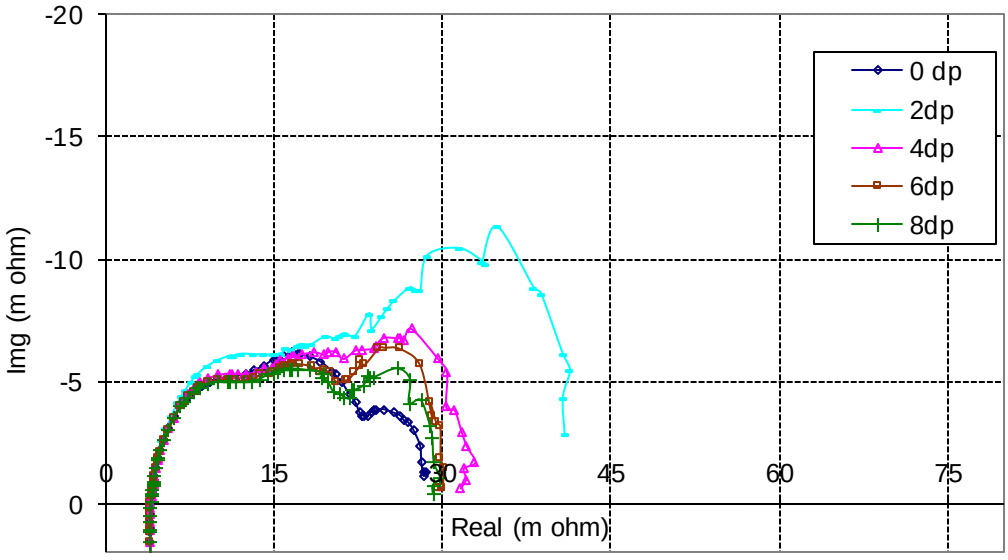


**Figure A.14: Differential pressure impedance signatures of 9-cell with a large leaky cell**

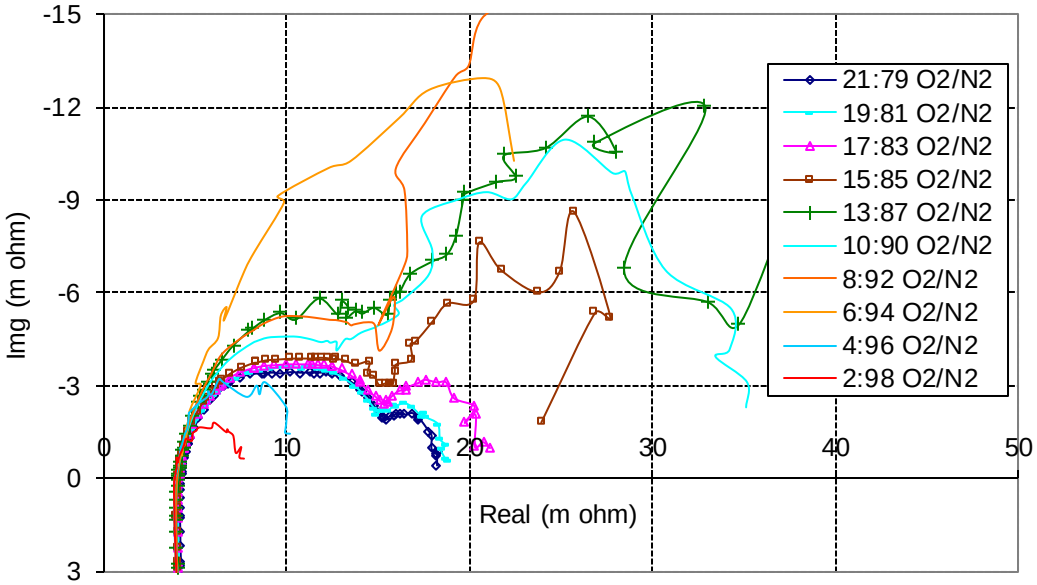


**Figure A.15: Oxygen concentration impedance signatures of 5-cell with a large leaky cell**

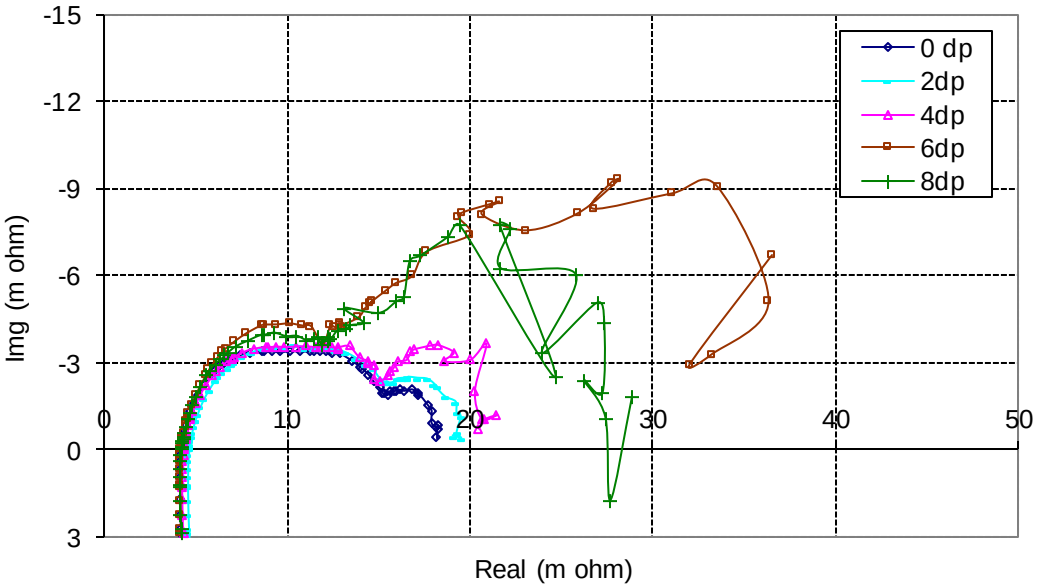


**Figure A.16: Differential pressure impedance signatures of 5-cell with a large leaky cell**

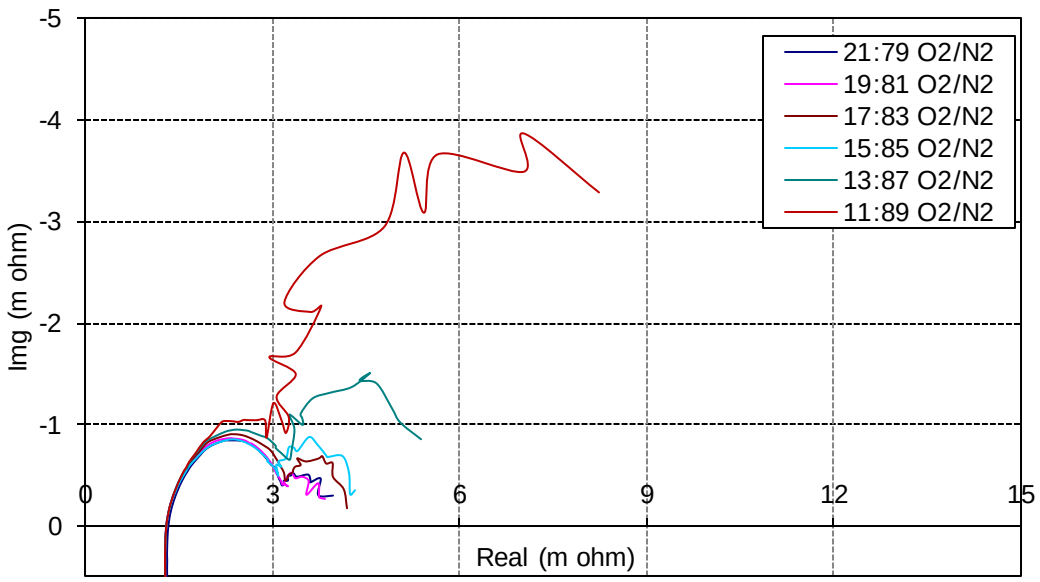


**Figure A.17: Oxygen concentration impedance signatures of a large leaky cell**

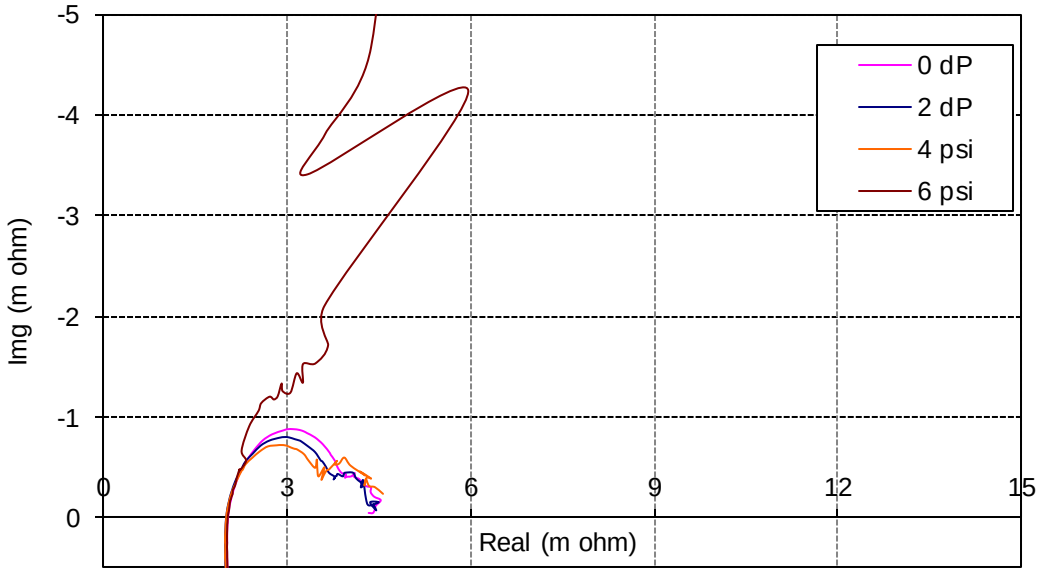


**Figure A.18: Differential pressure impedance signatures of a large leaky cell**

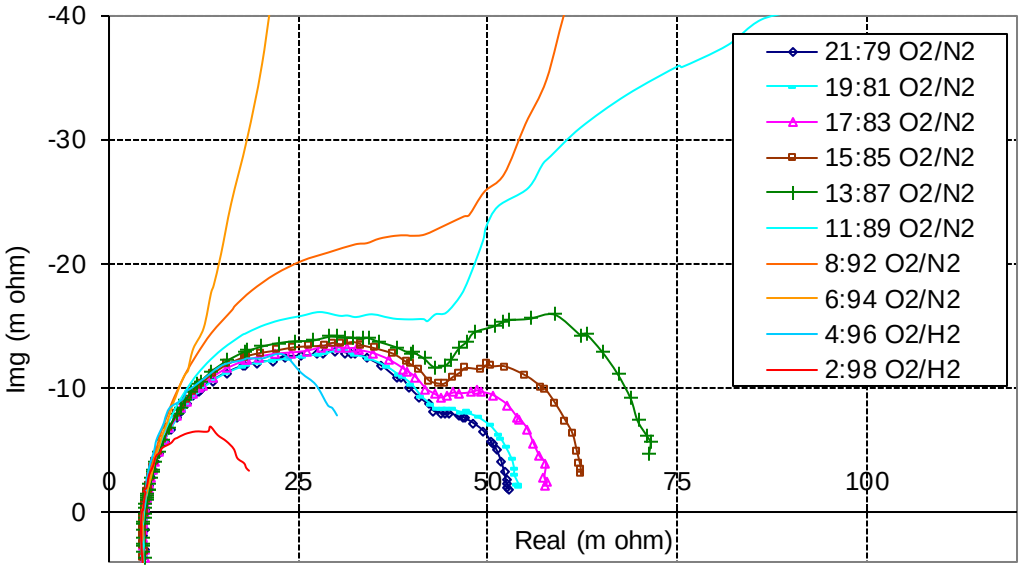


**Figure A.19: Oxygen concentration impedance signatures of 19-cell with a medium leaky cell**

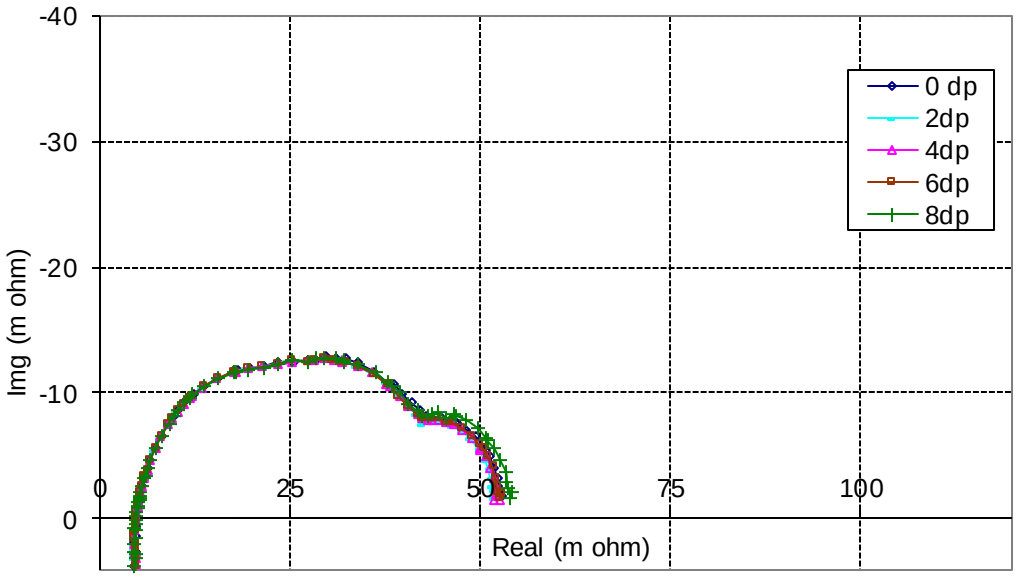


**Figure A.20: Differential pressure impedance signatures of 19-cell with a medium leaky cell**

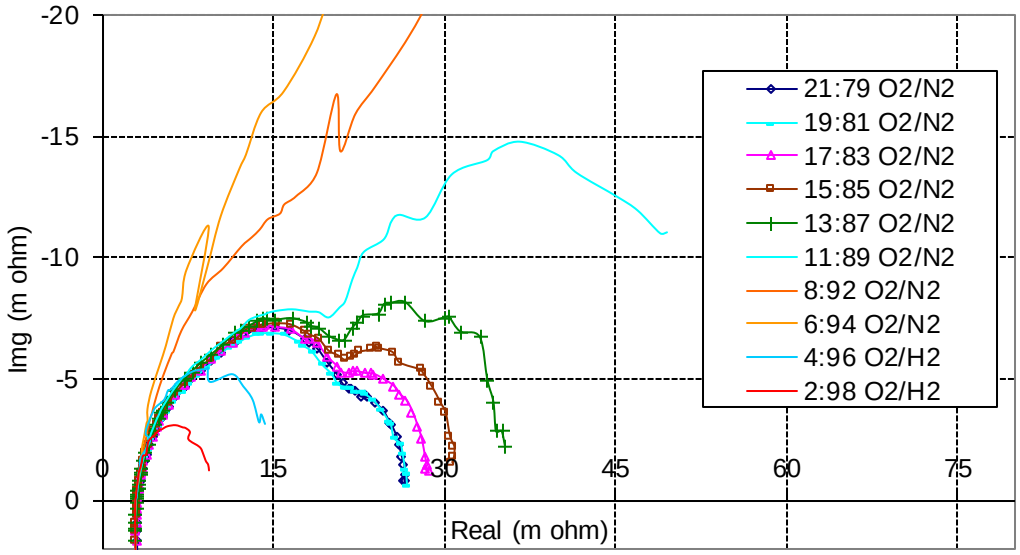


**Figure A.21:Oxygen concentration impedance signatures of 9-cell with a medium leaky cell**

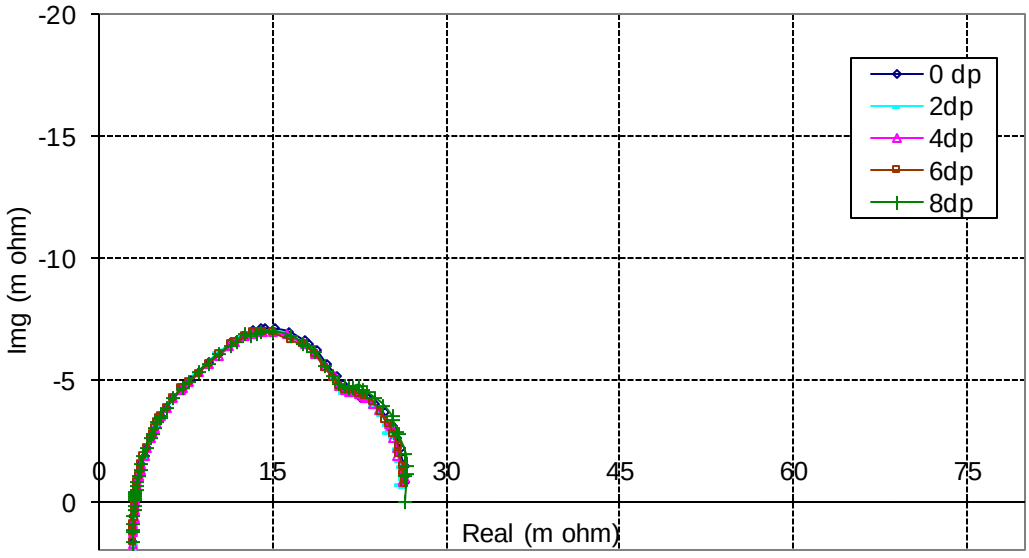


**Figure A.22:Differential pressure impedance signatures of 9-cell with a medium leaky cell**

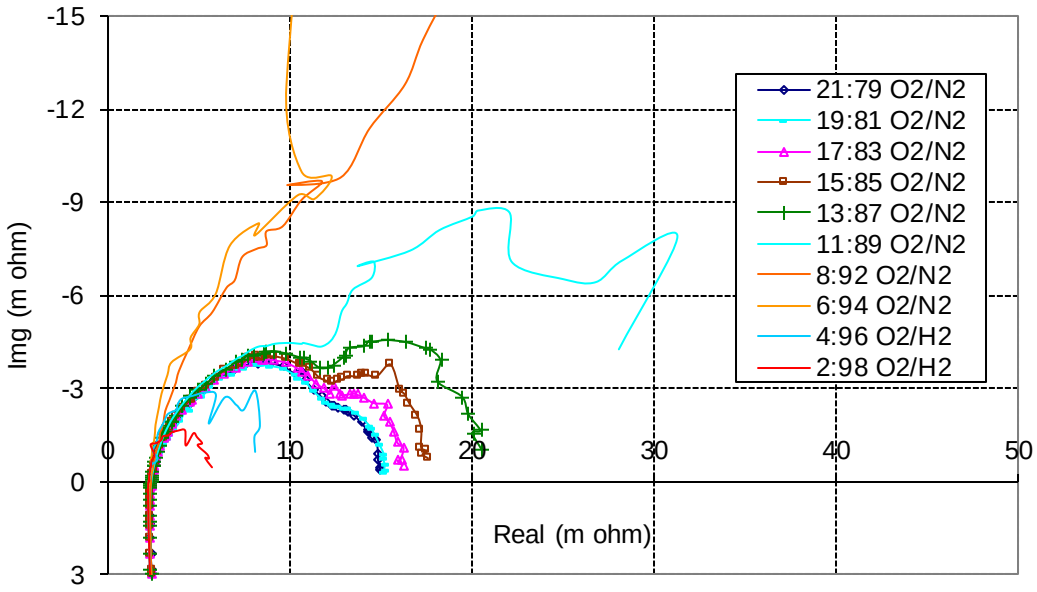


**Figure A.23:Oxygen concentration impedance signatures of 5-cell with a medium leaky cell**

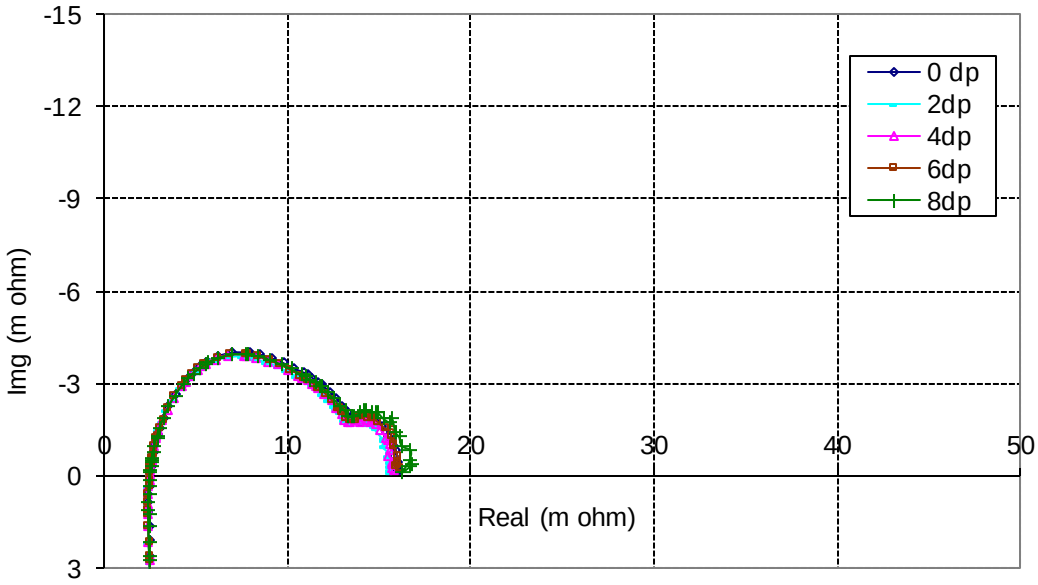


**Figure A.24:Differential pressure impedance signatures of 5-cell with a medium leaky cell**

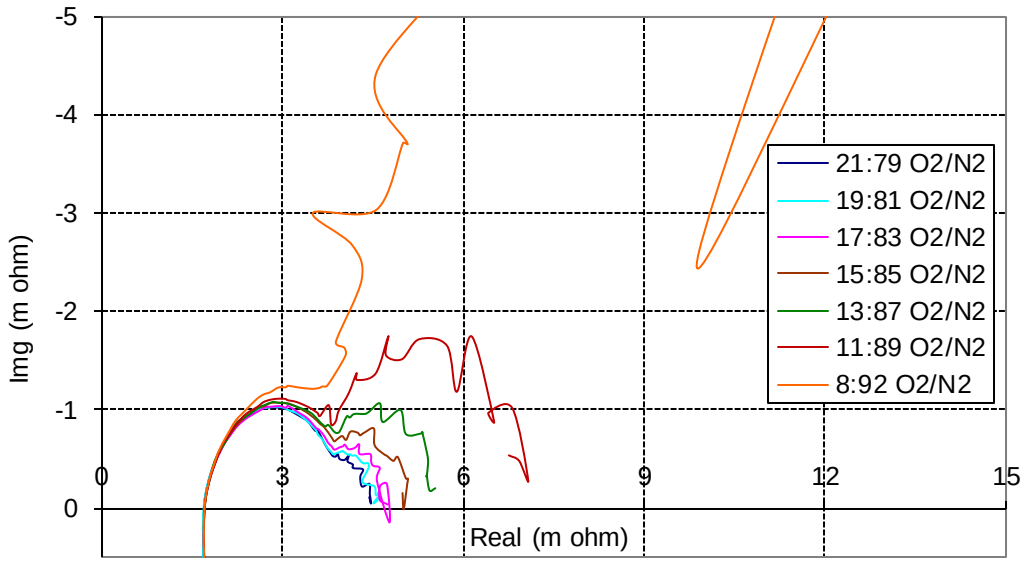


**Figure A.25:Oxygen concentration impedance signatures of a cell with a medium leaky cell**

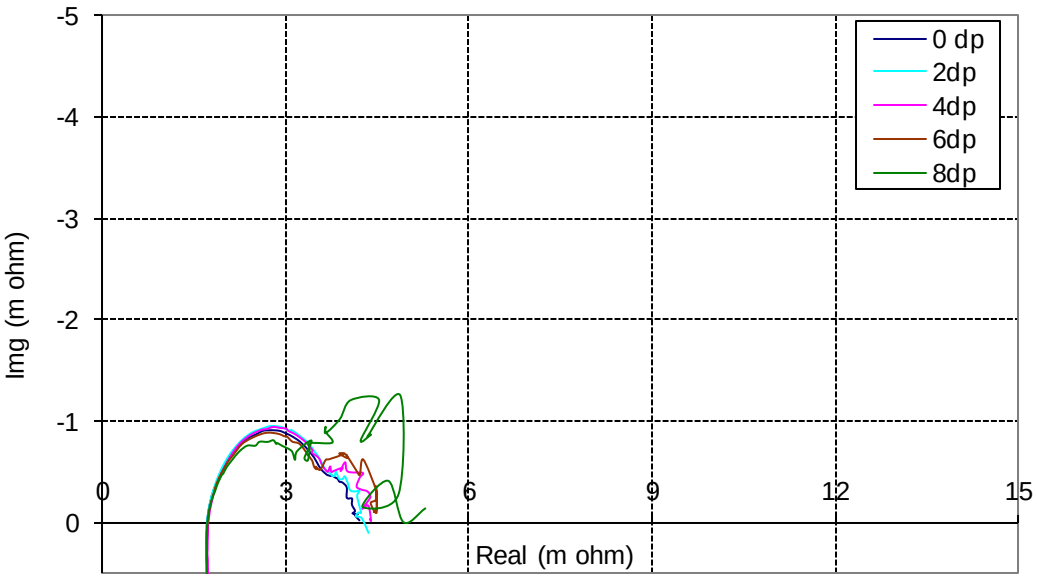


**Figure A.26:Differential pressure impedance signatures of a cell with a medium leaky cell**

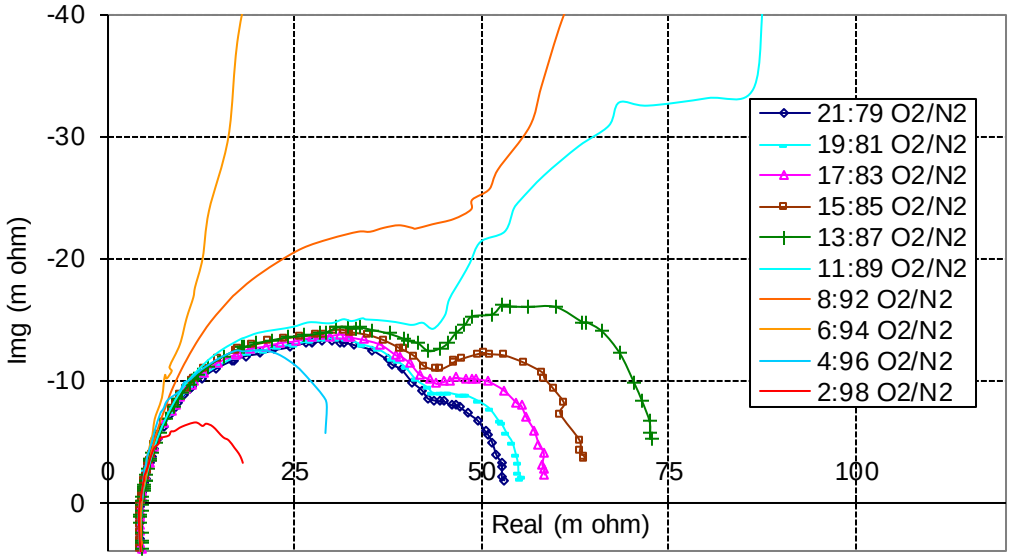


**Figure A.26:Oxygen concentration impedance signatures of 19-cell with a small leaky cell**

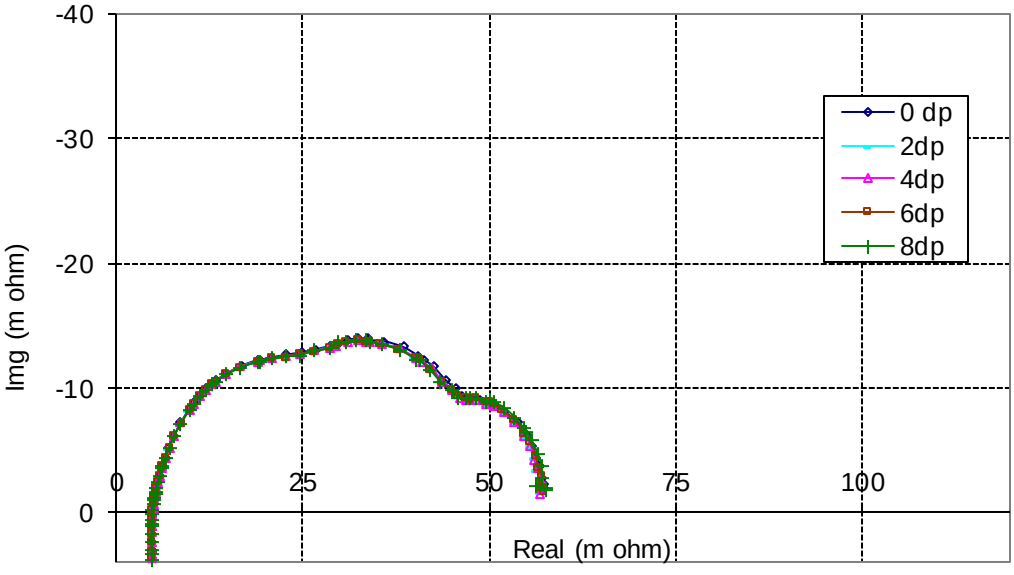


**Figure A.28:Differential pressure impedance signatures of 19-cell with a small leaky cell**

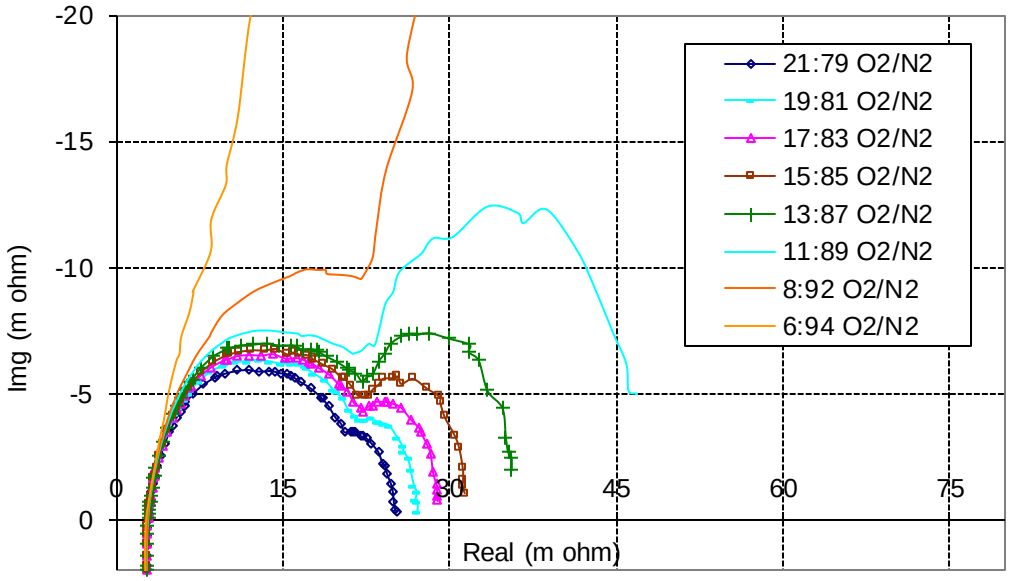


**Figure A.29:Oxygen concentration impedance signatures 9-cell with a small leaky cell**

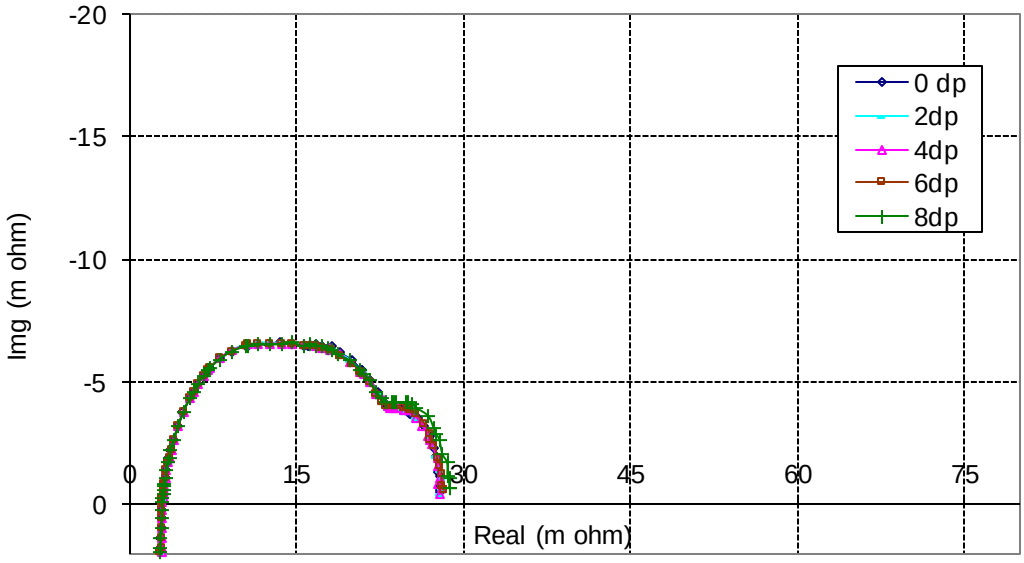


**Figure A.30:Differential pressure impedance signatures of 9-cell with a small leaky cell**

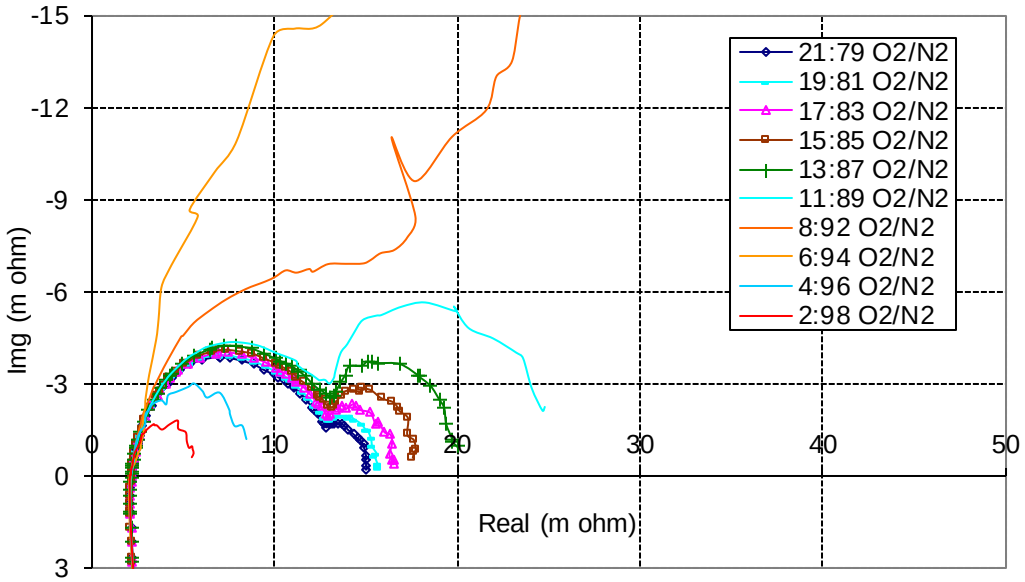


**Figure A.31:Oxygen concentration impedance signatures of 5-cell with a small leaky cell**

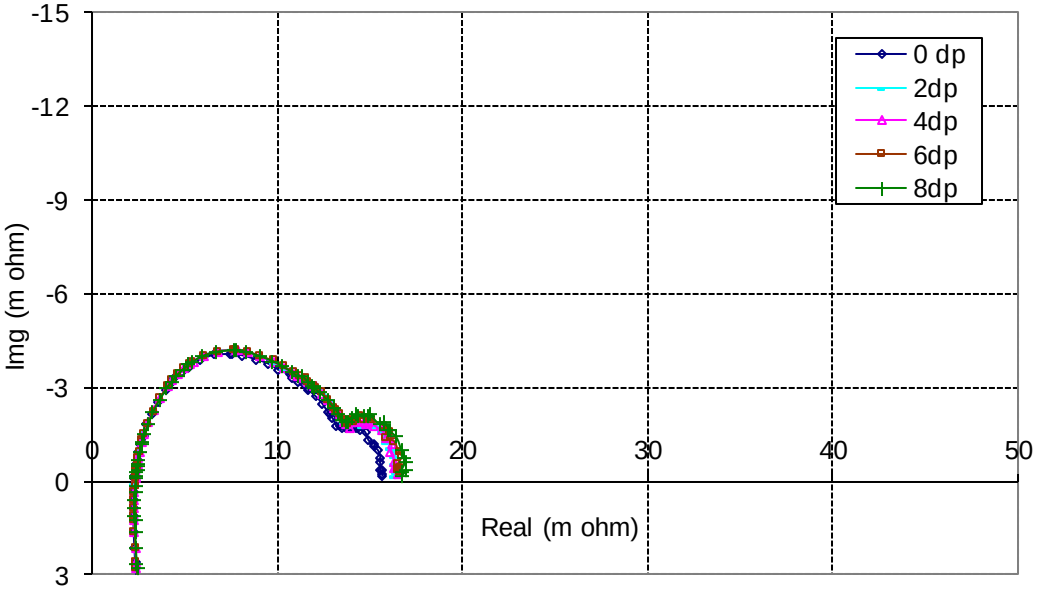


**Figure A.32:Differential pressure impedance signatures of 5-cell with a small leaky cell**

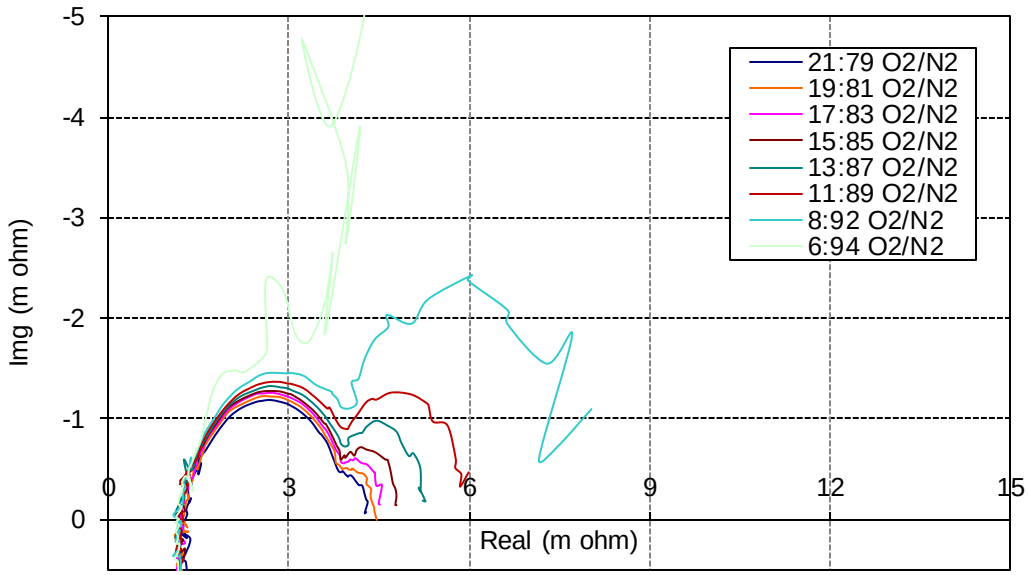


**Figure A.33:Oxygen concentration impedance signatures of a cell with a small leaky cell**

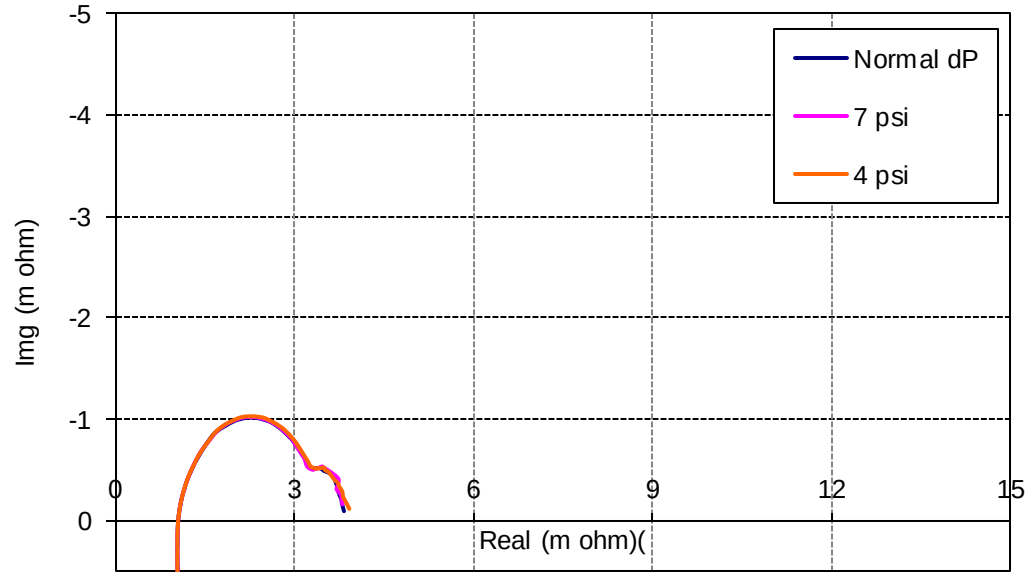


**Figure A.34:Differential pressure impedance signatures of a cell with a small leaky cell**

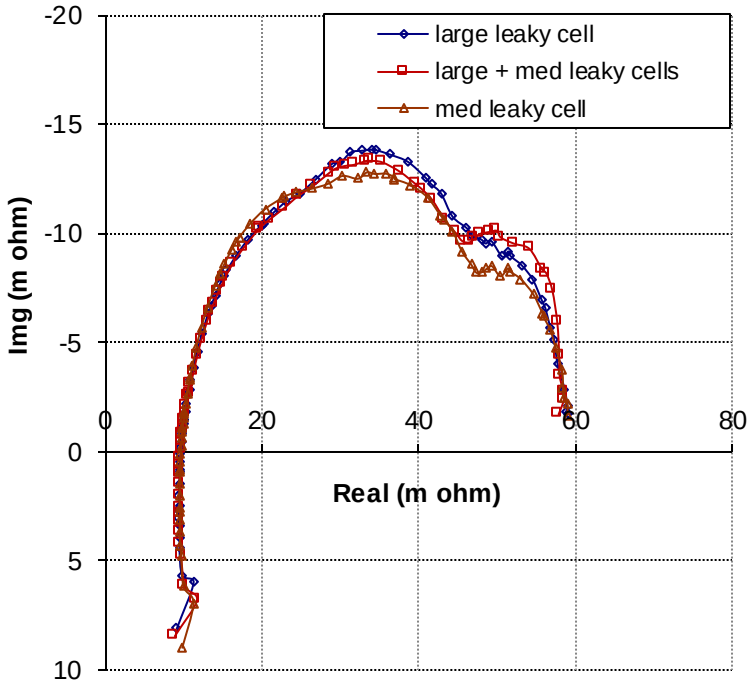


**Figure A.35:Impedance of a large and medium leaky cells with 19-cell stack at 8 dP**

# Appendix B.

## Impedance of 50A load

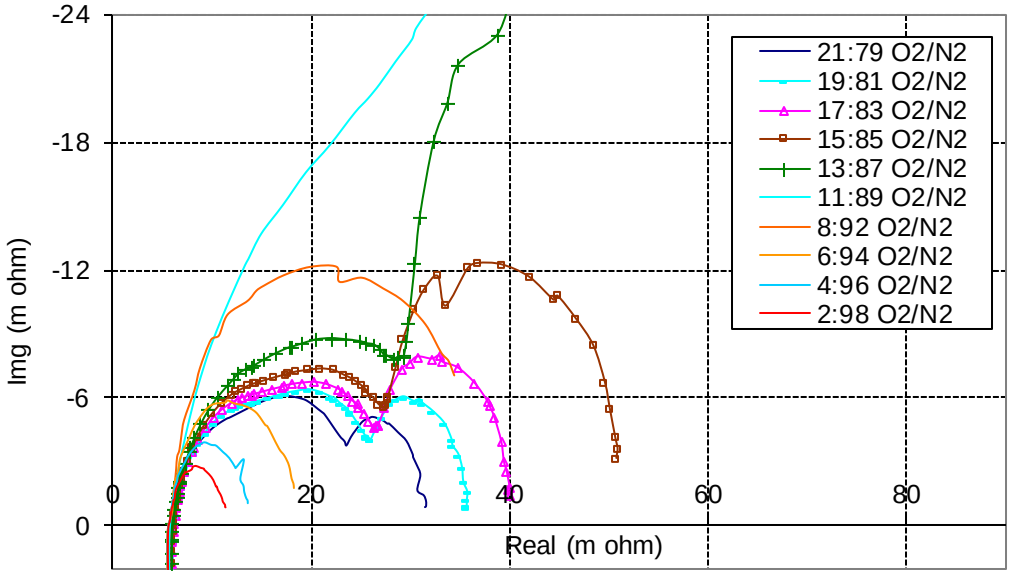


**Figure B.1: Oxygen concentration impedance signatures of 19 normal cells**

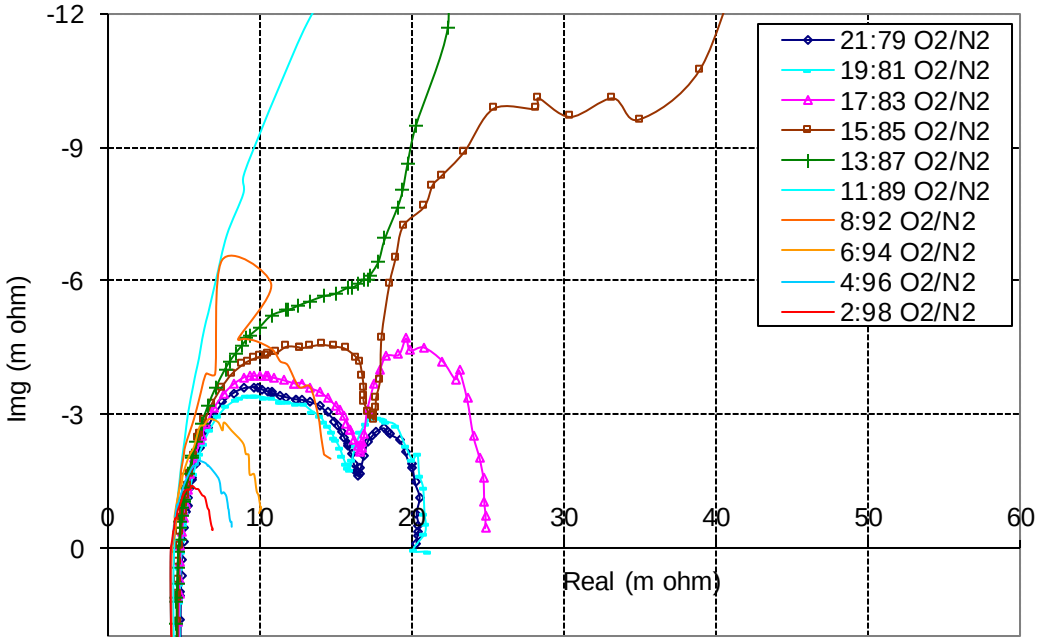


**Figure B.2: Oxygen concentration impedance signatures of 9 normal cells**

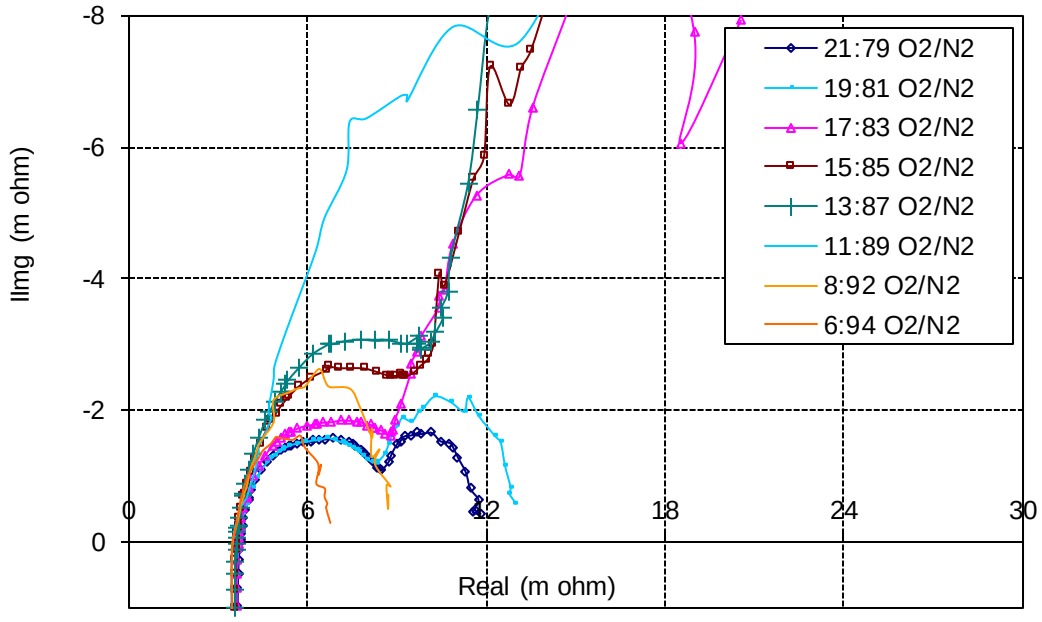


**Figure B.3: Oxygen concentration impedance signatures of 5 normal cells**

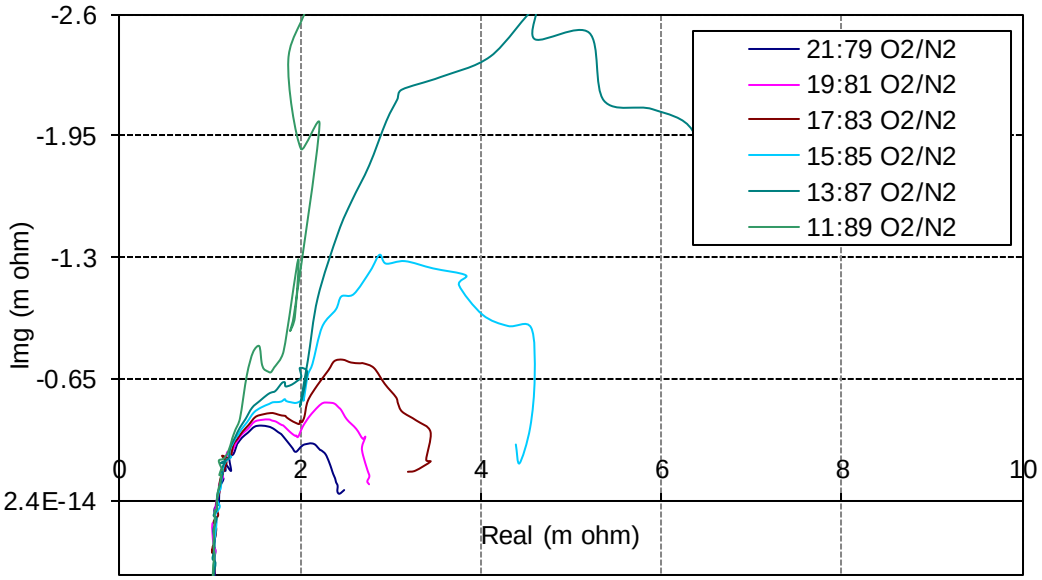


**Figure B.4: Oxygen concentration impedance signatures of a normal cell**

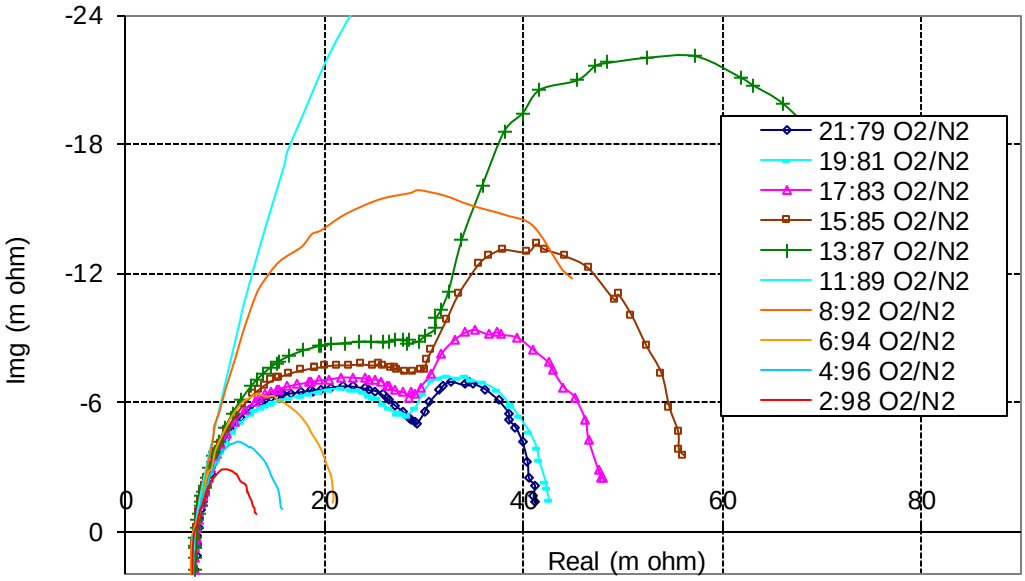


**Figure B.5: Oxygen concentration impedance signatures of 19-cell with a shorted cell**

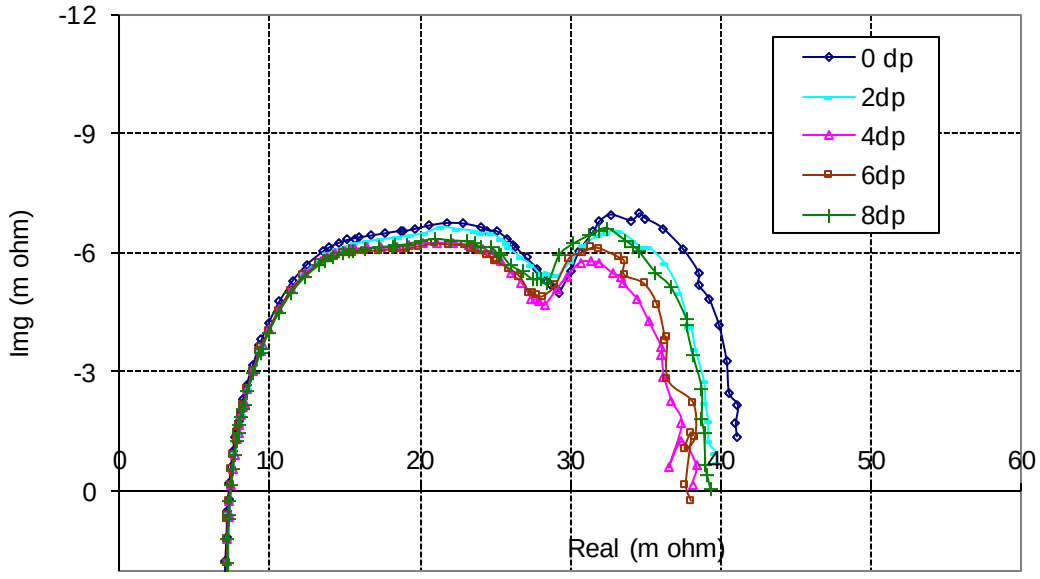


**Figure B.6: Differential pressure impedance signatures of 19-cell with a shorted cell**

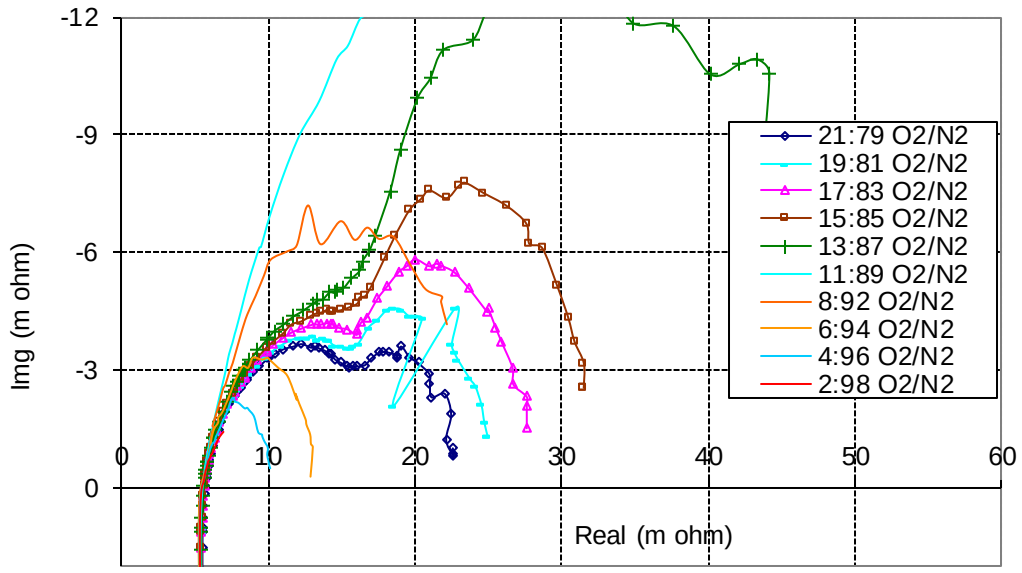


**Figure B.7: Oxygen concentration impedance signatures of 9-cell with a shorted cel l**

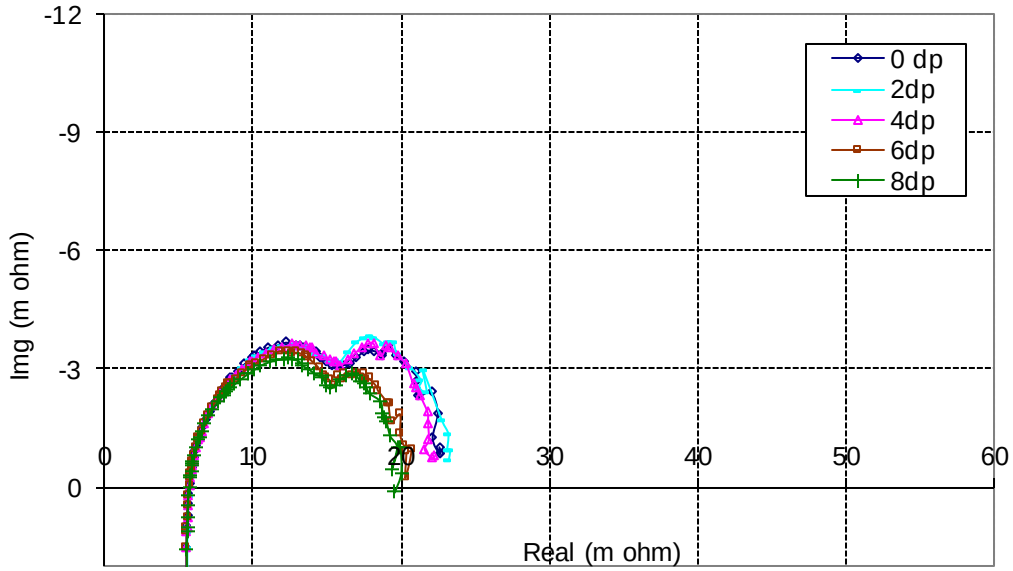


**Figure B.8: Differential pressure impedance signatures of 9-cell with a shorted cell**

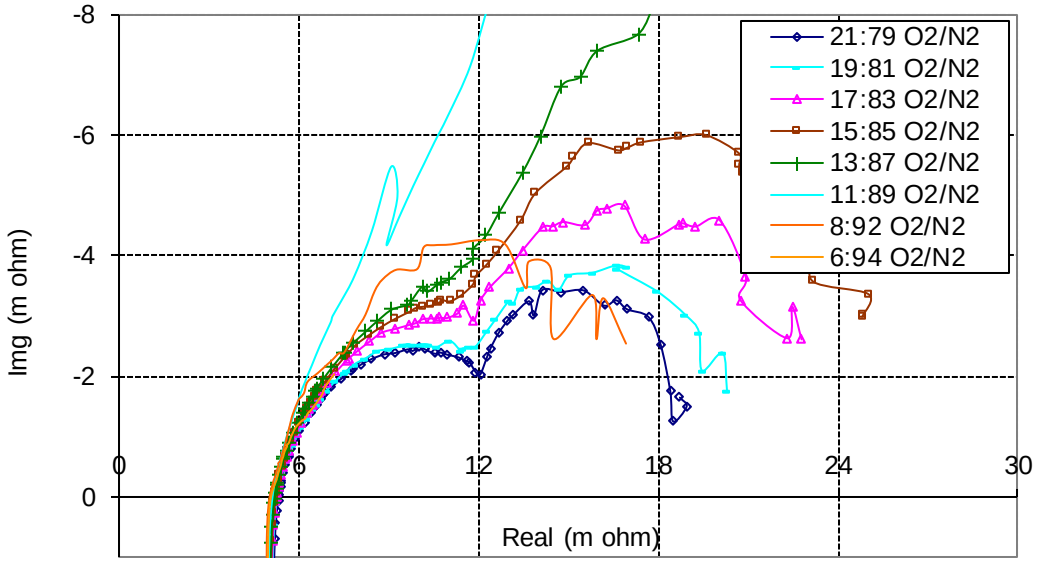


**Figure B.9: Oxygen concentration impedance signatures of 5-cell with a shorted cell**

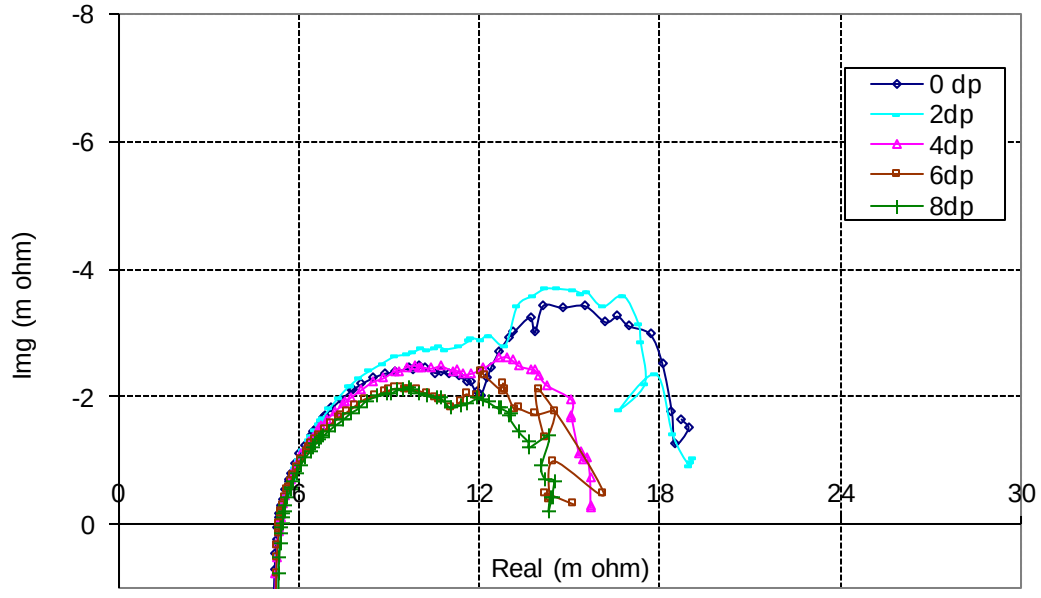


**Figure B.10: Differential pressure impedance signatures of 5-cell with a shorted cell**

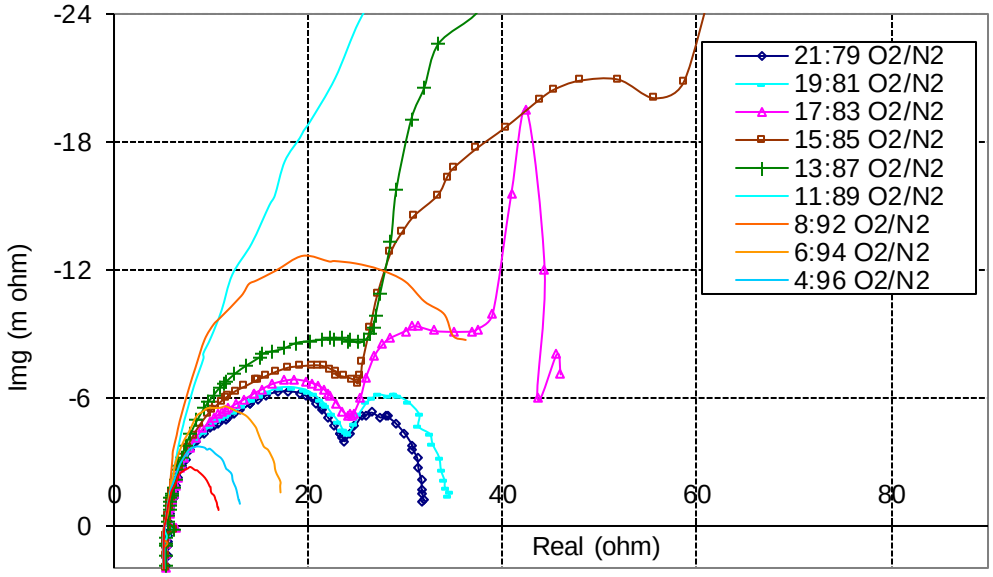


**Figure B.11: Oxygen concentration impedance signatures of 19-cell with a large leaky cell**

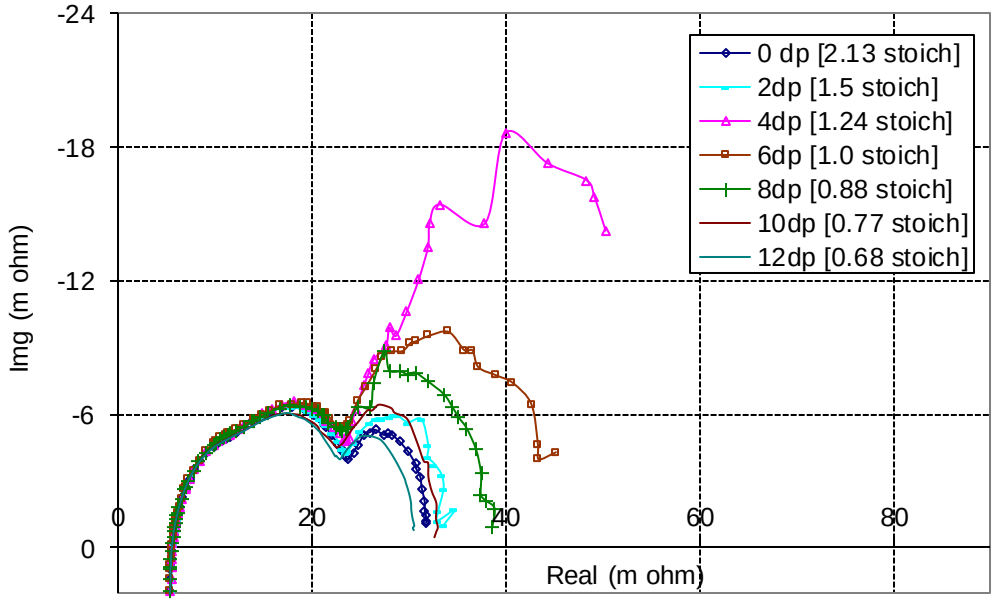


**Figure B.12: Differential pressure impedance signatures of 19-cell with a large leaky cell**

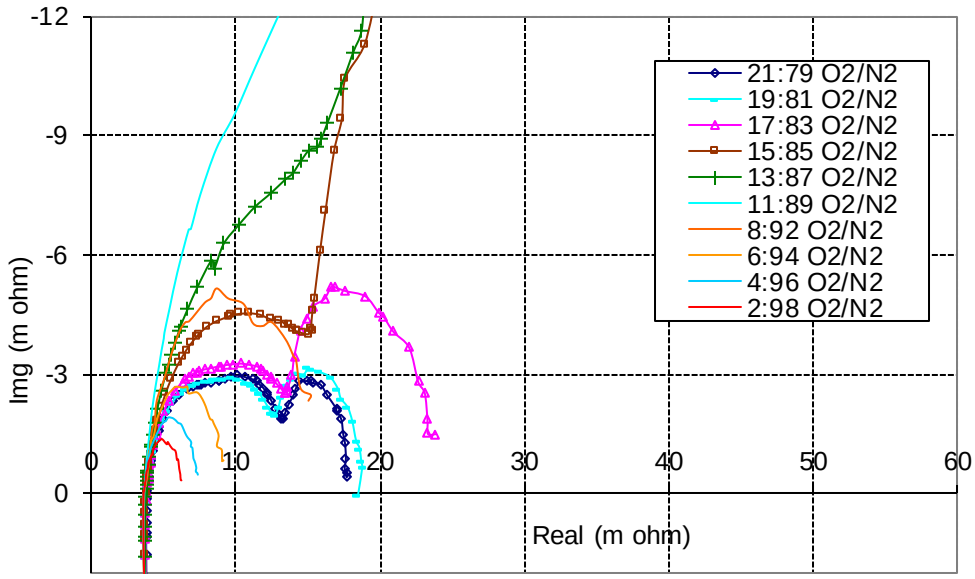


**Figure B.13: Oxygen concentration impedance signatures of 9-cell with a large leaky cell**

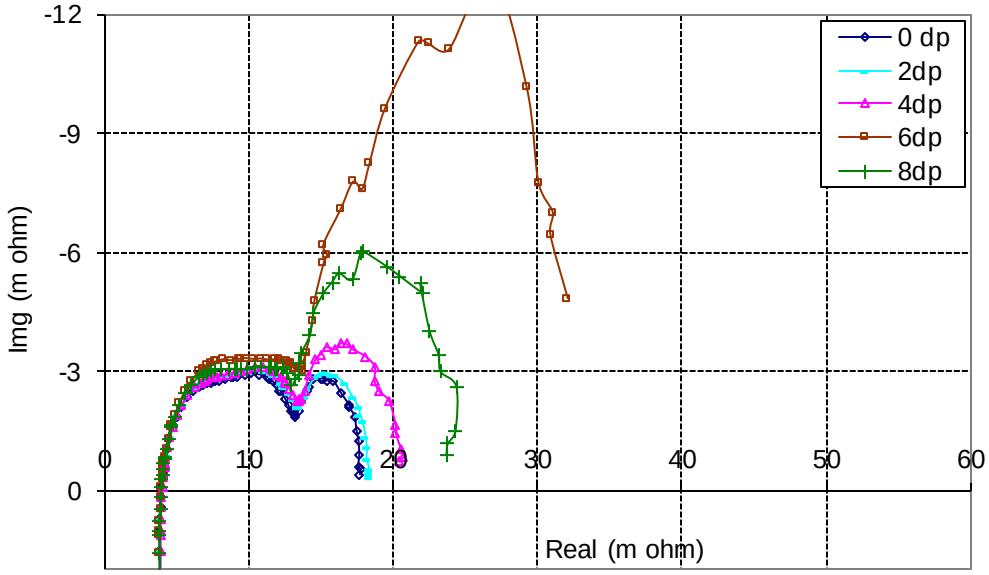


**Figure B.14: Differential pressure impedance signatures of 9-cell with a large leaky cell**

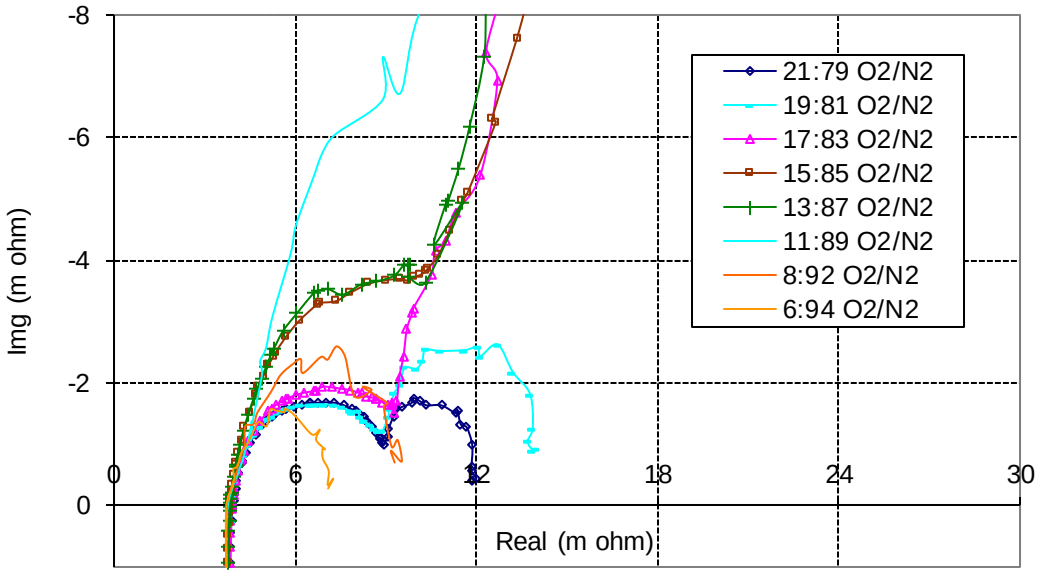


**Figure B.15: Oxygen concentration impedance signatures of 5-cell with a large leaky cell**

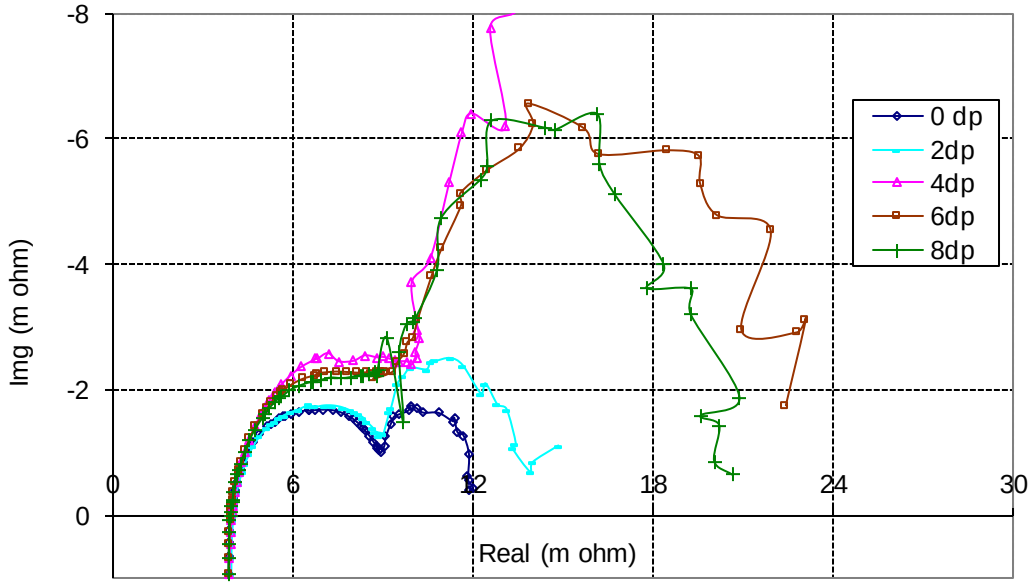


**Figure B.16: Differential pressure impedance signatures of 5-cell with a large leaky cell**

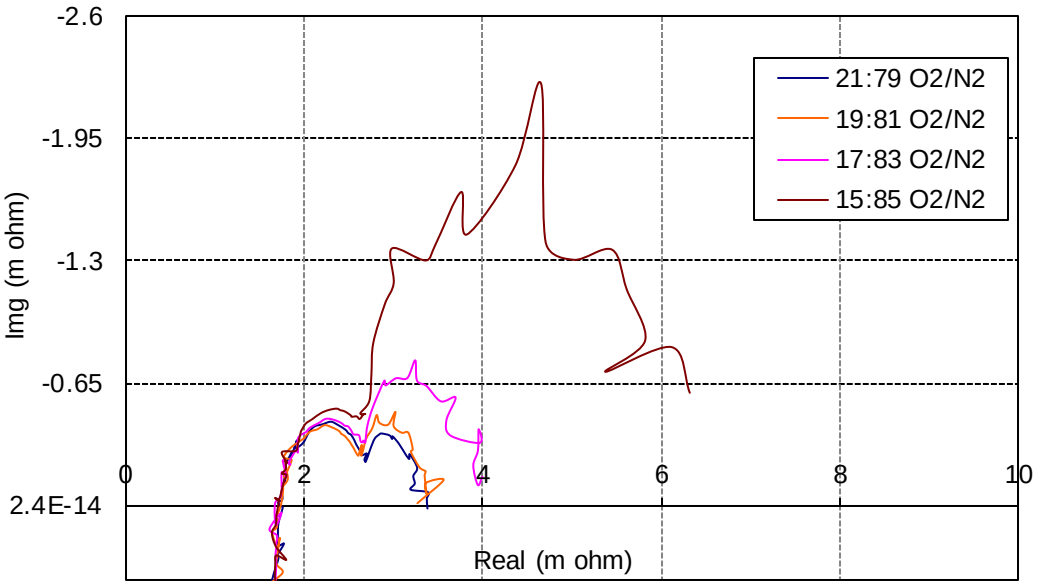


**Figure B.17: Oxygen concentration impedance signatures of a large leaky cell**

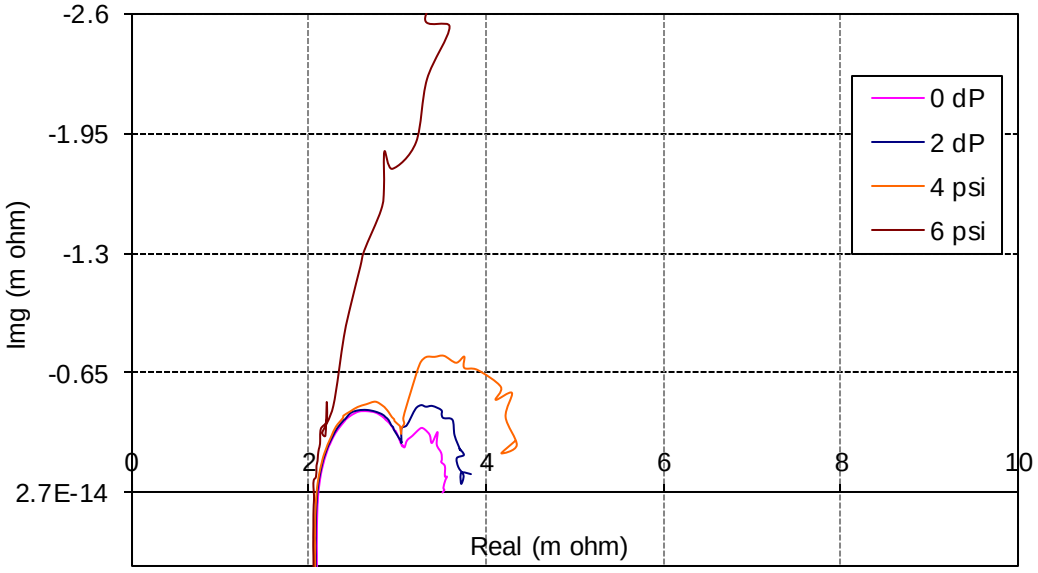


**Figure B18.: Differential pressure impedance signatures of a large leaky cell**

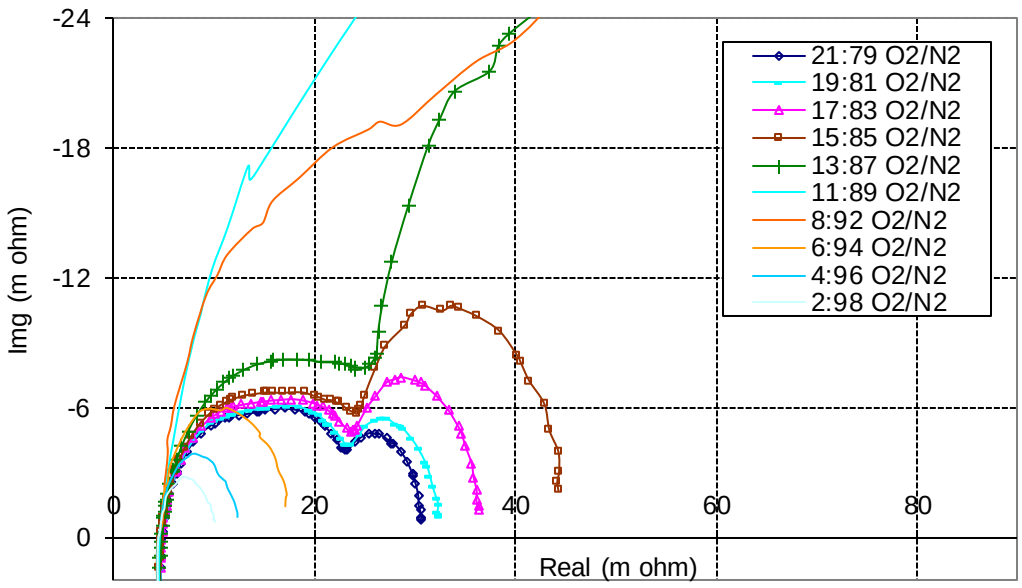


**Figure B.19: Oxygen concentration impedance signatures of 19-cell with a medium leaky cell**

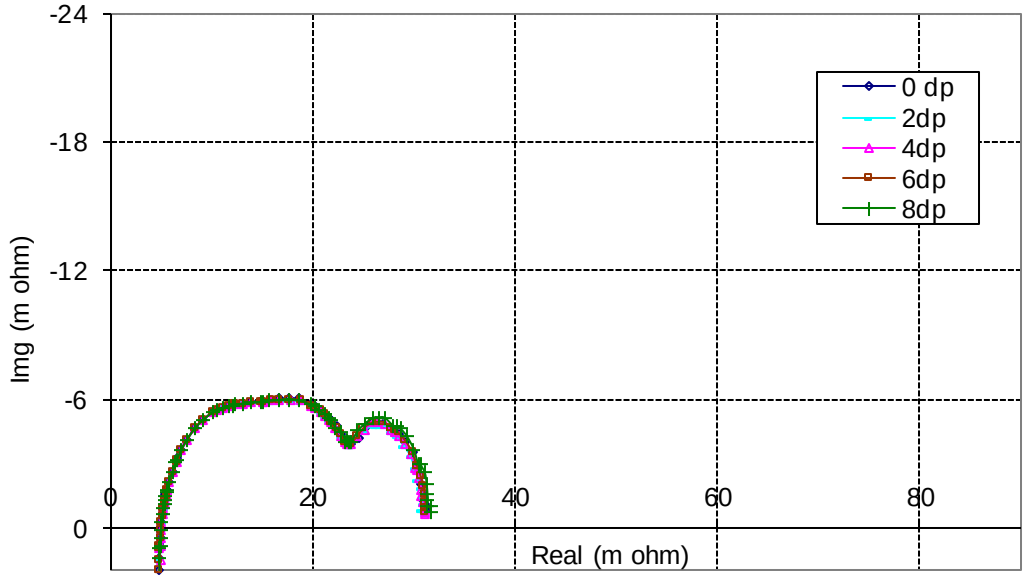


**Figure B.20: Differential pressure impedance signatures of 19-cell with a medium leaky cell**

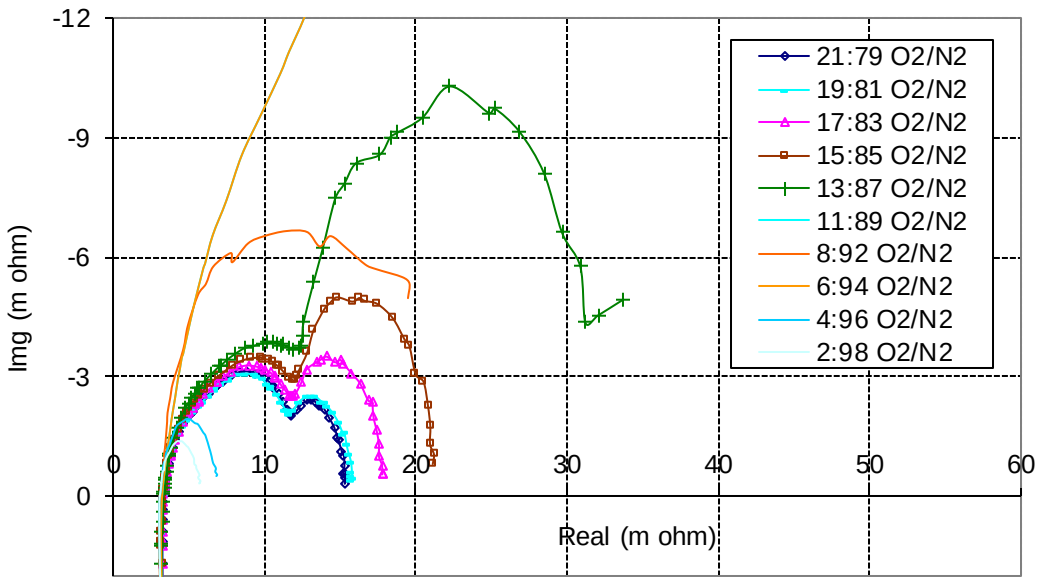


**Figure B.21: Oxygen concentration impedance signatures of 9-cell with a medium leaky cell**

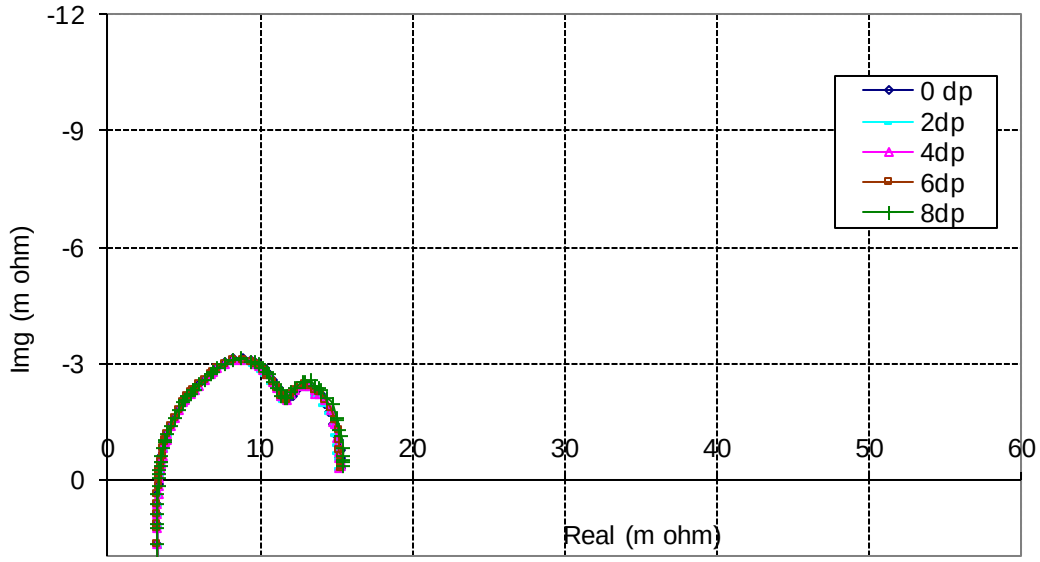


**Figure B.22: Differential pressure impedance signatures of 19-cell with a medium leaky cell**

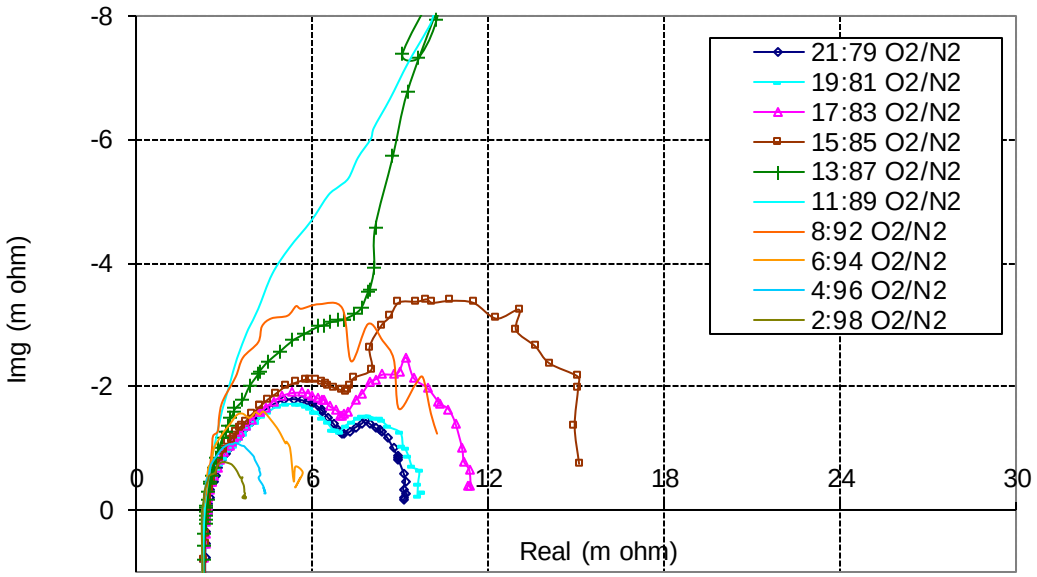


**Figure B.23: Oxygen concentration impedance signatures of 5-cell with a medium leaky cell**

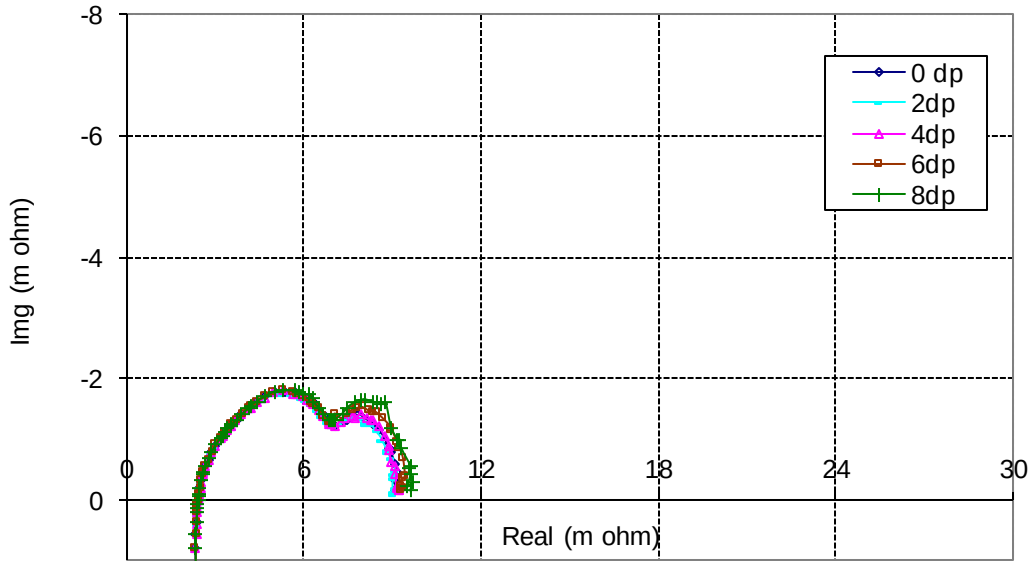


**Figure B.24: Differential pressure impedance signatures of 5-cell with a medium leaky cell**

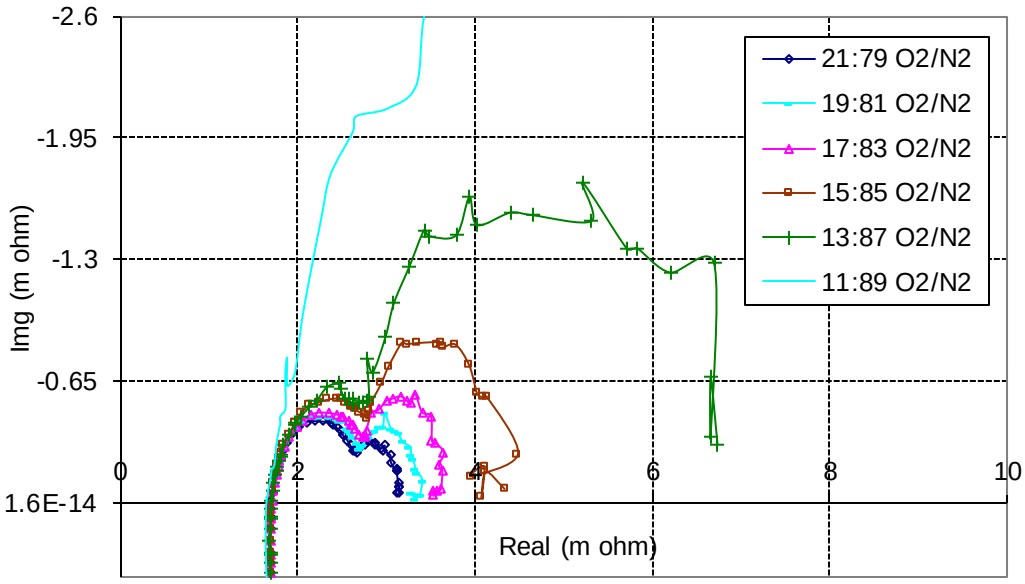


**Figure B.25: Oxygen concentration impedance signatures of a medium leaky cell**

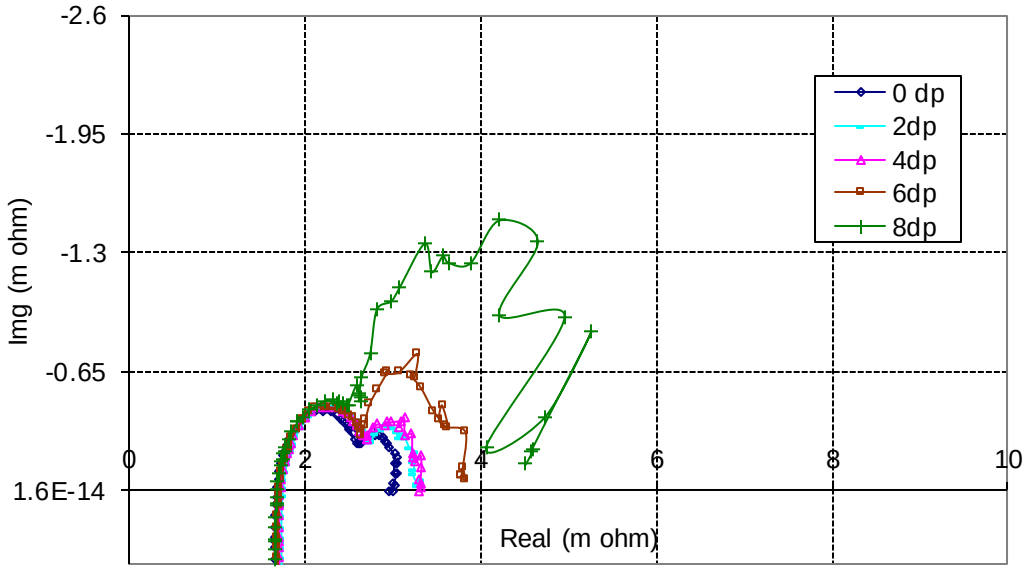


**Figure B.26: Differential pressure impedance signatures of a medium leaky cell**

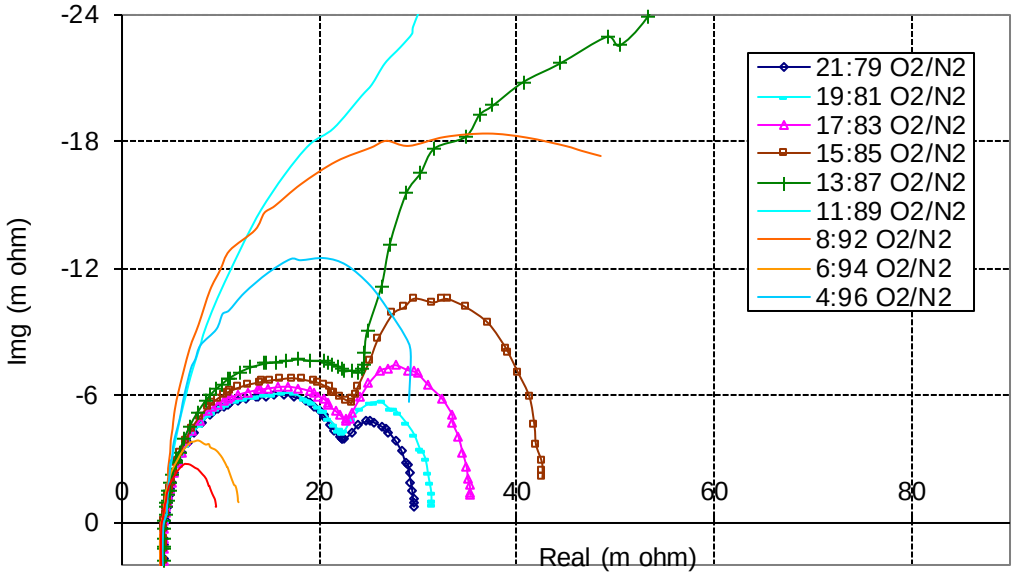


**Figure B.27: Oxygen concentration impedance signatures of 19-cell with a small leaky cell**

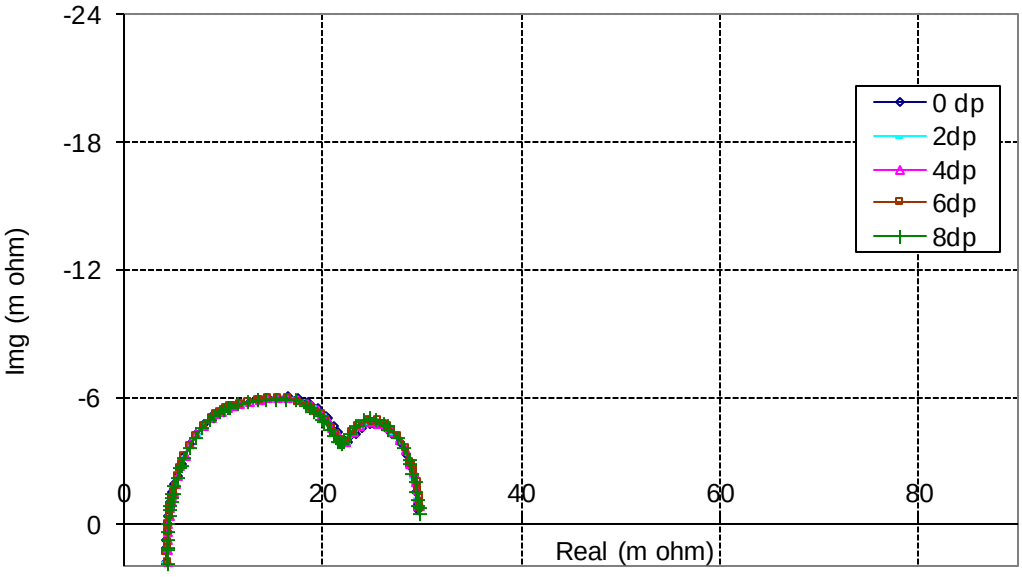


**Figure B.28: Differential pressure impedance signatures of 19-cell with a small leaky cell**

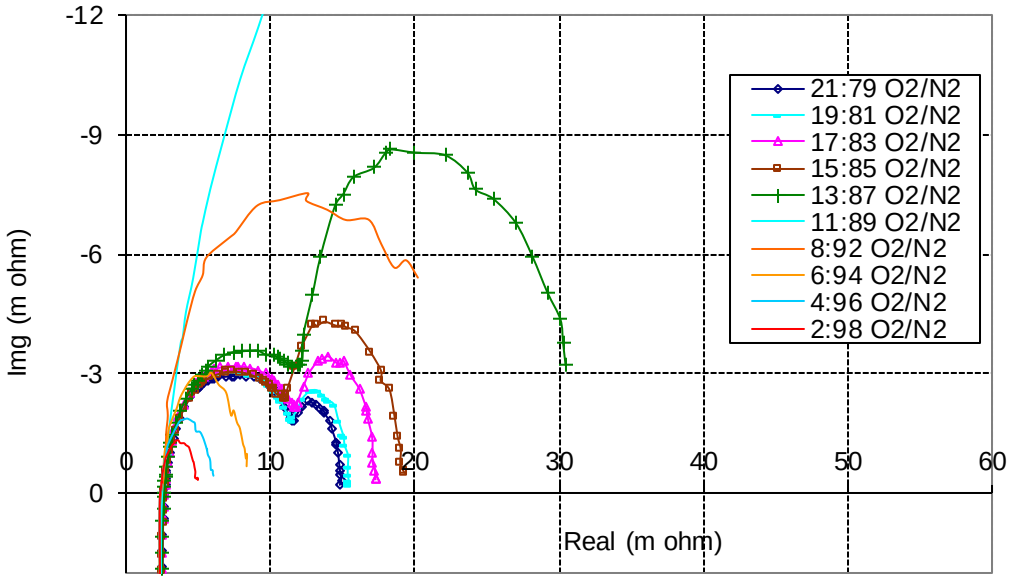


**Figure B.29: Oxygen concentration impedance signatures of 9-cell with a small leaky cell**

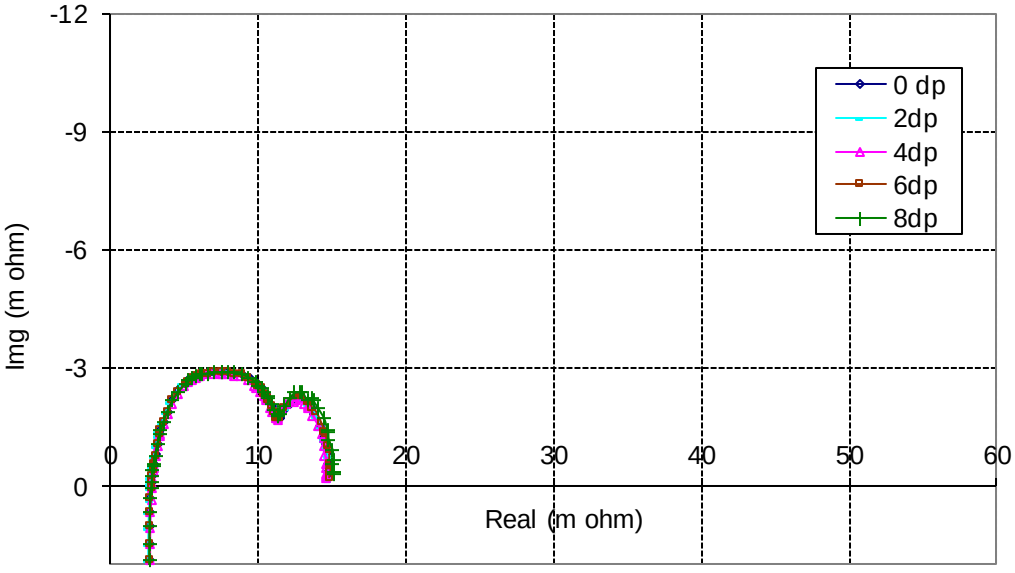


**Figure B.30: Differential pressure impedance signatures of 9-cell with a small leaky cell**

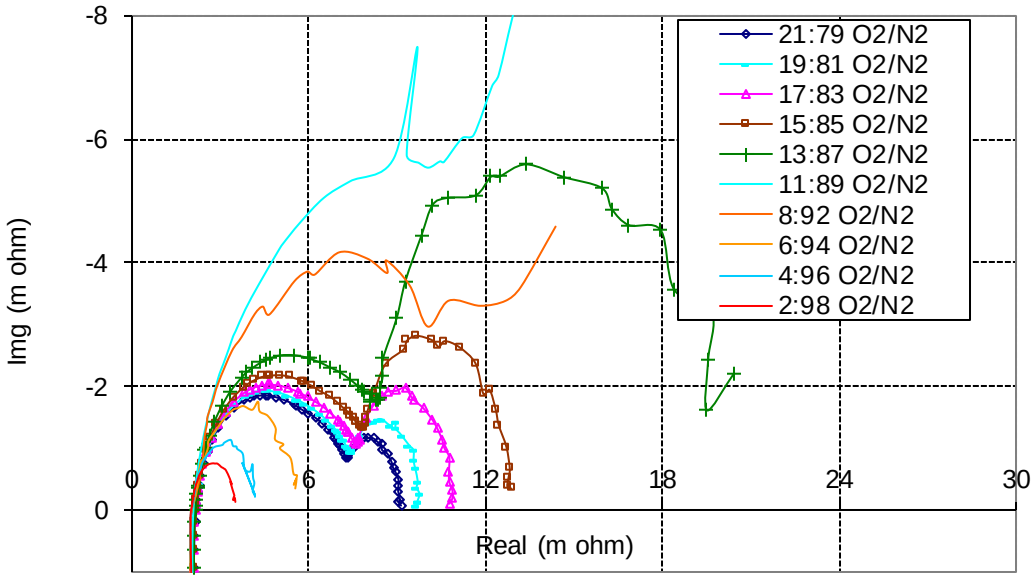


**Figure B.31: Oxygen concentration impedance signatures of 5-cell with a small leaky cell**

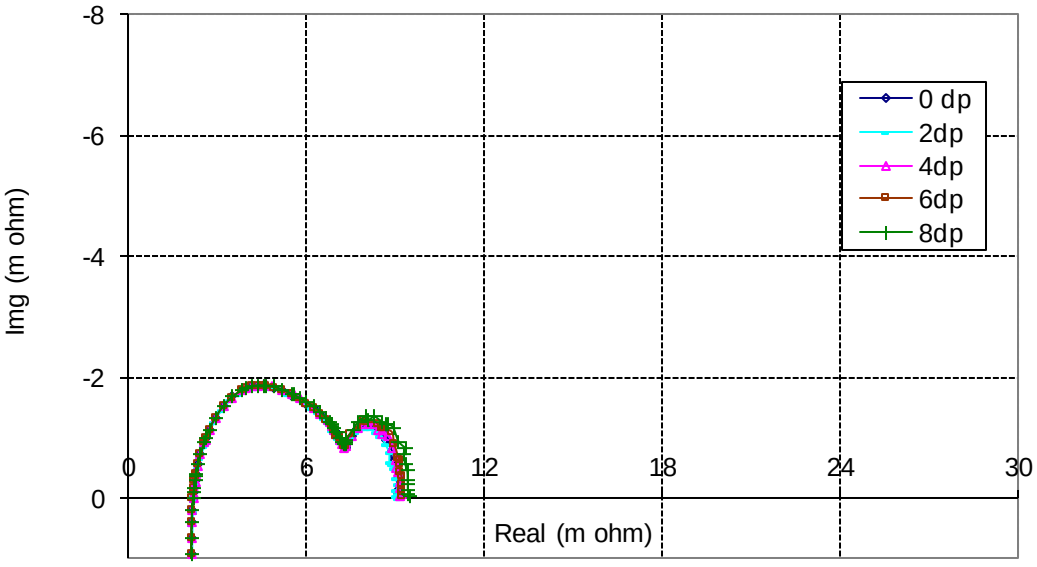


**Figure B.32: Differential pressure impedance signatures of 5-cell with a small leaky cell**

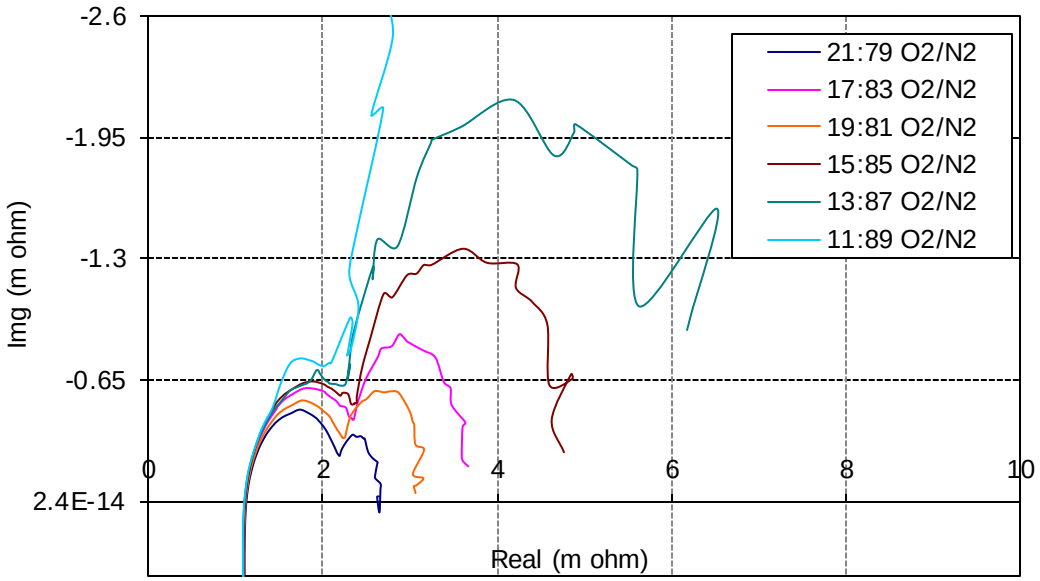


**Figure B.33: Oxygen concentration impedance signatures of a small leaky cell**

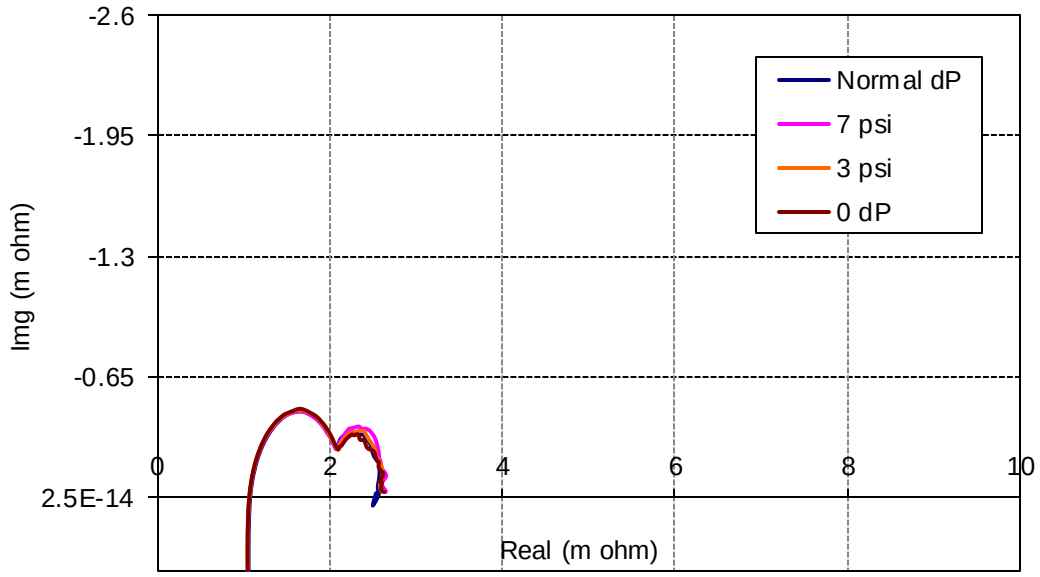


**Figure B.34: Differential pressure impedance signatures of a small leaky cell**

# Appendix C.

# MATLAB codes

Code used to calculate the stack voltage:

```
a = 1;
t = [0:.1:3]';
% f & I are the frequency and current respectively
% Ro, R & C known from fitting the data to the electrical circuit
for k = 1:size (f)
    z = Ro+(1/((-i*f(a,:)*C)+(1/R)))';
    x = I*((Ro+R)-(R*exp(-t/(C*R))))';
    a = a+1;
end
v = max(x)
```

Code used to train the NN:

```
% in are is the network input
% target is the network target
% m: slope; b: intersect; r: correlation coefficient 2

net = newff(in,target,[20]);
net.trainParam.show = 5;
net.trainParam.epochs = 5000;
net.trainParam.goal = 0.01;
net = init(net);
[netdPDeg,tr] = train(net,in,target);
plotperform(tr);
close;

a = sim(netdPDeg,in);
[m,b,r] = postreg(a(1,:),target(1,:))
```